AD-A109 683 SRI INTERNATIONAL MENLO PARK CA F/G 4/1
ANALYSIS OF NUCLEAR PROPAGATION EFFECTS UTILIZING WIDEBAND SATE--ETC(U)
APR 81 C L RINO, J OWEN, R C LIVINGSTON DNA001-80-C-0077
UNCLASSIFIED DNA-5807F NL

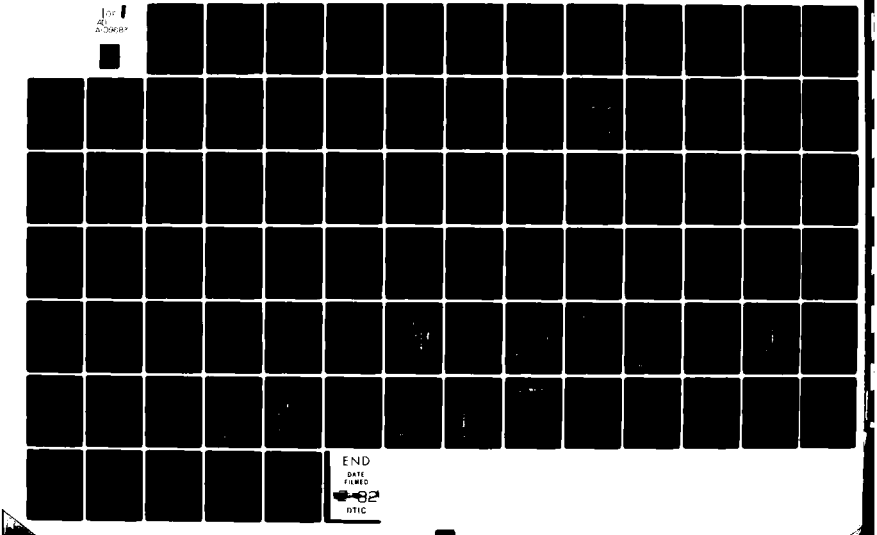

END
DATE FILMED
-82
DTIC

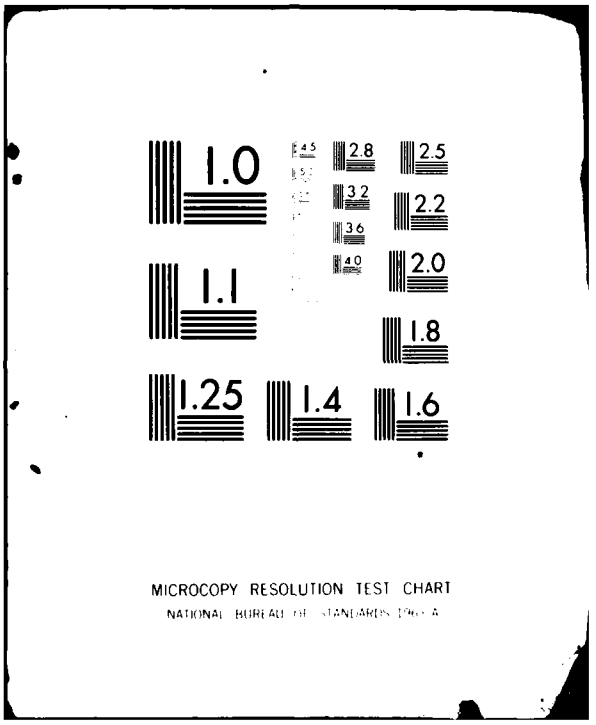
1.0
1.1
1.25
1.4
1.6
1.8
2.0
2.2
2.5
2.8
3.2
3.6
4.0
MICROCOPY RESOLUTION TEST CHART
NATIONAL BUREAU OF STANDARDS 1963-A

LEVEL II

12

DNA 5807F

ANALYSIS OF NUCLEAR PROPAGATION EFFECTS UTILIZING WIDEBAND SATELLITE DATA

Charles L. Rino
Jacqueline Owen
R. C. Livingston

SRI International
333 Ravenswood Avenue
Menlo Park, California 94025

1 April 1981

Final Report for Period 14 January 1980—30 January 1981

CONTRACT No. DNA 001-80-C-0077

APPROVED FOR PUBLIC RELEASE;
DISTRIBUTION UNLIMITED.

THIS WORK SPONSORED BY THE DEFENSE NUCLEAR AGENCY
UNDER RDT&E RMSS CODE B322080462 I25AAXHX64017 H2590D.

Prepared for
Director
DEFENSE NUCLEAR AGENCY
Washington, D. C. 20305

Destroy this report when it is no longer needed. Do not return to sender.

PLEASE NOTIFY THE DEFENSE NUCLEAR AGENCY, ATTN: STTI, WASHINGTON, D.C. 20305, IF YOUR ADDRESS IS INCORRECT, IF YOU WISH TO BE DELETED FROM THE DISTRIBUTION LIST, OR IF THE ADDRESSEE IS NO LONGER EMPLOYED BY YOUR ORGANIZATION.

UNCLASSIFIED

SECURITY CLASSIFICATION OF THIS PAGE (When Data Entered)

REPORT DOCUMENTATION PAGE

READ INSTRUCTIONS BEFORE COMPLETING FORM

1 REPORT NUMBER: DNA 5807F	2. GOVT ACCESSION NO.: AD-A104 688
3 RECIPIENT'S CATALOG NUMBER:	
4. TITLE (and Subtitle): ANALYSIS OF NUCLEAR PROPAGATION EFFECTS UTILIZING WIDEBAND SATELLITE DATA	5 TYPE OF REPORT & PERIOD COVERED: Final Report for Period 14 Jan 80—30 Jan 81
	6 PERFORMING ORG. REPORT NUMBER: SRI Project 1284
7 AUTHOR(s): Charles L. Rino, Jacqueline Owen, R. C. Livingston	8 CONTRACT OR GRANT NUMBER(s): DNA 001-80-C-0077
9 PERFORMING ORGANIZATION NAME AND ADDRESS: SRI International, 333 Ravenswood Avenue, Menlo Park, California 94025	10 PROGRAM ELEMENT, PROJECT, TASK AREA & WORK UNIT NUMBERS: Subtask I25AAXHX640-17
11 CONTROLLING OFFICE NAME AND ADDRESS: Director, Defense Nuclear Agency, Washington, D.C. 20305	12. REPORT DATE: 1 April 1981
	13. NUMBER OF PAGES: 88
14 MONITORING AGENCY NAME & ADDRESS (if different from Controlling Office):	15. SECURITY CLASS (of this report): UNCLASSIFIED
	15a DECLASSIFICATION DOWNGRADING SCHEDULE: N/A

16. DISTRIBUTION STATEMENT (of this Report)

Approved for public release; distribution unlimited.

17. DISTRIBUTION STATEMENT (of the abstract entered in Block 20, if different from Report)

18 SUPPLEMENTARY NOTES

This work sponsored by the Defense Nuclear Agency under RDT&E RMSS Code B322080462 I25AAXHX64017 H2590D.

19. KEY WORDS (Continue on reverse side if necessary and identify by block number)

Scintillation
Striations
Natural ionosphere

20 ABSTRACT (Continue on reverse side if necessary and identify by block number)

Previous analyses of the Wideband Satellite data have emphasized the scale-size regime between 500 m and several tens of kilometers. In this report we describe the results of a detailed analysis of the auroral and equatorial total electron content (TEC) structure associated with the various scintillation phenomena. A nighttime equatorial anomaly was a priminent feature in the equatorial data, particularly as the solar cycle maximum approached. In the auroral data we found that an enhanced F region is the primary contributor to steep latitudinal TEC gradients.

DD FORM 1 JAN 73 1473 EDITION OF 1 NOV 65 IS OBSOLETE

UNCLASSIFIED

SECURITY CLASSIFICATION OF THIS PAGE (When Data Entered)

20. (Continued)

Because recent data have shown an abrupt steepening of the irregularity spectral density function near 500 m, a careful analysis of the mutual coherence function was performed to see if this feature could be detected in the Wideband scintillation data. The analysis did indeed reveal such a feature, which is evidently a permanent characteristic of the most severely disturbed equatorial irregularity continuum.

TABLE OF CONTENTS

TABLE OF CONTENTS (Continued)

LIST OF ILLUSTRATIONS

LIST OF ILLUSTRATIONS (Continued)

LIST OF ILLUSTRATIONS (Continued)

LIST OF TABLES

I EXECUTIVE SUMMARY

Between May 1976 and August 1979--the active data-taking phase of the Wideband Satellite Experiment--an extensive data base was accumulated and analyzed to determine the temporal coherence, spatial coherence, and frequency coherence of naturally occurring ionospheric scintillation and its global morphology. The unique feature of the Wideband satellite experiment was the S-band phase reference, which permitted measuring phase as well as amplitude scintillation at L band, UHF, and VHF.

For striations greater than ~200 m, where diffraction effects can be safely neglected, the Wideband phase-scintillation structure is an integral measure of the in-situ structure along the propagation path. If the shape of the in-situ spectrum of the irregularities does not vary along the propagation path, then the power-law index of the phase spectrum is one plus the corresponding index of the one-dimensional in-situ spectral index. Thus, a k^{-2} in-situ spectrum corresponds to a k^{-3} phase spectrum.

The Wideband satellite data, however, have consistently shown shallower spectral indices than expected that vary systematically with changing perturbation strength. Only recently, in-situ measurements from the Atmospheric Explorer-E (AE-E) satellite and the PLUMEX experiment have demonstrated that the Wideband data correctly predicted the in-situ structure. The PLUMEX rocket data, moreover, have extended the measurements to structures well below 200 m. There, the in-situ spectra roll off more rapidly than expected.

The in-situ spectral-density function evidently has a two-component, power-law shape. For structures smaller than ~200 m, where striation shape dominates, the spectra fall off more rapidly than k^{-2}. For structures larger than ~200 m, where the striation-size distribution dominates, the spectra fall off less rapidly than k^{-2}. This characterization strictly applies only to the most intensely disturbed (high-electron-density)

regions. Bottomside spread F and density fluctuations within equatorial depletions show the expected $k^{-2.3 \pm 0.2}$ power-law behavior, but do not contribute significantly to disturbances on propagation paths that also intercept highly structured, high-density regions.

The Wideband satellite data are clearly dominated by the large-scale structures, which are generally larger than the Fresnel radius. This effect has been intuitively clear from the earliest Wideband measurements. Under this contract, we have carefully analyzed the mutual coherence function, which, in principle, is unaffected by the diffraction effects that distort the phase data. The results show clear evidence of a systematic steepening of the integrated phase spectrum at high frequencies that is consistent with the PLUMEX data.

We have also analyzed the total electron content (TEC) data recorded at Poker Flat, Alaska and the equatorial stations at Kwajalein, Marshall Islands, and Ancon, Peru. The analysis of the auroral-zone data was concentrated on the occurrence and structure of distinct (TEC) boundaries that are evidently associated with an enhanced, unstable F region. The scintillation signature of these regions shows a unique sheet-like anisotropy and recently has generated considerable interest. The equatorial TEC patterns are much more systematic, and reveal a considerable amount of information about the distribution of equatorial ionization and its seasonal and solar cycle variation.

Both the propagation effects and the background ionization structure have ramifications for predicting propagation effects in disturbed nuclear environments. The two-component spectral structure illustrates the importance of establishing where the spectrum becomes distribution dominated rather than edge dominated. The former regime dominates the Wideband scintillation structure, whereas the latter regime is most readily amenable to numerical simulation and theoretical analysis. The analysis of the background ionization structure is important for establishing the relationships between the macroscale and the various microscale structure regimes.

II INTRODUCTION

The active data-taking phase of the Wideband Satellite Experiment was formally completed in August 1979 [Rino et al., 1980]. Extensive data were accumulated and analyzed to determine the temporal coherence, spatial coherence, and frequency coherence of naturally occurring scintillation and its global morphology. The systematic analysis of these data has provided a consistent characterization of the underlying irregularity structure to scale sizes as small as a few hundred meters, beyond which the effects of diffraction severely distort the phase data. The PLUMEX rocket experiment has, moreover, provided in-situ measurements to scale sizes approaching one meter [McDaniel, 1980]. Many of the results were unexpected, however, and it is useful to review the theory that has guided the interpretation of these experimental data.

It is now generally accepted that convective instabilities cause the development of an enhanced continuum of intermediate-scale plasma structures. The gradient-drift and Rayleigh-Taylor instabilities are well-known examples of convective instabilities. When a convective instability is operative, an initially unstable gradient first steepens and then finger-like striations or depletions develop. The size of the primary striations or depletions can vary considerably.

An important finding from numerical simulations of barium striation development is that the size of the primary striations is controlled by the initial gradient [Keskinen et al., 1979]. When the unstable plasma is completely isolated, the primary striations bifurcate, thereby generating smaller structures which themselves bifurcate. This cascade process continues until the fine structure is small enough to be rapidly eroded by classical cross-field diffusion.

The main spectral characteristics of the structure continuum can readily be inferred when such a process is operative. Photographic data suggest that the striation cross-section is essentially rectangular ("top-hat"

like), which leads directly to a k^{-2} one-dimensional spectral-density function (SDF) wherever the steep edges dominate. The canonical SDF is then k^{-2} between an outer-scale wave number corresponding to the primary striation size and an inner-scale wave number corresponding to the ion gyroradius.

An isolated barium cloud does not conform rigorously to this simple picture, however. Numerical simulations by Keskinen et al. [1981] have shown, for example, that a k^{-2} SDF actually occurs only for SDFs measured across the tips of the primary striation. The cross gradient SDFs are somewhat steeper with a spectral index between 2.2 and 2.5. The steeper slopes persist when the structure achieves a quasi-steady isotropic state. These spectral characteristics agree well with bottomside spread F measured during the PLUMEX experiment [Keskinen et al., 1981].

Rapid progress is also being made in understanding the various mechanisms that generate the meter-to-submeter structure responsible for enhanced radar field-aligned backscatter echoes [Ossakow, 1981]. The spectral continuum for naturally spread F, however, is more complex than the spectral continuum for an isolated barium cloud. For example, the power-law spectral indices deduced from the Wideband satellite data have been consistently less than 2, not greater than 2 as would be expected from the totality of numerical simulation studies.

The estimates of the in-situ spectral index are derived from the phase-scintillation spectra and are consistent with the behavior of the intensity scintillation and frequency coherence of the signal under strong scatter conditions. Nonetheless, the scintillation structure responds to the integral of the structure along the entire propagation path. Because of this "geometrical smearing," it was initially thought that the scintillation structure gave a biased estimate of the in-situ spectral index.

Recent comparisons of Wideband satellite data with nearly coincident in-situ measurements using the AE-E satellite have shown, however, that the indirectly inferred shallow and systematically varying spectral indices are indeed characteristic of the in-situ irregularity structures

with scale sizes between several hundred kilometers and several hundred meters [Livingston et al., 1981]. The measured and inferred perturbation strengths show systematic differences, which are attributed to the fact that the AE-E satellite sampled only a single altitude. This feature was demonstrated by the phase and in-situ data from the PLUMEX I rocket, which showed nearly perfect agreement for a near vertical path [Rino et al., 1981].

To reconcile the intermediate-scale measurements, which show a much more shallowly sloped SDF, with the more steeply sloped transition-scale structures, we must postulate a discontinuity in the power-law index between the spatial frequencies corresponding to ~500 m and ~200 m. The PLUMEX I data have provided direct evidence of such a two-component spectrum [Rino et al., 1981; Kelley et al., 1981]. Even the transitio-scale structures, however, show a variable spectral index, in some regions steepening to values as high as 4.

Such departures from the expected behavior of isolated convective instabilities with uniform driving conditions are evidently caused by the very complex environment in which the local instability operates, as has been suggested by Wittwer [1981]. With regard to the transition-scale structure, evidence mounts that the enhanced diffusion inhibits the bifurcation process so that the primary structures persist much longer than expected--the "freezing" phenomenon [McDonald et al., 1980].

The cause of the anomalous diffusion is believed to be E-region coupling, which undoubtedly plays an important role in establishing the structure of auroral-zone scintillation [Vickrey, 1981]. The hypothesis seems reasonable that anomalously enhanced diffusion acting to scale sizes approaching 100 m or more can explain the observed spectral steepening over that measured in isolated bottom side structures.

Turning to the intermediate-scale structures, we first note that in the PLUMEX I data they were most intense in the high-density regions adjacent to the large-scale depletions that are delineated by enhanced radar backscatter. Indeed, evidence mounts that the west wall of the depletion is convectively unstable because of an eastward neutral wind

[Tsunoda, 1981; Singh et al., 1981]. Because the gradient varies with height, the locally unstable regions should have a varying local outer scale. Wittwer [1981] argues that the superposition of the spectra from many such regions can account for the shallow and varying spectral index that characterizes the intermediate-scale irregularity structures.

To summarize, therefore, the Wideband satellite data, the more recent PLUMEX data, and the structure of isolated convective instabilities can be reconciled, at least qualitatively. The break in the spectral slope is formally the point beyond which the SDF becomes dominated by the striation profile and the effects of anomalously enhanced diffusion manifests itself. In the shallowly sloped region, the SDF shape is determined by the configuration of the locally striated subregions. As yet, however, these characteristics have not been verified by simulations.

The potential ramifications for systems are important because the scintillation structure under strong-scatter conditions is a sensitive function of the power-law index. Scintillation effects are generally caused by structures comparable to the Fresnel radius and smaller. This is strictly true, however, only for intensity scintillation under weak-scatter conditions. Under strong-scatter conditions, structures larger than a Fresnel radius, but smaller than the outer scale, dominate the scintillation effects; moreover, the spectral characteristics of the underlying irregularity structure manifests itself most clearly under strong-scatter conditions.

The Wideband satellite data behave as if only the large-scale, shallowly sloped spectral regime were present. This behavior, evidently, is due to the transition region scale sizes in the transition region are larger than the Fresnel radius only at L band and above, where saturated scintillation conditions are rarely observed. Under this contract, we have pursued a more refined analysis of the disturbed Wideband satellite passes to verify these concepts.

In a paper submitted for publication by C. L. Rino and C. H. Liu (1981), we develop a simple set of parameters for the scintillation index

that can be used to determine the characteristics of the dominant spectral regime when only intensity-scintillation data are available. The results reconfirm the shallow slopes. Midlatitude data from ATS-6 recorder at 140 MHz, however, show different characteristics. This is most likely caused by an outer-scale cutoff, but possibly caused by spectral steepening. In any case, it underscores the variability of naturally occurring scintillation producing irregularities.

To test the Wideband satellite data for some manifestation of the transition-scale regime, we have also analyzed the mutual coherence function. The mutual coherence function is important in its own right, because in the Rayleigh scatter limit, it completely characterizes the fading structure at a single frequency. In theory, moreover, the mutual coherence function is independent of the Fresnel radius. Thus, its functional form should directly relate to the underlying irregularity structure.

Our results show that this is strictly true only under conditions of strong scatter. Under weak-scatter conditions the slow, trend-like phase variations distort the mutual coherence function. The results have, nonetheless, provided evidence of a break in the spectral slope that cannot be detected in the phase data alone because of diffraction effects.

In Section III, the results of an analysis of the total electron content (TEC) data from the Poker Flat station are reported. We have concentrated on the occurrence and structure of distinct TEC-boundary features to determine their association with the localized high-latitude scintillation feature that is currently of considerable interest [Rino, 1980; Vickrey, 1981].

Distinct TEC-boundary features occur in approximately 50 percent of the nighttime passes, and are generally manifestations of an enhanced, unstable F region. The TEC gradient is positively correlated with magnetic activity during the summer months, but the correlation reverses sense during the winter months. The occurrence of phase-scintillation enhancements within the boundary region is positively correlated with the magnitude of the TEC gradient.

Section IV reviews the results of TEC studies at two equatorial stations, Ancon, Peru in the American sector and Kwajalein, Marshall Islands in the Pacific sector. A consistent F-layer model is established from which the long-term solar cycle and seasonal dependences of TEC can be analyzed. The overall, large-scale electrodynamic behavior at both stations is consistent with an F-region dynamo driven by thermospheric winds. The dynamo action enhances vertical ionization drift in the evening and generates the irregular latitudinal distribution of TEC known as the equatorial anomaly. During the equinoxes, the TEC shows a strong solar-cycle dependence. Also during these periods, the effects of meridional neutral winds on the anomaly symmetry are clear. During the solstices, when the dynamo is weak, the solar effects are less dominant, and local influences seem to control TEC behavior. The association between TEC and scintillation is also considered. As expected, enhanced TEC is necessary for, but does not ensure, scintillation occurrence. Detailed comparisons suggest that the scintillation occurs when the large-scale TEC distributions are changing.

III THE MUTUAL COHERENCE FUNCTION

A. Introduction

Under conditions of narrow-angle scattering, a wave field, $U(\vec{r})$, that interacts with a randomly irregular medium admits the representation

$$U(\vec{r}) = \mathrm{Re}[u(\vec{\rho}, z) \exp\{ikz\}] \quad , \tag{1}$$

where $u(\vec{\rho}, z)$ satisfies the parabolic wave equation. In Eq. (1), the z axis lies along the propagation direction. The mutual coherence function is generally defined as

$$R_u(\Delta\vec{\rho}; z) \triangleq \langle u(\vec{\rho}, z)\, u^*(\vec{\rho}', z)\rangle \quad , \tag{2}$$

because the correlation of the wavefield along z can be neglected for most applications.

We have tacitly assumed that R_u is independent of location in the transverse plane, although this is never strictly true in practice. Indeed, under the narrow-angle scatter approximation, R_u must satisfy the differential equation

$$\frac{\partial R_u}{\partial z} = -i\, k/2 \left[\nabla_T^2 - \nabla_{T'}^2\right] R_u - 1/2 \frac{\partial D(\vec{\rho}, \vec{\rho}')}{\partial z} R_u \quad . \tag{3}$$

In Eq. (3), $D(\vec{\rho}, \vec{\rho}')$ is the phase-structure function

$$D(\vec{\rho}, \vec{\rho}') = \langle\{\delta\phi(\vec{\rho}) - \delta\phi(\vec{\rho}')\}^2\rangle \quad , \tag{4}$$

where

$$\delta\phi(\vec{\rho}) = -r_e\lambda \int_o^z N_e(\vec{\rho},\ \eta)\ d\eta \quad , \tag{5}$$

r_e is the classical electron radius, $\lambda = 2\pi/k$ is the wavelength, and $N_e(\vec{\rho},\ z)$ is the local electron density.

If D is a function only of $\Delta\vec{\rho}$, then the transverse Laplacian operators in Eq. (3) cancel and

$$R_u(\Delta\vec{\rho};\ z) = \exp\{-\ 1/2\ D(\Delta\vec{\rho})\} \quad . \tag{6}$$

The simple form of Eq. (6) was known long before a full multiple-scatter theory was developed. Booker, Ratcliffe, and Shinn [1950] pointed out that the mutual coherence function (MCF) is invariant under conditions of free-space propagation. Fejer [1953] seems to have first derived Eq. (6). Bramley [1954] later pointed out that Eq. (6) can be deduced immediately from the Gaussian phase-screen model.

The two-dimensional Fourier transform of Eq. (6) gives the spatial spectral-density function of the wave field--the so-called angular spectrum. Under the usual assumption of "frozen" irregularity structures, moreover, the MCF for the complex signal can be obtained by replacing $\Delta\vec{\rho}$ by $\vec{v}\Delta t$, where $\vec{v}$ is the irregularity-drift velocity. The one-dimensional Fourier transform of the temporal MCF gives the Doppler spectrum.

The most general form of the phase-structure function is too cumbrous for use in most computations. Rino [1980], however, shows that

$$D(y) \sim C_{\delta\phi}^2 |y|^{\min(2\nu-1,\ 2)} \quad , \tag{7}$$

where ν is the power-law index parameter for a three-dimensional spectral-density function of the form $C_s q^{-(2\nu+1)}$. The phase-structure constant can be derived from the formula

$$C_{\delta\phi}{}^2 = \frac{C_p}{2\pi}\,(\nu^2 - 4.5\nu + 5.5) \text{ for } 1 \le \nu \le 2 \quad , \tag{8}$$

where

$$C_p = r_e{}^2 \lambda^2 \ell_p \, C_s \quad . \tag{9}$$

In Eq. (9), ℓ_p is the length of the propagation path.

The effects of anisotropy can be accommodated by replacing y for $v_{eff}\delta t$, and multiplying C_p by G, where v_{eff} is the effective velocity parameter, and G is a coherent amplification factor defined in Rino (1979a). The main point is that a detailed measurement of the MCF can provide information about the underlying irregularity structure that is unencumbered by a complicated dependence on the Fresnel radius, as is the case when intensity or phase statistics are used.

The Wideband satellite data provide a unique opportunity to measure the mutual coherence function. The S-band reference frequency is essentially undisturbed even under conditions of very strong scatter at VHF and UHF. Moreover, under saturated-scatter conditions ($S_4 \sim 1$), it is generally assumed that Rayleigh scattering prevails. In that case, the MCF is sufficient to completely specify the signal statistics at a single frequency.

B. Data Analysis

To compute the MCF, we have used Wideband satellite data sampled at a 250-Hz rate. The amplitude and phase data were separately detrended using a 25-s (0.04-Hz) cutoff. This step is particularly important in computing the MCF because it effectively establishes the local-phase reference. To compute the actual MCF, we first compute the Doppler spectrum using a standard FFT algorithm. A second Fourier transform then gives the mutual coherence function estimate.

The Doppler spectrum is very nearly symmetric. Thus, to force a purely real MCF, we have averaged the positive and negative frequencies together before computing the final FFT. A standard window function was

also applied to the detrended data to minimize sidelobe effects. Examples of the Doppler spectra and the corresponding MCFs for typical moderate and strong disturbances are shown in Figures 1(a) and (b), respectively.

The left-most frames show the Doppler spectra on log-linear plots. The data have been normalized to unit average intensity over the 16-s data interval. Thus, the integral of the Doppler spectrum is unity. The reduction in intensity of the low-frequency spectral components and the attendant spectral broadening induced by strong scattering is clearly evident. The middle frame shows the same Doppler spectra on a log-log plot. For clarity of presentation, however, the negative frequencies have been offset by 20 dB.

As might be expected, the higher frequencies show a power-law regime with the same power-law index as the integrated-phase spectrum. The lower frequencies are distorted, however, and bear no simple relation to the integrated-phase spectrum. Nonetheless, the shift of the spectral content to higher frequencies with increasing perturbation strength is conspicuous in both the semi-log and log-log displays.

Now, to the extent that Eq. (6) is strictly applicable, the phase spectrum can be extracted by first taking the logarithm of the MCF and then computing the Fourier transform of the result. The problem is that the measured MCFs are not strictly positive as the righthand frames of Figures 1(a) and 1(b) show. Indeed, for the weak perturbation the negative excursion appears to be systematic.

In retrospect, this result might have been expected. The phase-structure function, in fact, any measured-structure function, is a function of $\Delta\vec{\rho}$ only to some maximum separation. In a simple homogeneous environment, the phase-structure function converges to twice the rms phase at this point. In practice, trend-like phase variations upset this convergence, and the structure function does not remain position- or time-invariant for large separations. Under such conditions, Eq. (3) implies a weak dependence on the Fresnel radius. Under strong-scatter conditions, decorrelation occurs sufficiently rapidly that the non-stationary component can evidently be neglected.

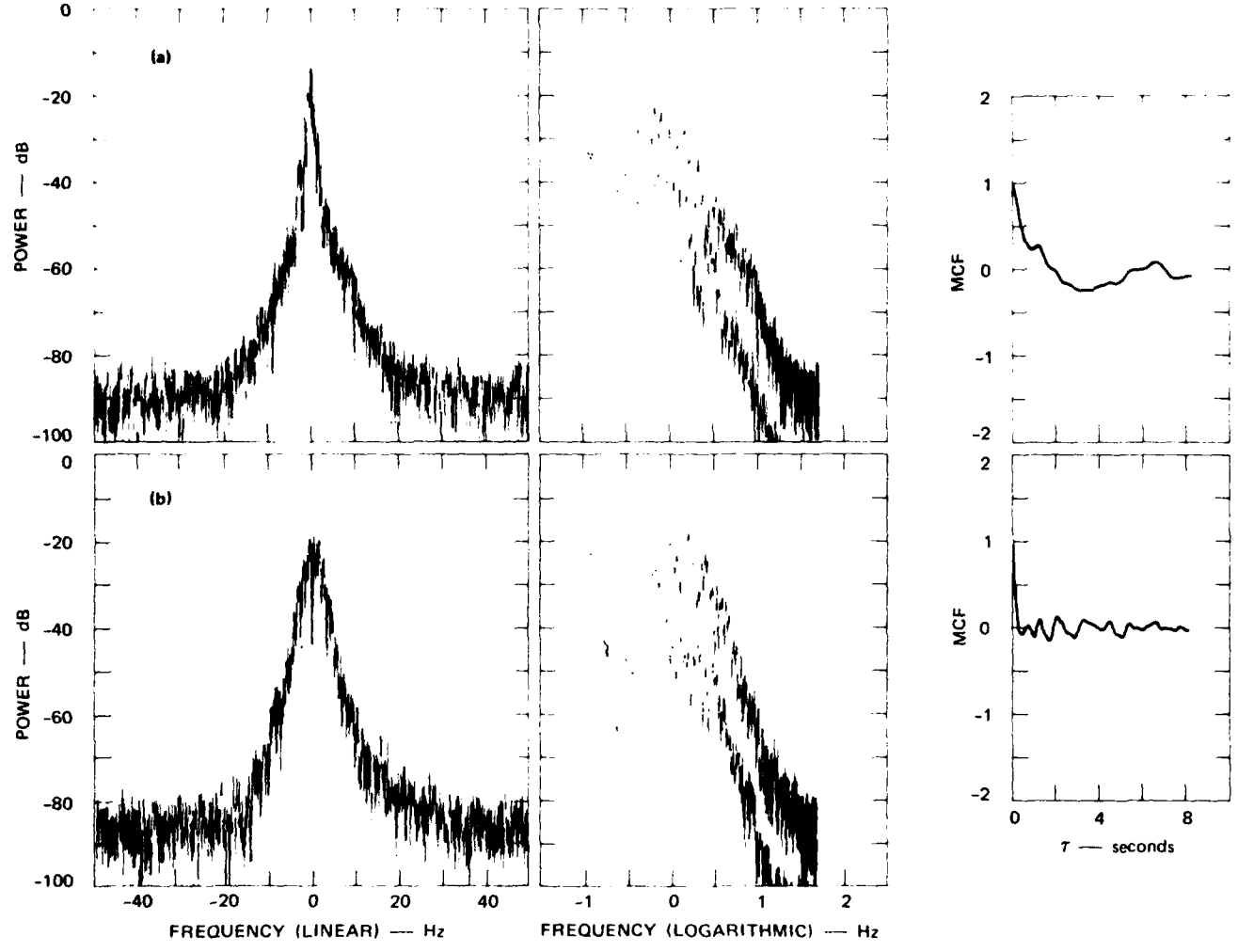

FIGURE 1 MEASURED WIDEBAND SATELLITE VHF DOPPLER SPECTRA AND MUTUAL COHERENCE FUNCTION, (a) WEAK SCATTER (T = -11.5 dB) AND (b) STRONG SCATTER (T = 0.5 dB)

Because a single MCF estimate is itself a random function, we must average many estimates together to determine the functional form of the underlying MCF. Each measured MCF is first corrected for wavefront curvature effects as described in Rino and Owen [1980(b)]. All other geometrical effects scale in exactly the same way as does the phase turbulent strength parameter, T, described in Fremouw et al. [1978], [see also Rino and Owen (1980a)]. Thus, the corrected MCFs with common T values should be statistically similar.

We have, therefore, sorted the corrected MCF estimates by turbulent strength as deduced from the corresponding phase spectra and averaged the results. The upper frames in Figure 2 show the results derived from the more disturbed portions of 24 passes recorded at Ancon, Peru. To the extent that the form implied by Eq. (6) and (7) is correct, a log-log plot of the base e logarithm of the MCF should be linear. Thus, in the lower frames in Figure 2, we have generated such a plot for the strictly positive portion of the measured and averaged MCFs, together with a linear least-squares fit to the resultant curve.

The corresponding weak-scatter data are shown in Figure 3. Here we see a distinct and systematic negative tail. Nonetheless, the strictly positive portion adheres quite well to the exponential power-law model. The varying termination of the MCFs is caused by the spherical wavefront correction.

Data recorded at the Wideband station in Kwajalein have also been processed in this manner. To summarize the results, in Figures 4 and 5, we have plotted the index parameter derived from the linear fit to the log-log plots of the base e logarithm of the measured MCFs. The time to 50-percent decorrelation, τ_v, is also shown. The straight line superimposed on the plot of ν versus T is the empirically derived relation obtained from the Wideband AE-E data comparisons. The solid curve superimposed on the τ_v versus T plot is the theoretical curve derived from Eq. (6) and Eq. (7), but using the ν value computed from the empirical ν versus T relation rather than the measured value.

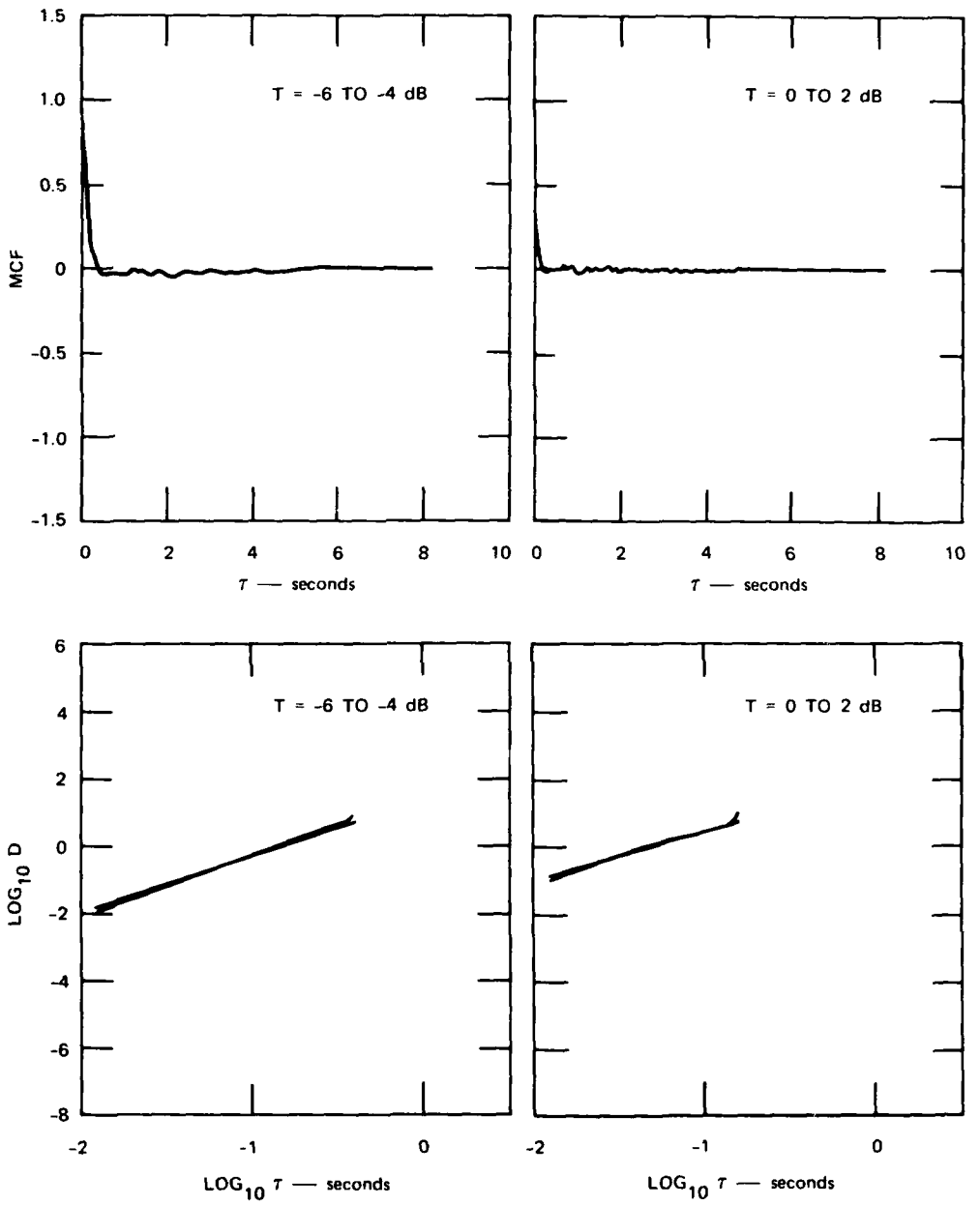

FIGURE 2 STRONG SCATTER MCFs FROM ANCON DATA TOGETHER WITH LOG-LOG PLOTS OF ESTIMATES OF PHASE-STRUCTURE FUNCTION. The straight lines are linear least-squares fits to the data.

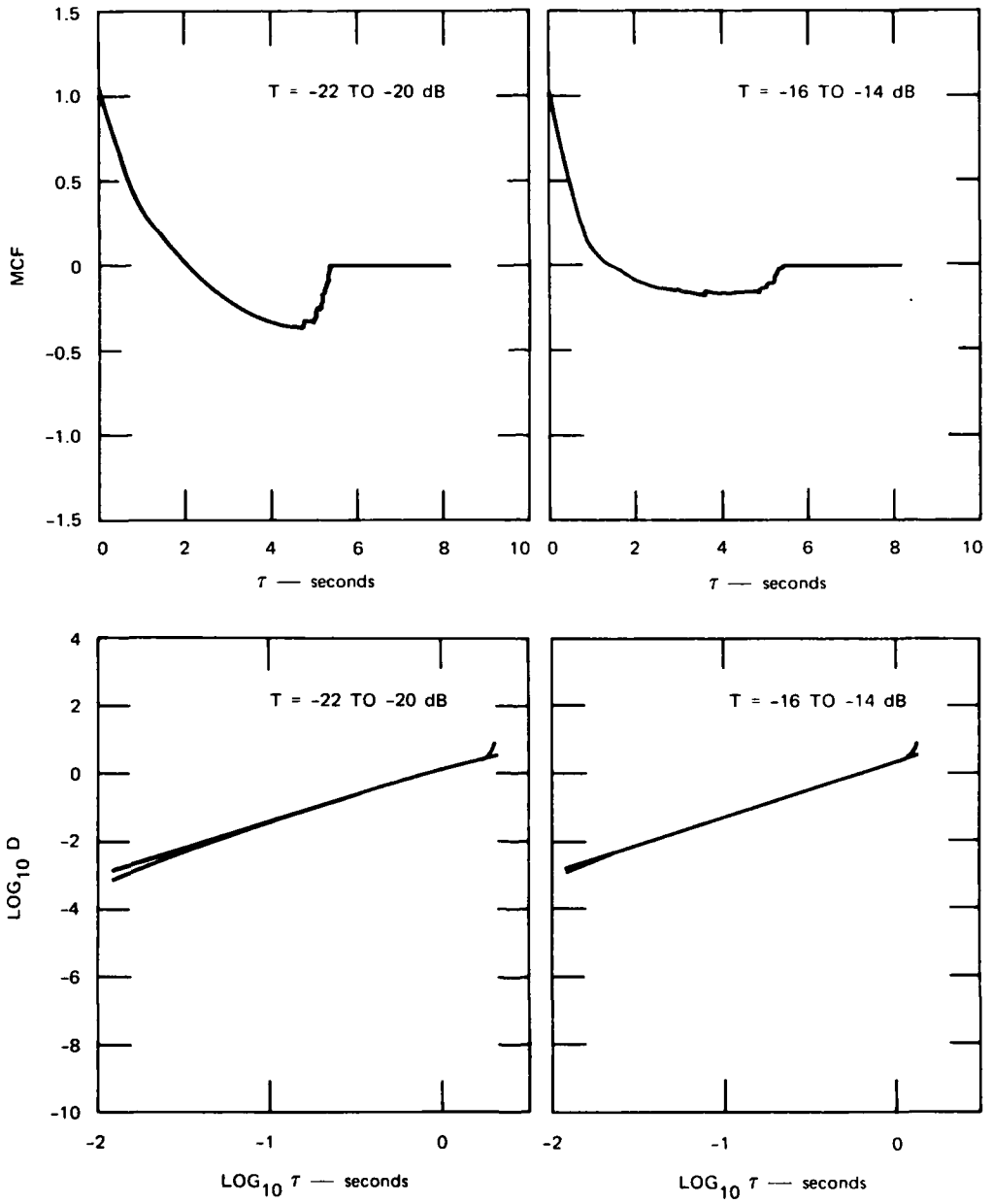

FIGURE 3 WEAK-SCATTER MCFs FROM ANCON DATA SHOWING SYSTEMATIC NEGATIVE TAIL

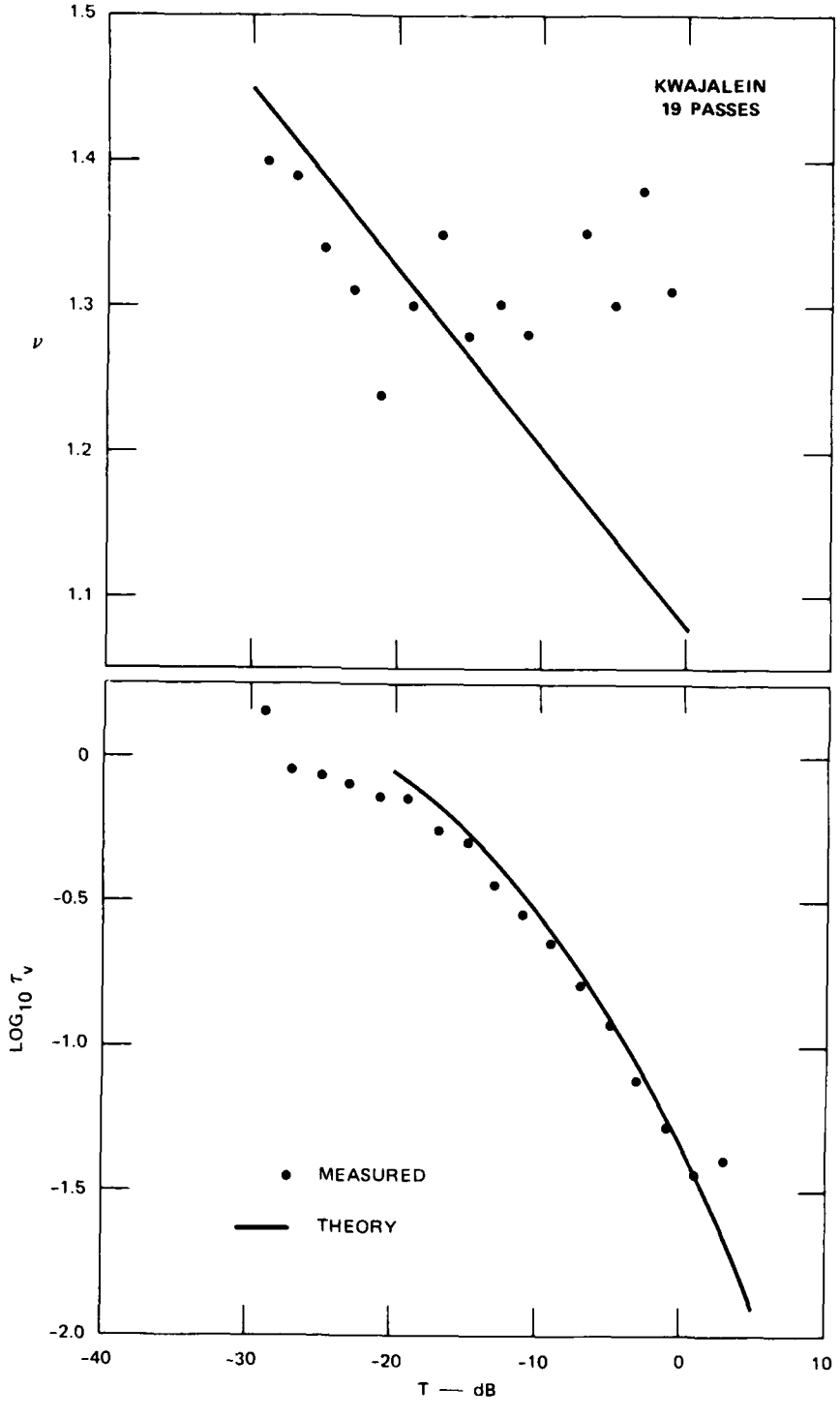

FIGURE 4 SUMMARY PLOT FOR KWAJALEIN DATA SHOWING TIME LAG TO 50-PERCENT DECORRELATION AND SPECTRAL-INDEX PARAMETER DERIVED FROM LOG LINEAR LEAST-SQUARES FIT TO ESTIMATE OF PHASE-STRUCTURE FUNCTION

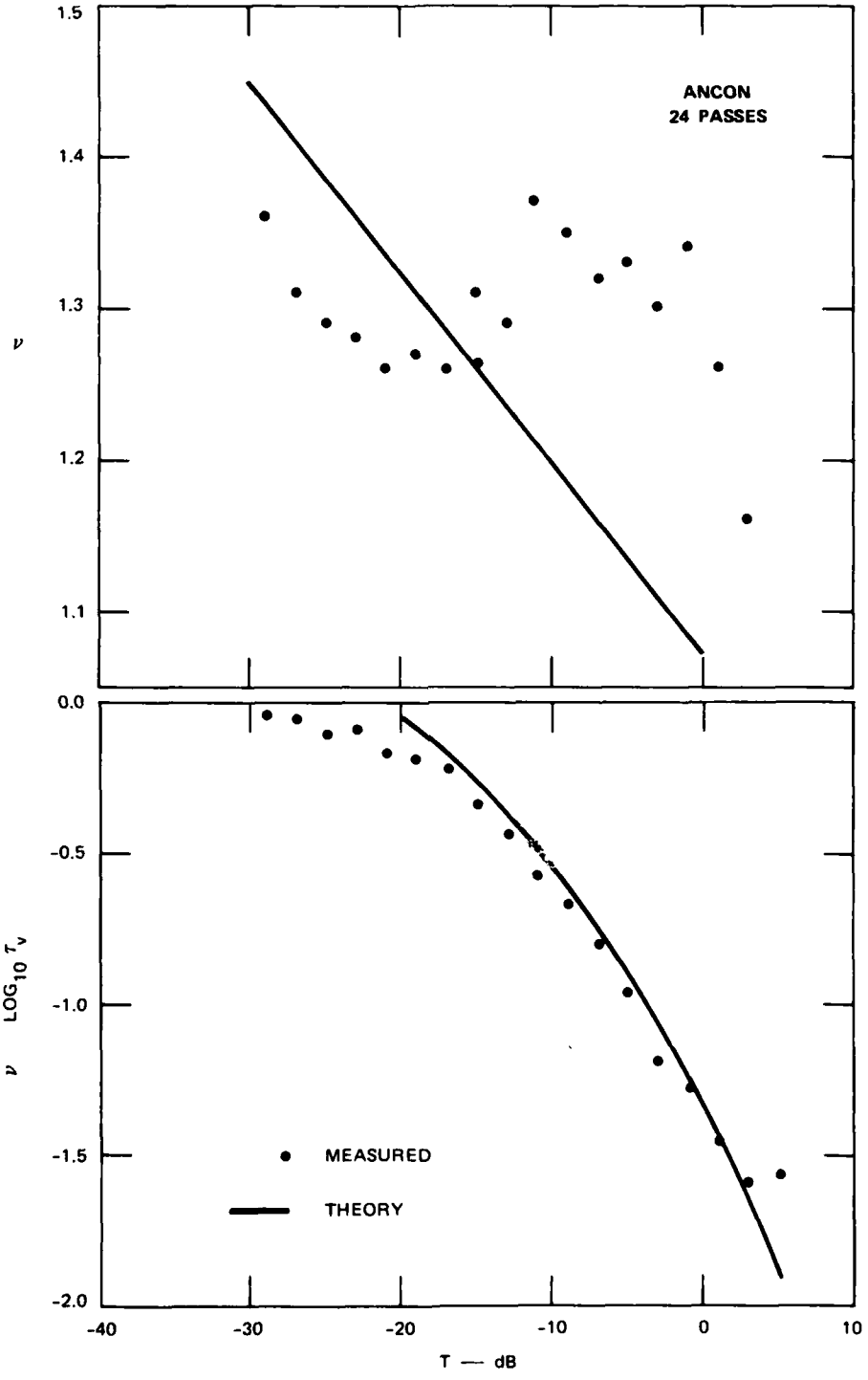

FIGURE 5 SUMMARY PLOT FOR ANCON DATA SHOWING TIME LAG TO 50-PERCENT DECORRELATION AND SPECTRAL-INDEX PARAMETER DERIVED FROM LOG LINEAR LEAST SQUARES FIT TO ESTIMATE OF PHASE-STRUCTURE FUNCTION

The empirically derived ν versus T curve fits the weakly to moderately disturbed Kwajalein data [$T \lesssim -15$ dB in Figure 4] very well. Thus, in this range, the MCF is consistent with the independently processed phase data and the AE-E satellite in-situ data. For the more disturbed data, the inferred spectral index steepens. Intuitively, the behavior is expected if the in-situ SDF had an abrupt change in the power-law slope.

This feature evidently does not manifest itself in the behavior of τ_V, since the τ_V versus T data follow the theoretical computations based on the empirically derived ν versus T curve, except for the last data point. The resolution limit for $\log_{10}\tau_V$ is -2.4. In any case, τ_V is derived from a single point, whereas ν is derived from a range of MCF values. Moreover, the behavior of the MCF for a two-component SDF need not give rise to a simple disjointed two-component MCF.

In the Ancon data shown in Figure 5, the behavior of τ_V versus T is virtually identical to the Kwajalein data. However, the τ_V versus T curve shows pronounced departures from the empirically derived T versus ν curve. We conclude that when comparatively simple measures are used, e.g., τ_V, that MCF theory and data agree well. A more refined measure of the MCF structure, however, shows evidence of a more complex high-frequency SDF behavior, in particular, a steepening of the spectral index.

To illustrate this effect directly in Figure 6, we show a single power-law SDF superimposed on a two-component power-law SDF together with the corresponding MCFs and the log-log display of the corresponding phase structure function. The computations were all done numerically. The measured τ_V parameter agrees to two decimal places for the two SDFs. In the log-log display, however, a steepening of the power-law slope at short lags is clearly evident. Such behavior completely explains the data shown in Figures 4 and 5.

As noted earlier, a Rayleigh process is completely characterized by the MCF. In particular, $S_4 = 1$ and

$$\langle II' \rangle - 1 = |R_u(\Delta t)|^2 \quad , \tag{10}$$

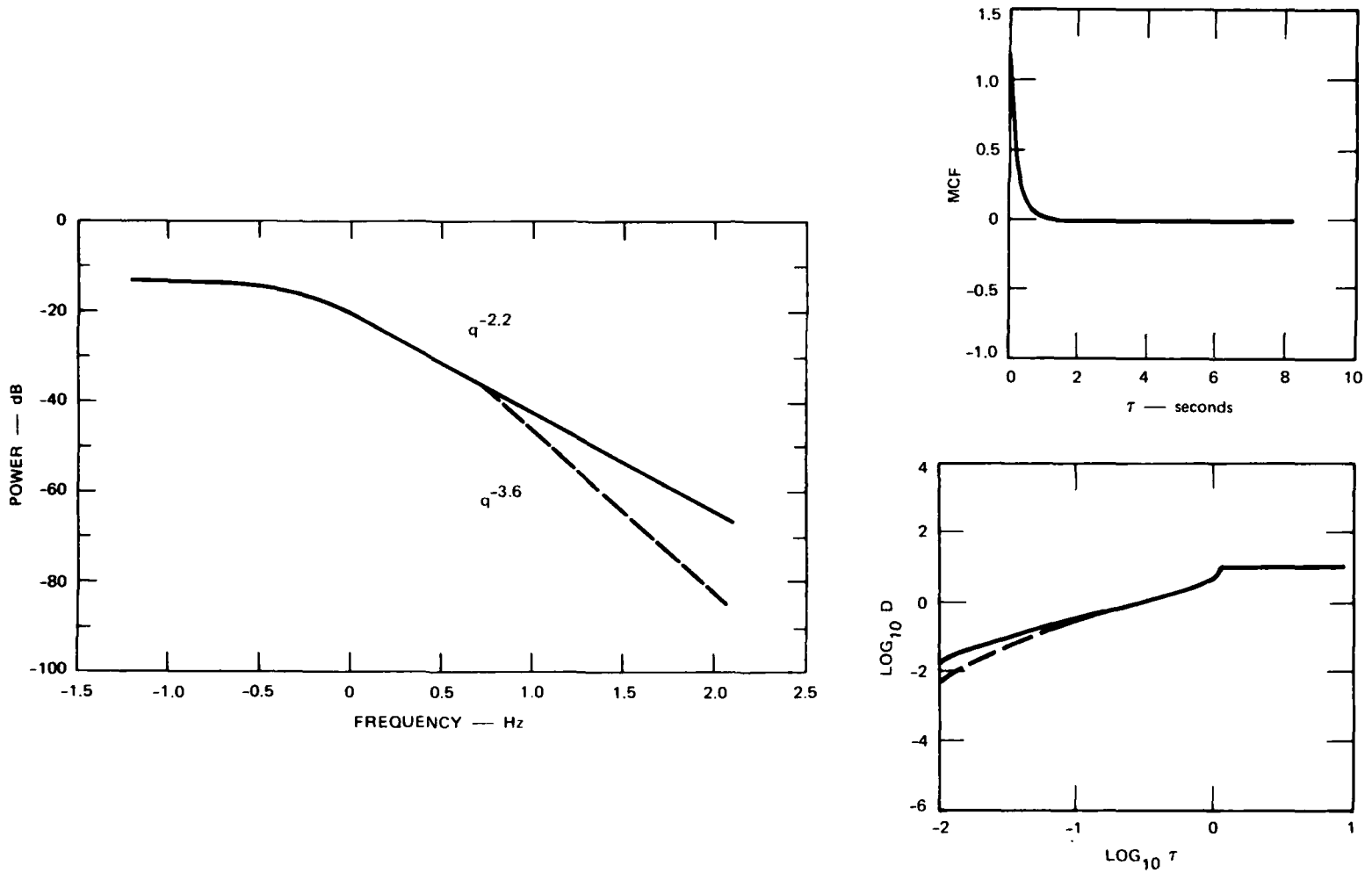

FIGURE 6 NUMERICAL COMPUTATION SHOWING THE EFFECT OF A DISCONTINUITY IN THE POWER-LAW INDEX

where I is the signal intensity normalized to unity average. Strictly speaking, Eq. (10) is a necessary but not sufficient condition. Rino (1979b) shows that Eq. (10) is the strong-scatter limit as long as the power-law index for phase is less than 3.

Because the dominant irregularity structures fall well within this limitation, Eq. (10) should apply to saturated ionospheric scintillation. This was verified indirectly in Rino and Owen (1980a, 1981) by plotting τ_I versus T, where τ_I is the time interval to 50-percent decorrelation of intensity. The data agreed very well with theoretical predictions based on Eqs. (6), (7), and (10).

The model implies a simple relationship between τ_I and τ_V under strong-scatter conditions. To verify this, we have averaged the corrected τ_V measurements in exactly the same way as the τ_I measurements that were reported in Rino and Owen (1981a) were processed. The results are shown in Figures 7 and 8. As before, the solid curves are derived from theory, but use the empirically derived relation between ν and T. As predicted, the τ_V data are simple displacements of the corresponding curves in Rino and Owen (1981).

C. Discussion

In this section we have presented the first detailed MCF computations using ionospheric radiowave scintillation data. It has been known from the time of the early development of radiowave scintillation theory that the MCF is invariant under free space propagation and independent of the Fresnel radius. Thus, it has attractive properties for diagnostic purposes. Our results show, however, that slow, trend-like phase variations disrupt the simple form of the MCF, particularly under weak-scatter conditions. For shorter time delays where the measured MCFs are strictly positive, however, the theory fits very well.

The structure of the MCF for short time lags verifies the dominant spectral characteristics of the intermediate-scale irregularities inferred independently from the Wideband phase data. Moreover, the MCF structure

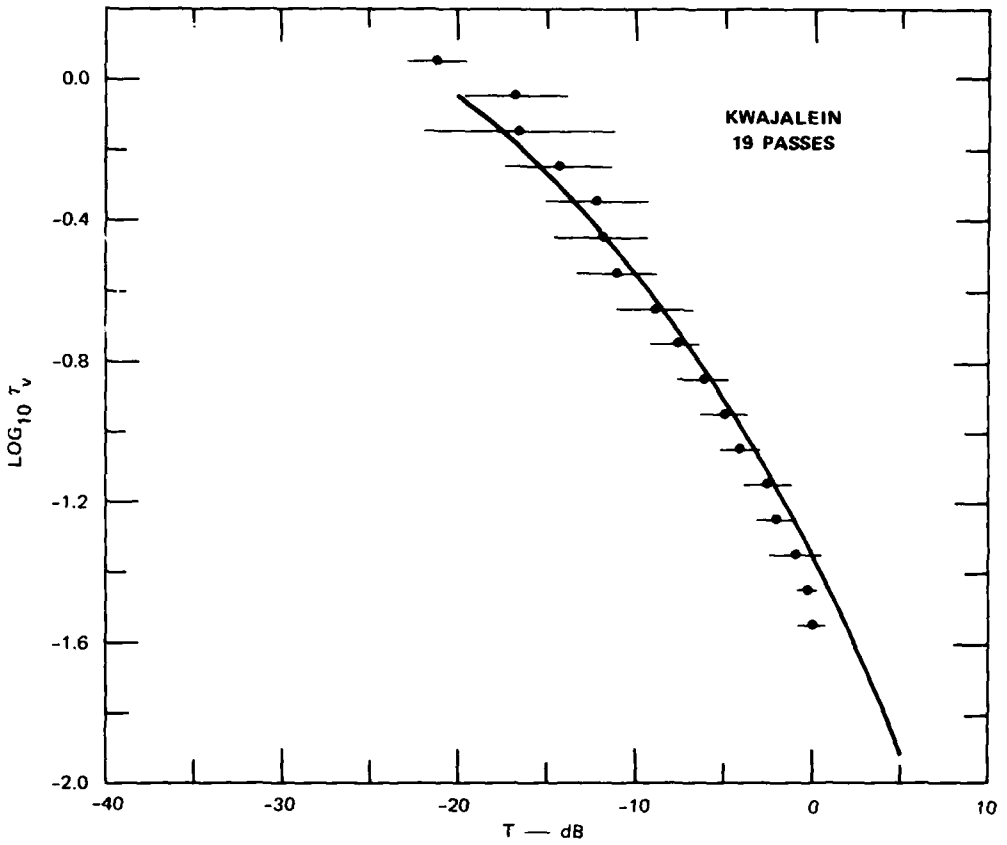

FIGURE 7 PLOT OF TIME LAG TO 50-PERCENT DECORRELATION vs SPECTRAL STRENGTH FROM KWAJALEIN DATA

showed evidence of spectral steepening at high spatial frequencies. This feature has not been detected in the Wideband phase data, evidently because of diffraction effects. A steepening of the power-law slope near 500 m was, however, directly measured in the PLUMEX I rocket data.

Finally, our results verify the use of the Rayleigh model for predicting the coherence time of radiowave scintillation under saturated ($S_4 \sim 1$) conditions. A straightforward extension of the model can be used to compute the Doppler spectrum or the angular spectrum of plane waves.

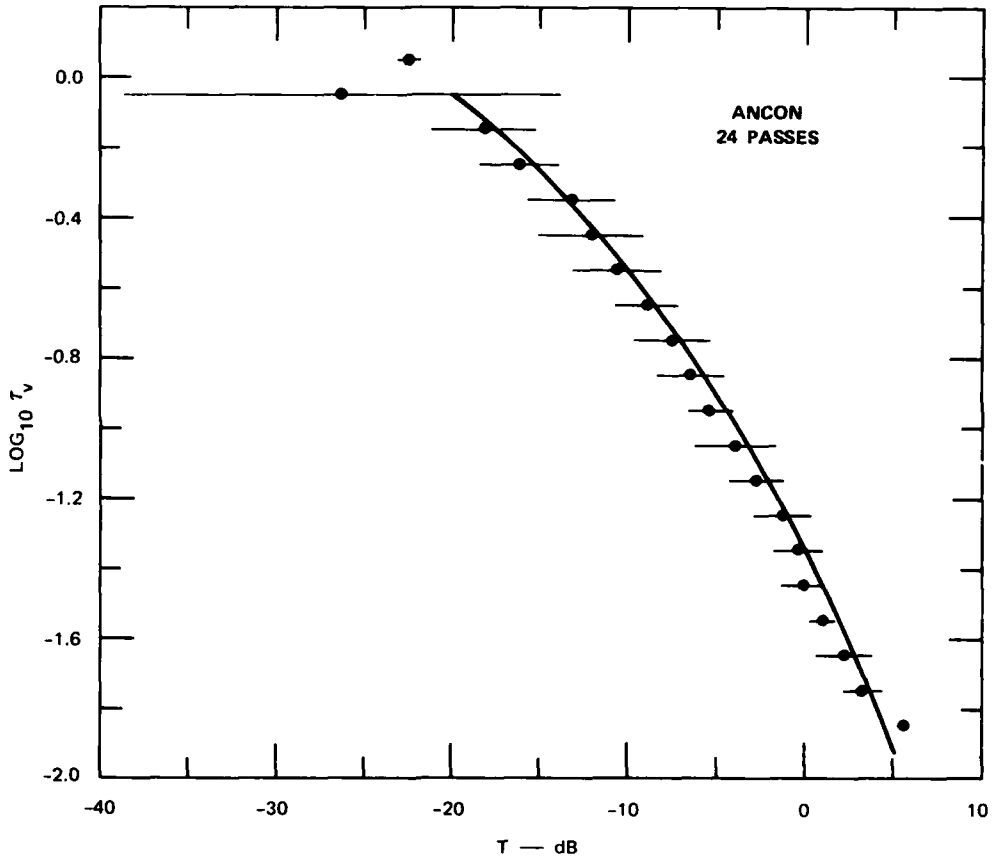

FIGURE 8 PLOT OF TIME LAG TO 50-PERCENT DECORRELATION vs SPECTRAL STRENGTH FROM ANCON DATA

IV AURORAL-ZONE TEC STRUCTURE

A. Introduction

In this section we shall report the results of a summary analysis of the high-latitude total electron content (TEC) structure as measured by the Wideband satellite. The scintillation morphology as measured by Wideband has received considerable attention, particularly the prominant nighttime enhancement that has been attributed to an unstable F region containing sheet-like irregularities [see Rino et al. (1980) and the references cited therein]. We have, therefore, concentrated on the TEC structures that can be associated with this phenomenon. Indeed, the F-region source was first identified by using multiple-station TEC measurements [Rino and Owen, 1980b].

One component of the nighttime auroral-zone particle precipitation sustains an enhanced E layer over a broad latitudinal region. The optical signature of this precipitation is called the diffuse aurora. The more dynamic discrete auroras generally lie poleward of the diffuse auroras, but they can penetrate into the region of the diffuse auroras during substorms.

The equatorial edge of the diffuse aurora is a well-defined feature in both optical and particle precipitation data. The boundary migrates equatorward with increasing magnetic activity [Dandekar, 1979]. Moreover, the ionization associated with the diffuse aurora is a prominent feature in the Chatanika radar data [Vondrak and Baron, 1976].

We, therefore, expect the diffuse auroral boundary to be a prominent feature in TEC data measured by using polar orbiting satellites. We have found, however, that the F-region ionization associated with the aforementioned instability [Vickrey, 1981] dominates the TEC boundary structure.

B. The Occurrence and Location of TEC Boundaries

In Figure 9, we show two nighttime Wideband satellite TEC records that have well-defined TEC boundaries. The data are presented here in units of relative phase change. To characterize the boundary, the minimum and maximum locations have been identified (see Figure 9) together with the corresponding change in TEC units.

As discussed in Section III-A, the presence of an enhanced F-layer complicates the interpretation of the boundary. As a guideline, therefore, we have performed model computations similar to those used in Rino and Owen [1980b]. In Figures 10, representative trough and diffuse auroral electron density profiles are shown together with a meridional profile of the corresponding density contours are shown. The resulting TEC variation is shown in Figure 11.

The results of a similar set of computations for an enhanced F layer is shown in Figures 12 and 13. The main difference is that the F region produces a much larger gradient. The location of the boundary relative to the station is also important as can be seen from Figures 14 and 15. The F-region boundary is visible from approximately 70° magnetic latitude, whereas the E-region boundary is only vislble from a few degrees poleward of the station. We conclude that the occurrence of a well-defined TEC boundary is heavily weighted toward F-region contributions, particularly when the gradient is large and observed poleward of the station.

With this in mind, we consider the occurrence of TEC boundaries in the nighttime Wideband passes recorded at Poker Flat from May 1976 through May 1979. The summary data are shown in Figure 16. A TEC boundary is present in approximately 50 percent of the passes, irrespective of season or solar-cycle epoch.

The location of the boundary is shown in Figure 17. The TEC boundary moves equatorward with increasing activity, but generally maintains a constant latitudinal extent. The more disturbed passes show an additional small equatorward migration with increasing solar activity. The three-year period from 1976 to 1979 is generally one of increasing solar activity as the 1980 maximum of solar cycle 21 was approached.

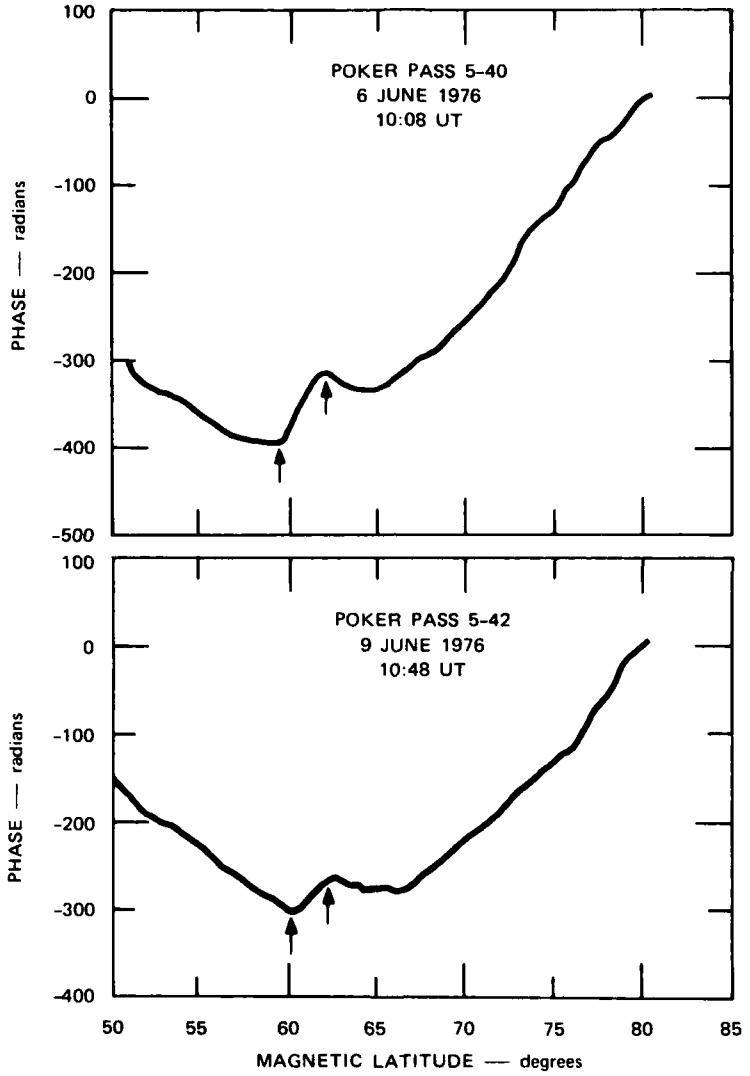

FIGURE 9 TYPICAL NEAR-MERIDIONAL, HIGH-LATITUDE TEC VARIATIONS SHOWING BOUNDARY FEATURE (ARROWS INDICATE MINIMUM AND MAXIMUM BOUNDARY LOCATIONS)

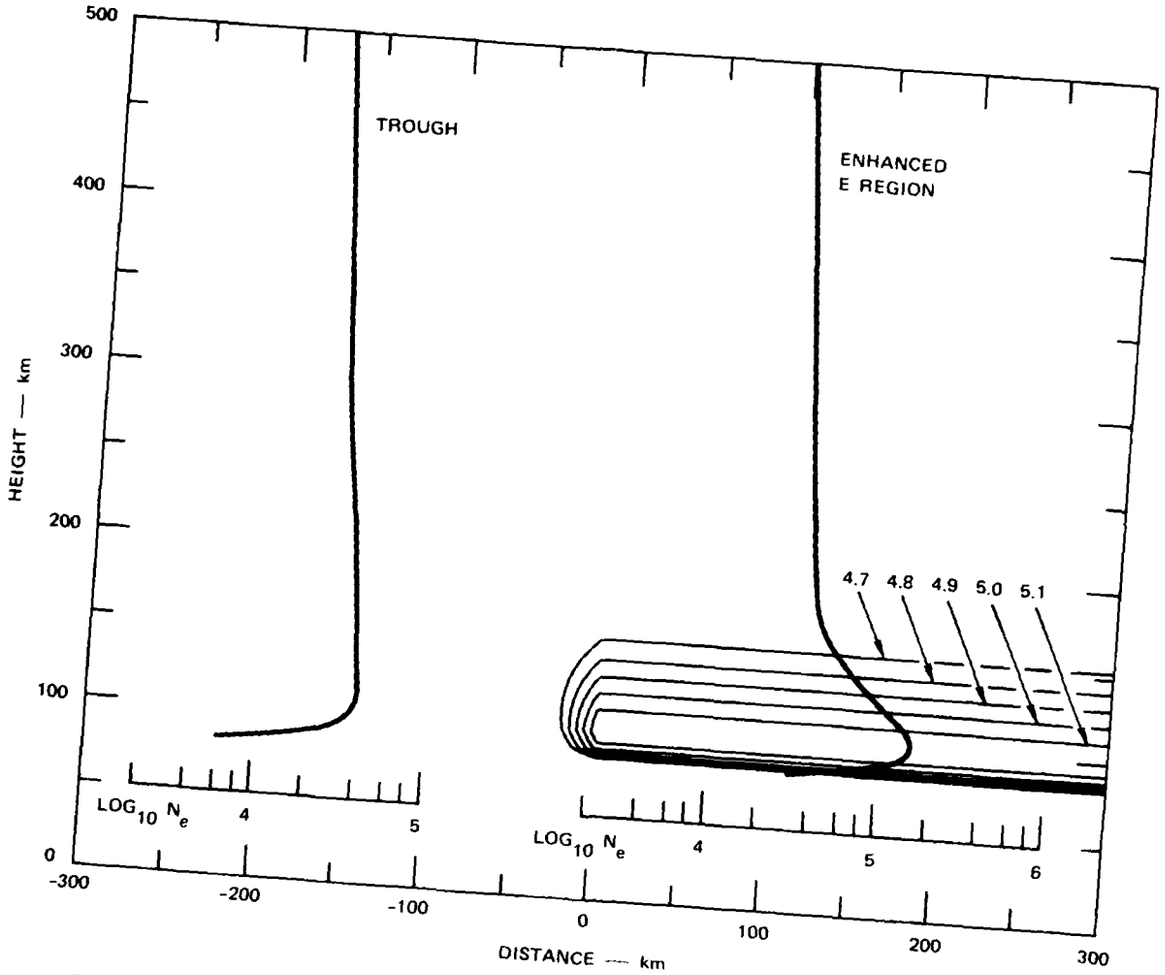

FIGURE 10 UNIFORM DIFFUSE AURORAL E-REGION IONIZATION DISTRIBUTION

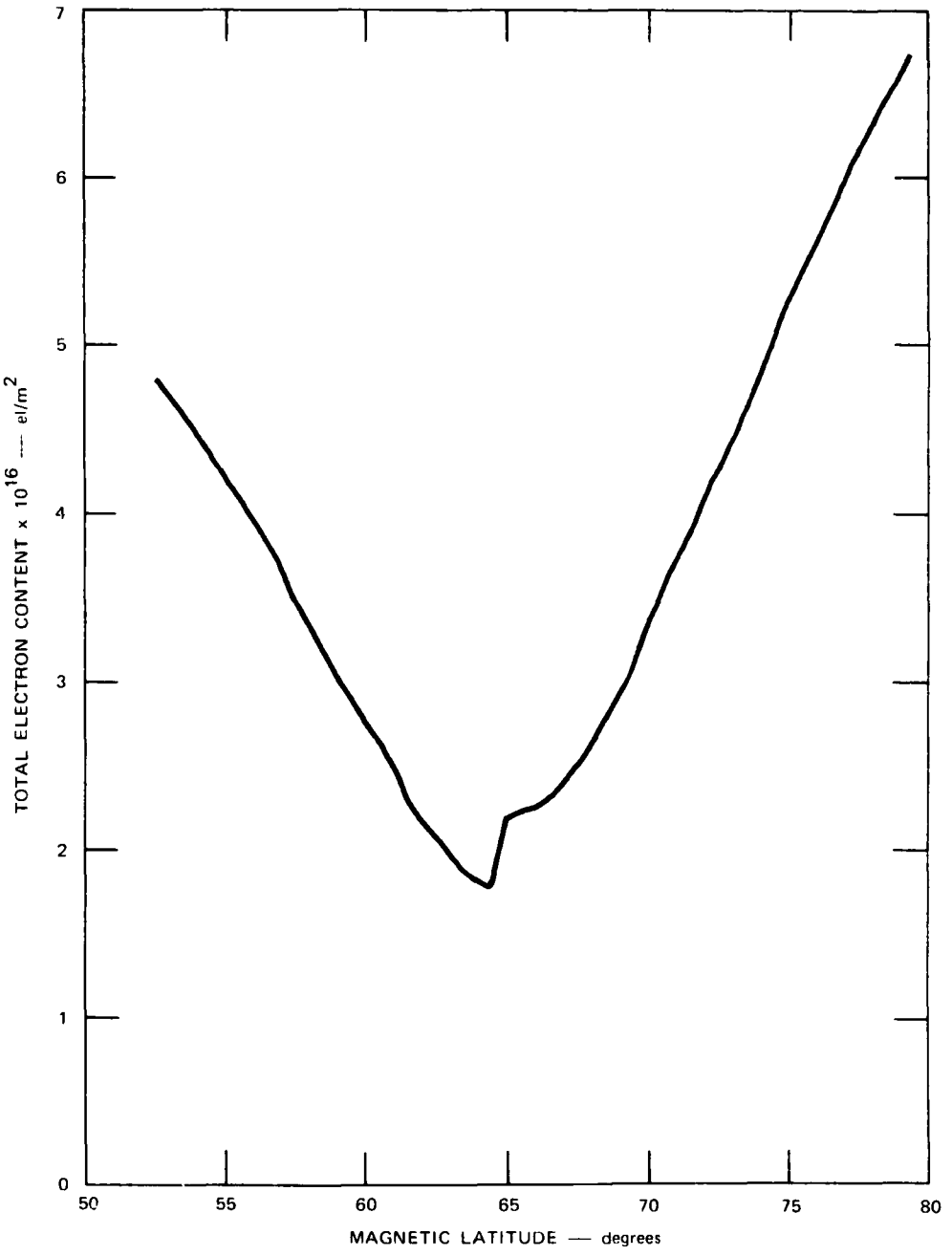

FIGURE 11 CALCULATED MERIDIONAL TEC PROFILE FOR E-REGION IONIZATION

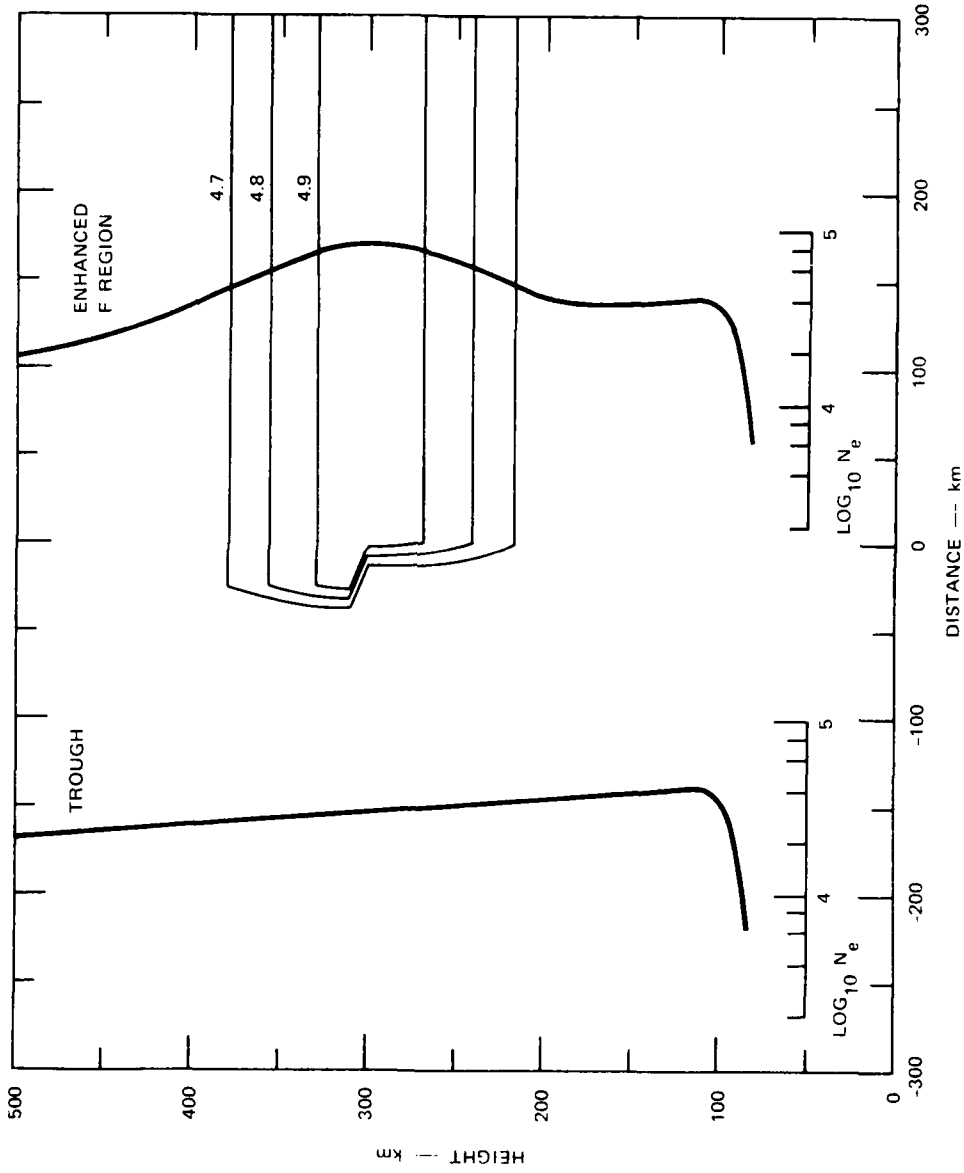

FIGURE 12 UNIFORM AURORAL ENHANCED F-REGION IONIZATION PROFILE

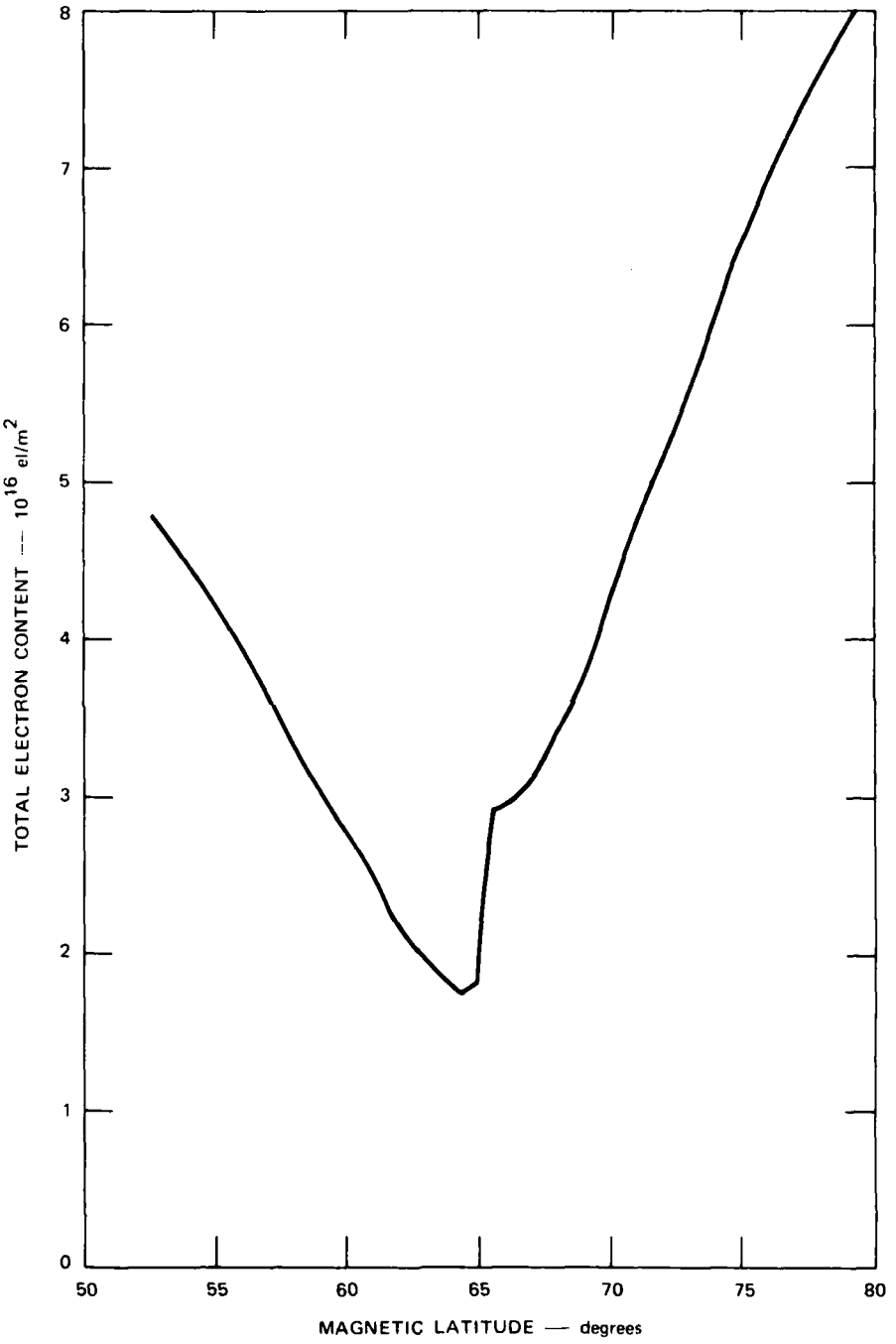

FIGURE 13 CALCULATED MERIDIONAL TEC PROFILE FOR ENHANCED F REGION

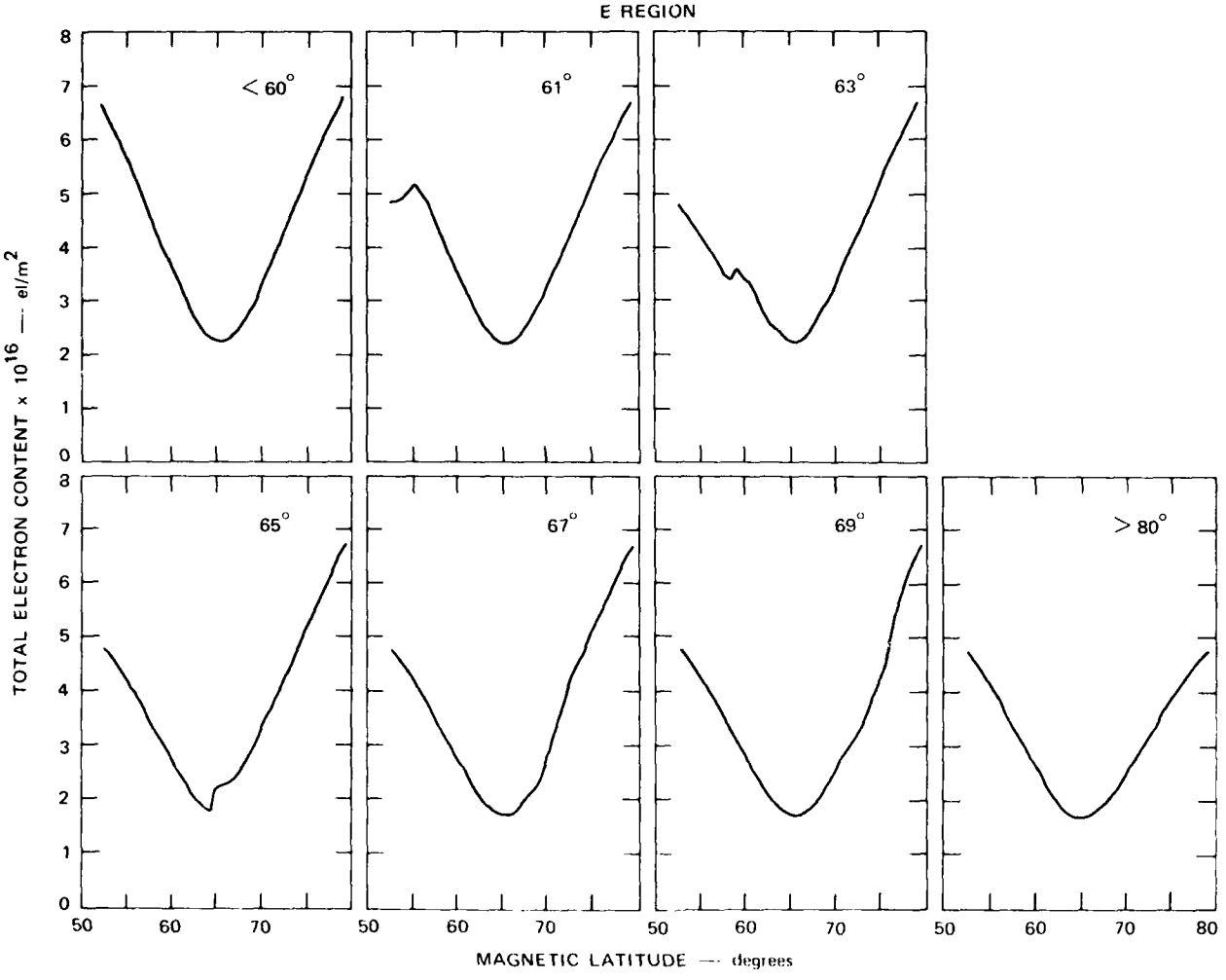

FIGURE 14 POKER FLAT COMPUTED TEC PROFILES SHOWING EFFECT OF VARYING DIFFUSE AURORAL BOUNDARY LOCATION

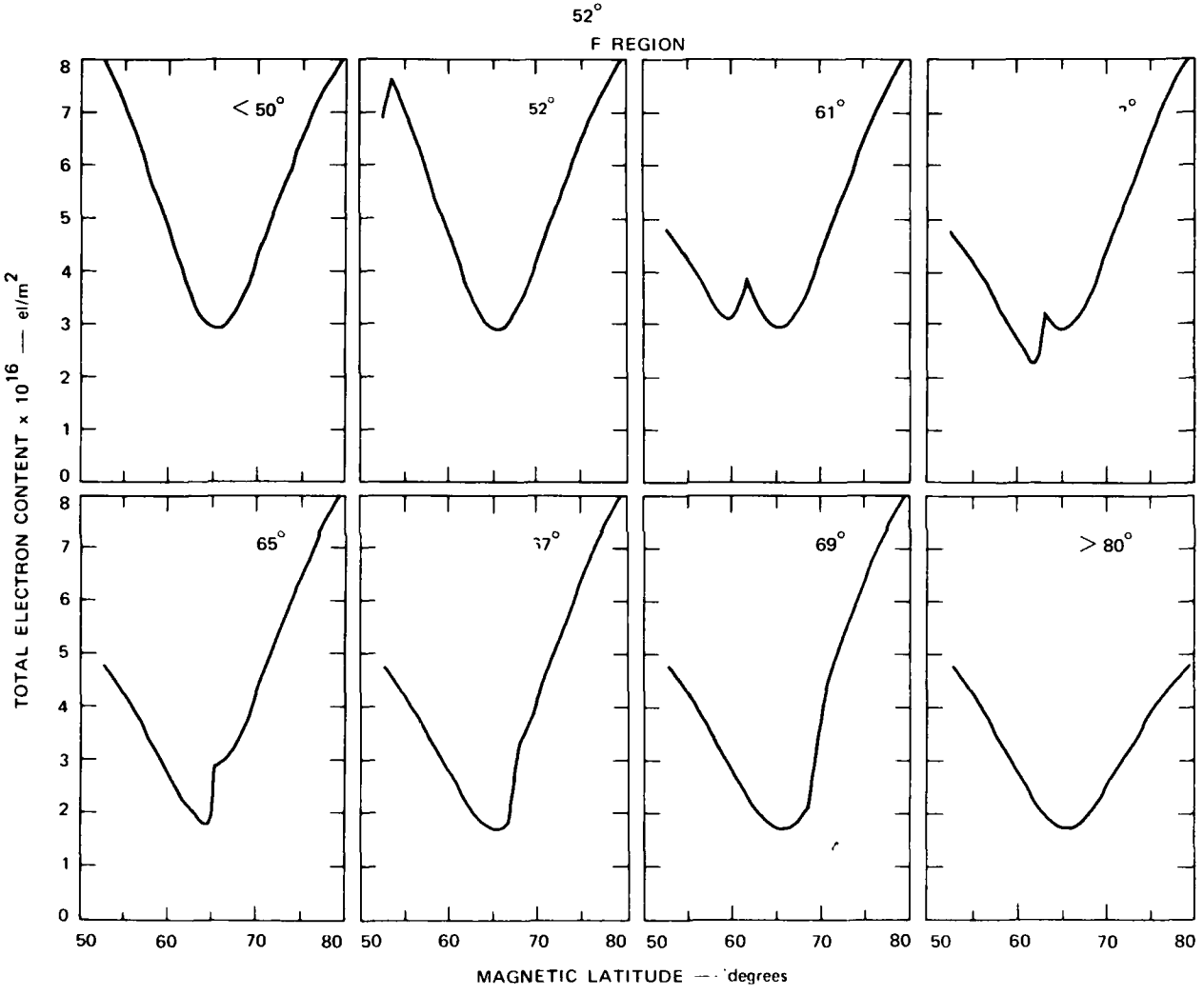

FIGURE 15 POKER FLAT COMPUTED TEC PROFILES SHOWING EFFECT OF VARYING ENHANCED F-REGION BOUNDARY LOCATION

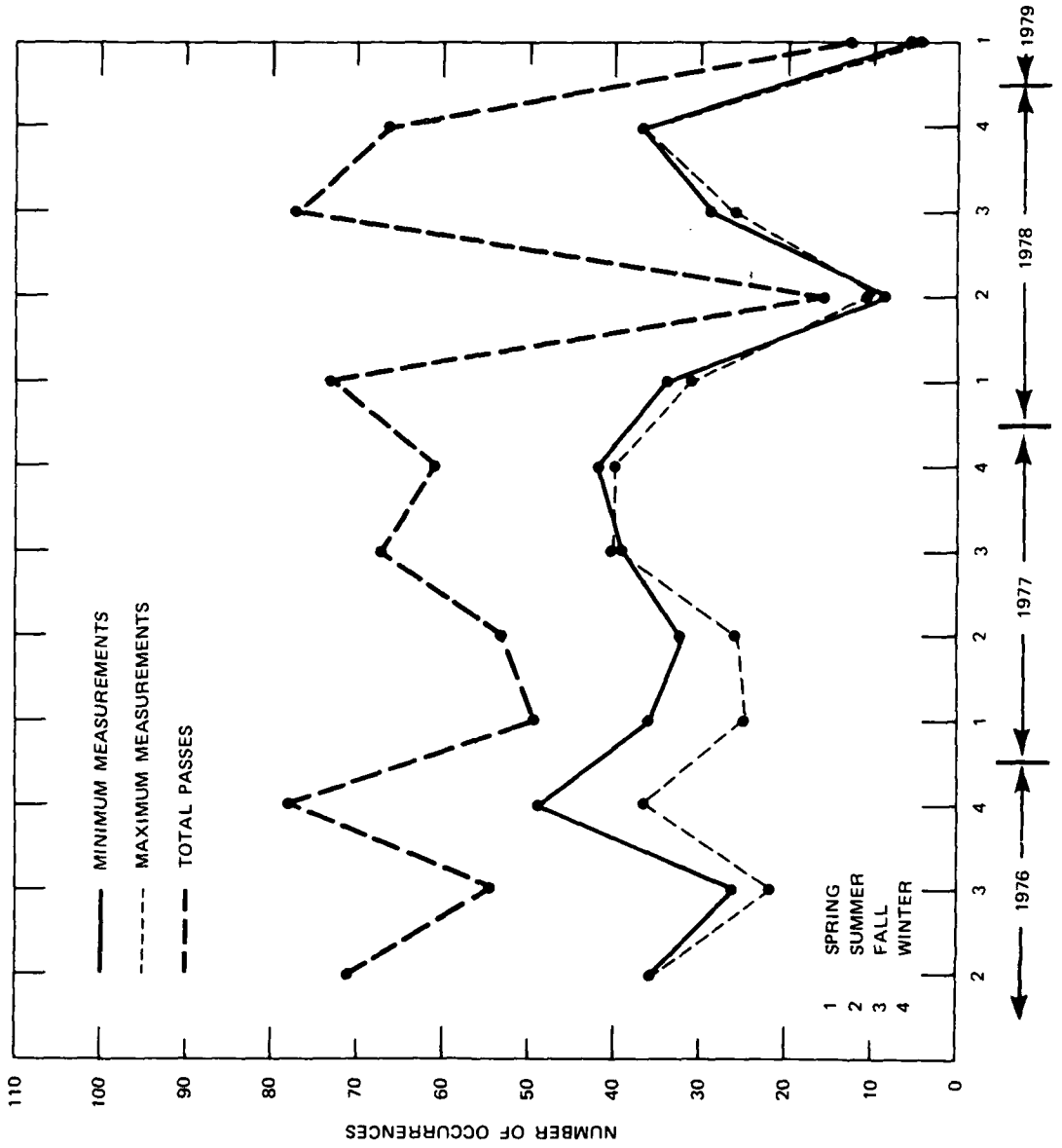

FIGURE 16 ANNUAL AND SEASONAL OCCURRENCE OF TEC BOUNDARY FEATURES

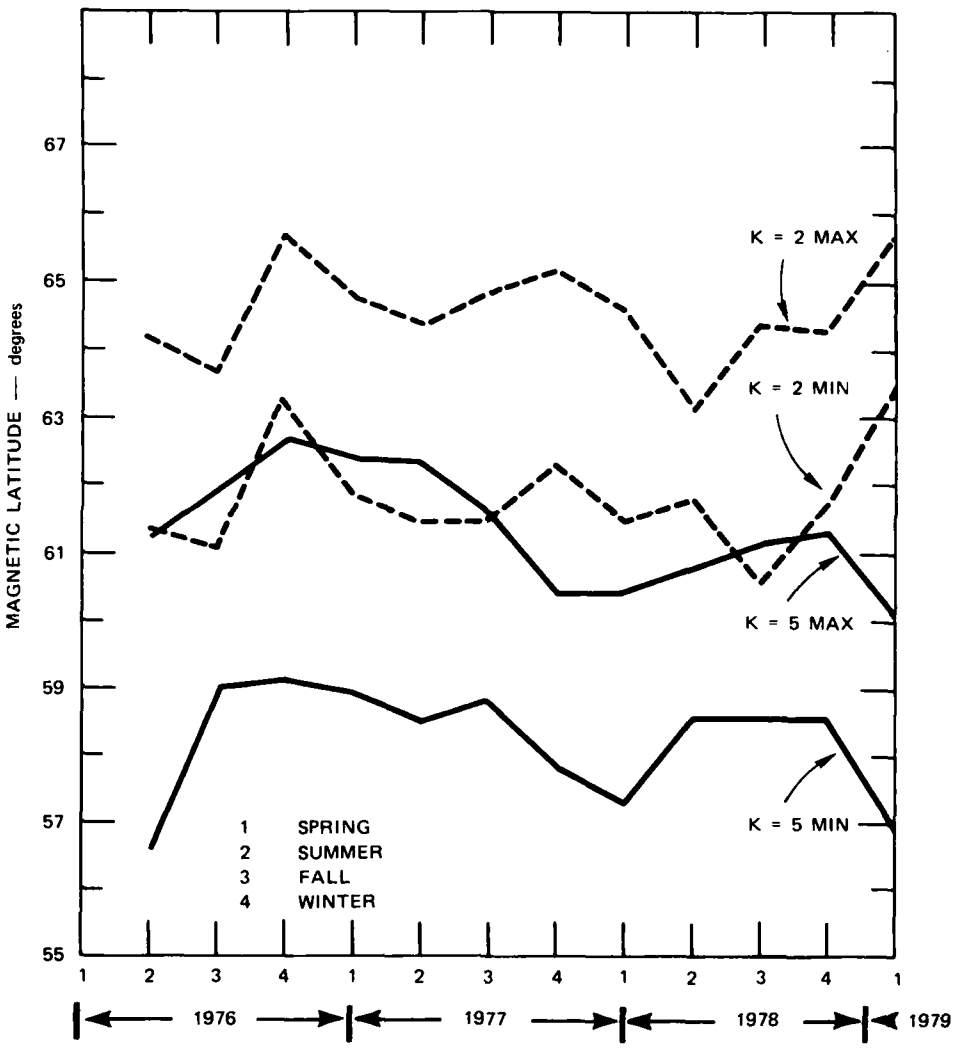

FIGURE 17 TEC BOUNDARY LOCATION FOR PERIODS OF LOW AND MODERATE LOCAL MAGNETIC ACTIVITY

C. Structure of TEC Boundary

To characterize the structure of the TEC boundary, we first measured the TEC gradient. In Figure 18, the results for weakly and moderately disturbed passes are shown. The gradients evidently depend on the season, in that they are generally larger in the summer months than in the winter months; moreover, the TEC gradient generally increases with solar activity, as does the occurrence of detectable TEC gradients.

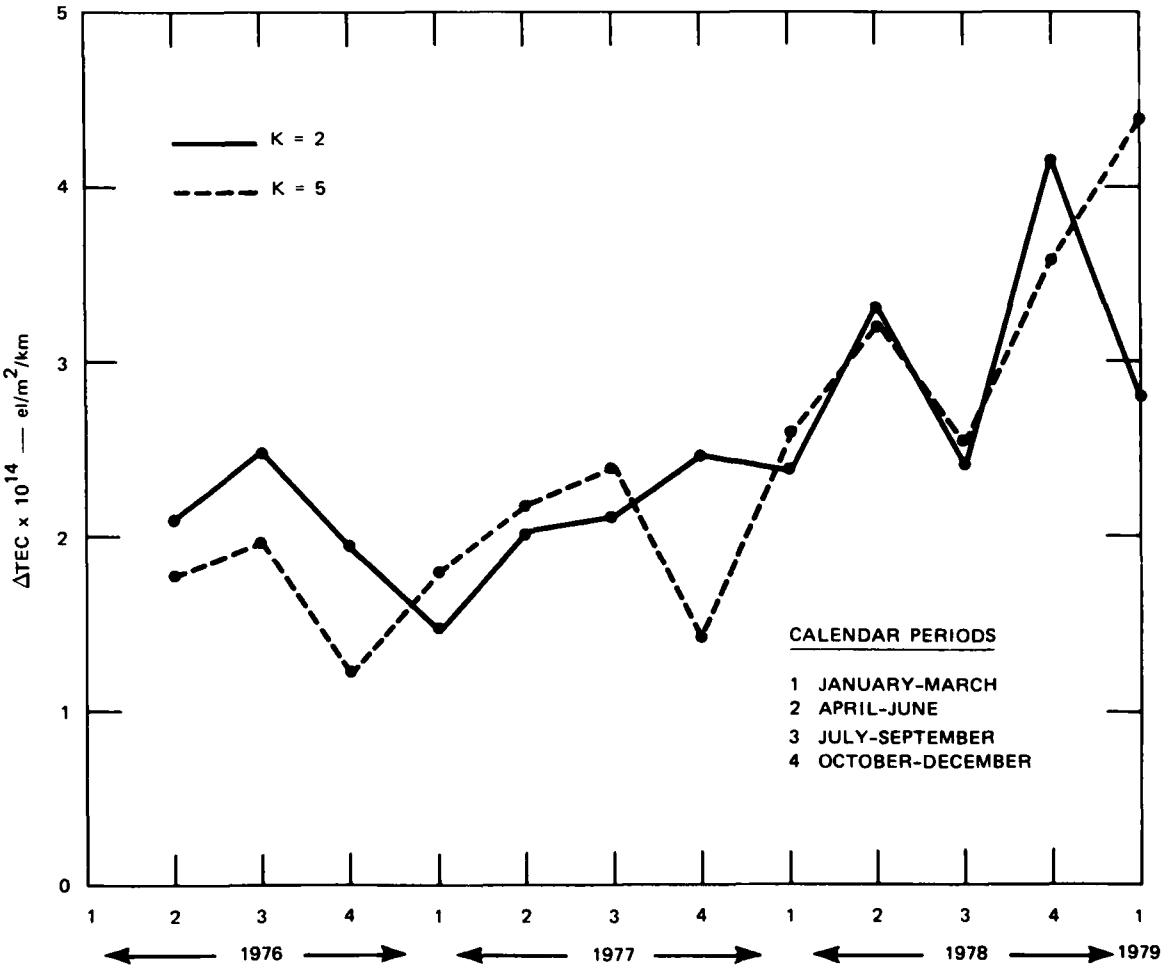

FIGURE 18 TEMPORAL VARIATION OF TEC GRADIENT SHOWING AN INCREASE WITH INCREASING SOLAR-CYCLE ACTIVITY

To explore the seasonal dependence in more detail, a linear least-squares fit to the TEC gradient as a function of the corresponding three-hour college Kindex has been plotted for each six-month period. The results are summarized in Figure 19. The gradient decreases rapidly with increasing K during the fall and winter months, whereas during the summer months, it increases.

We have associated the steep TEC gradients with an enhanced, unstable F layer. To show this directly, we have scatter plots of the average rms phase measured between the TEC gradient boundaries against the measured gradient. In all cases, the rms phase shows a positive correlation. The magnitude of the slope of the linear least-squares fit for each period is summarized in Table 1.

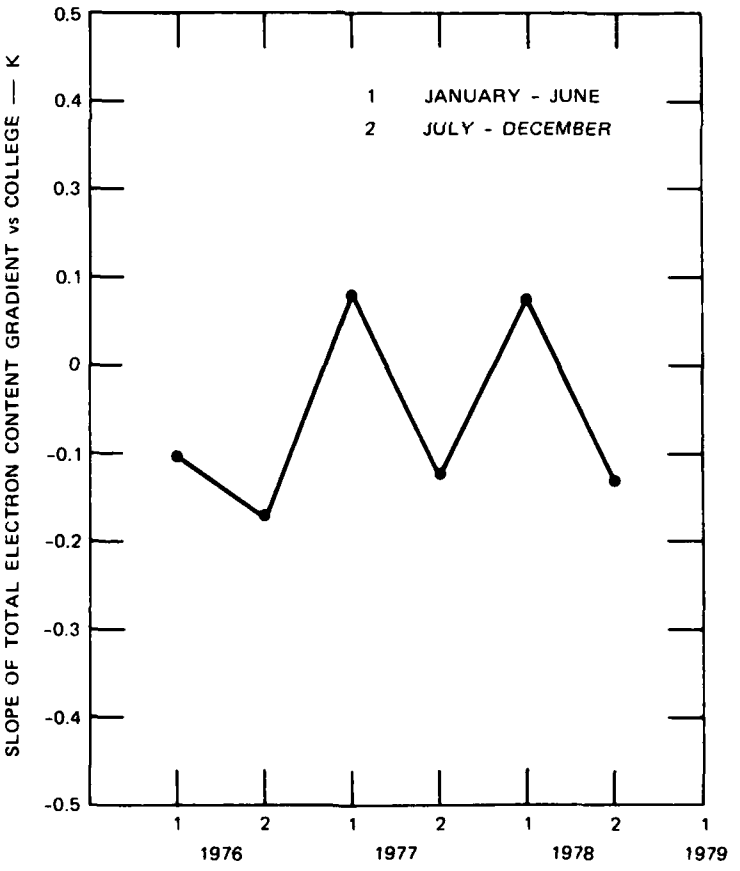

FIGURE 19 SLOPE OF LINEAR LEAST-SQUARES FIT TO TEC GRADIENT vs COLLEGE K INDEX

Table 1

SLOPE OF LINEAR LEAST SQUARES FIT TO rms PHASE
VERSUS TEC GRADIENT BY 6-MONTH CALENDAR PERIOD

Year	Period	Slope
1976	1	0.142
	2	0.108
1977	1	0.111
	2	0.216
1978	1	0.185
		0.154

D. Conclusions

In this section we have reviewed the occurrence and structure of nighttime TEC boundaries as observed by the Wideband satellite from the Poker Flat Station between May 1976 and June 1979. Well-defined TEC boundaries occur in about 50 percent of the passes irrespective of the season or solar-cycle epoch. The steepest gradients have been associated with an enhanced, but unstable F region. The occurrence statistics primarily reflect the incidence of enhanced F-region "blobs" migrating equatorward of 70° magnetic latitude.

The TEC boundary structure strongly depends on magnetic activity and more weakly on the solar-cycle epoch. The TEC gradients tend to be positively correlated with magnetic activity during the summer months, but negatively correlated during the winter months. In all cases the phase-scintillation level measured within the TEC boundary region is positively correlated with the TEC gradient.

V EQUATORIAL TEC

A. Introduction

The Wideband coherent beacon observations provide not only a characterization of ionospheric phase scintillation, but also a measure of the large-scale (> 100 km) variations that are directly related to ionospheric TEC. In this section we consider the TEC measurements made at Kwajalein Atoll and Ancon, Peru, both equatorial stations, between May 1976 and August 1979. We first consider the nature of the TEC measurement, and the difficulties encountered in applying the most obvious methods for interpreting the data. A brief review of equatorial electrodynamics and studies of three aspects of our TEC observations follow: (1) the dramatic sunspot number dependence of the midnight equatorial TEC, (2) the seasonal behavior of the latitudinal distribution of TEC, and (3) the association between TEC and the occurrence of scintillation-producing irregularities.

B. Analysis Method

1. Measurements

Each of the dispersive phase measurements available at nine frequencies from the Wideband system [Fremouw et al., 1978] is directly related to the propagation-path-integrated electron density

$$\varphi = \frac{b}{f} \int_o^s N ds \quad , \tag{11}$$

where b is a constant, f is the measurement frequency, and s indicates the propagation path to the satellite. In practice, the dispersive phase is continuously reconstructed from high sample rate quadrature components, and thus its resolution is limited only by the receiver, i.e., changes in the order of degrees can be observed. However, because of 2π ambiguities,

the reconstruction has an unknown starting value, which for absolute measure of TEC must be established by some other means.

In theory, the UHF comb of seven frequencies on Wideband can also provide the necessary absolute, but lower resolution, measure of TEC. The method uses the second-difference of phases for a number of closely spaced spectral lines [Burns and Fremouw, 1970]

$$\Delta_2\varphi \; b \; \frac{f_m^2}{f^3} \int_o^s N ds \quad , \tag{12}$$

where f_m is the frequency separation in the spectral comb (i.e., 11.4729 MHz for Wideband).

During the data collection portion of the experiment much effort was expended in the application of Eq. (12). This was necessary because as an absolute dispersion measure, $\Delta_2\varphi$ is sensitive not only to ionospheric dispersion, but any dispersion in the spacecraft transmission or ground receiver systems. The methods of prelaunch calibration and post-launch comparisons with other measures of TEC in the auroral zone are detailed in Fremouw et al. [1977]. Similar calibrations were made at Kwajalein using ALTAIR radar Lincoln Lab Sphere tracks, and at all three ground stations using standardized antennas [Cousins, 1979]. The resulting sets of system dispersion constants, estimated for each station, were applied during the processing of each satellite pass to supply a starting value to the continuous reconstruction of high resolution dispersive phase.

During the subsequent compilation of the TEC data, on average, the TEC values seem correct; however, pass-to-pass variations are often much too large to be attributed to ionospheric changes. Following recent detailed reanalysis of both the method and the data, we have concluded that such variations are unavoidable, and that routine calibrations using $\Delta_2\varphi$ are not practical.

The spacecraft antenna is highly frequency-dispersive, because of the limited size of the ground plane and multipath effects. The patterns, taken before launch for later calibration use, are highly structured,

and generally subject to question, since other aspects of the patterns were observed to change after launch. The UHF antenna was least dispersive at low angles, and, accordingly, the application of the $\Delta_2\varphi$ measurement was made early in each pass. A second conflicting problem is introduced, in that, at these low angles, the phase scintillation tends to maximize. The combined effect of these problems, i.e., noisy data and dispersive structure in the spacecraft antenna, contributes errors on the order of tens of degrees in measured $\Delta_2\varphi$. This error is comparable to the ionospheric contribution at the most closely spaced lines. Only in a few cases has it been possible to eliminate obviously noisy data and improve the TEC estimate.

Thus, an absolute calibration of the bulk of the Wideband TEC data is not feasible. Fortunately, this is not a major problem for a morphological study such as this, because the shape of the latitudinal TEC distribution reflects the solar cycle and seasonal dependences. When the term TEC is used to describe our data in the following sections, we are actually referring to changes in TEC, as derived from the dispersive phase alone.

2. Geometrical Corrections

The high inclination of the Wideband satellite orbit provides a "snapshot" of the ionosphere over about 20° of latitude in about 15 min. The propagation geometry, of course, changes significantly from overhead to the horizons, and interpretation of the TEC data in terms of the latitudinal distribution of ionization requires removal of that propagation geometry. The simplest and most widely used approach is to assume a slab of constant ionizat on at a particular height. In that case, the TEC variation can be described simply as $N_T = N_o \sec\theta$, where θ is the zenith angle of the propagation path at the chosen layer altitude, and N_o is the overhead TEC value.

We have found that such a constant altitude slab model is not consistent with the Wideband equatorial data, and can be demonstrated using some of the early Wideband data collected in 1976 at Ancon. During

this low sunspot phase of the solar cycle (SSN $\sim$ 15), the evening F-region vertical drifts are small, and, therefore, the equatorial anomaly in TEC is absent at the time of Wideband observation, which is around local midnight (see Section C, below). During this period, the shape of the uncorrected TEC records are nearly constant (for the same propagation geometry) for weeks at a time. Therefore, application of an appropriate geometry correction scheme should produce similar latitudinal variations in TEC for both high- and low-elevation passes.

The application of the constant height slab for these data is shown in Figure 20 for two heights and several passes with different propagation geometries. These have been grouped into two sets: those with maximum elevation angles of 30° to 60° for which the sec θ factor changes from $\sim$ 4 to $\sim$ 2 from the horizons to closest approach, and those with maximum elevation angle of 60° to 90° for which sec θ changes from $\sim$ four to 1. If the constant height slab model is appropriate, the shapes of these geometry corrected distributions should be the same (although not necessarily flat). This is clearly not the case for a layer between 350 km and 700 km in Figure 20(a) and 20(b); the slab model produces a rapid change in TEC around closest approach, which differs for the two pass geometries.

A model that produces a more consistent geometrical correction, is one for which the F-layer height follows a particular magnetic field line. Tsunoda [1980] has presented incoherent-scatter data from Kwajalein that clearly shows this behavior for the nighttime F layer. In Figure 20(c), we show the same low-high-elevation pass sets from Ancon, now corrected for a field-aligned layer. The height of the layer ranges from about 700 km over the dip equator to about 300 km at 10° dip latitude. The shapes of the low- and high-elevation latitudinal distributions are much more consistent than for the constant height layer in Figure 20(a) or 20(b).

Having established a geometrically consistent model with which to interpret the data, we now consider the latitudinal variation in effective layer thickness that produces the curvature in the Figure 20(c)

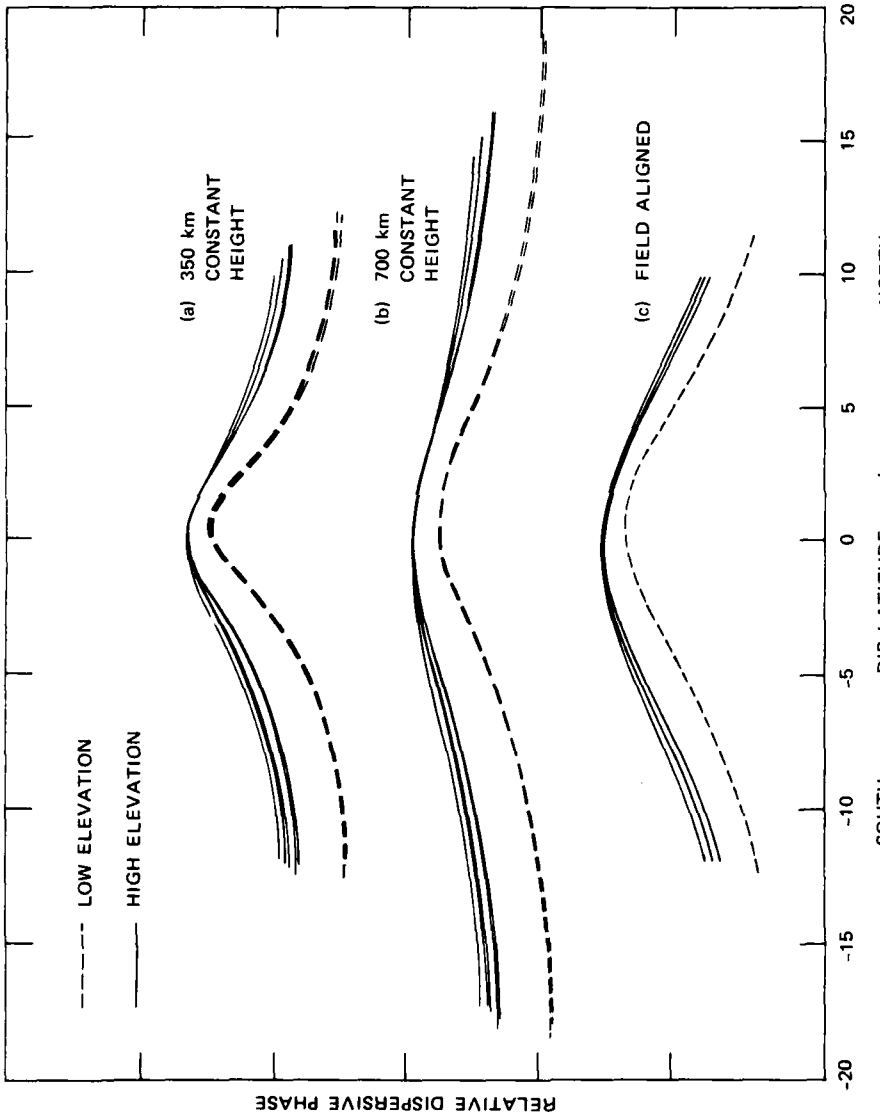

FIGURE 20 COMPARISON OF THE GEOMETRICAL CORRECTION IN TEC FOR HIGH- AND LOW-ELEVATION PASSES FOR A CONSTANT THICKNESS LAYER (a) AT 350 km, (b) AT 700 km, AND (c) LOCAL FIELD ALIGNED

data. From that figure, clearly, the curvature cannot be removed by moving the layer up or down (i.e., by the sec θ dependence on layer altitude). This idea is further supported by the ionosonde data from Kwajalein, which, despite an increase in f_oF2 from 1977 to 1979, showed little long-term change in the height of the F-region peak.

The most direct evidence that the curvature in Figure 20 is due to a change of layer thickness with latitude, however, is that both the Ancon and Kwajalein data show similar patterns during this period of low solar activity. Because only a few days of data from Kwajalein are available during the September-to-October period, we illustrate the similarity between stations using the November-to-December 1976 data. As Figure 21 shows, the ionization distribution has become slightly asymmetrical during this season, because of the equatorial anomaly to the north (see Section C, below). The shapes of the geometrically corrected TEC distributions with latitude are very similar despite the large longitudinal separation of the two stations. We feel that this justifies the use of the Ancon September-to-October distribution as our low sunspot number, no-anomaly baseline for the latitudinal distribution corrections at Ancon and Kwajalein.

Variation in F-layer thickness with latitude is also consistent with the single data set presented in Tsunoda [1980], in which he observed much narrower F-layer thickness with roughly the same peak density south of Kwajalein. (His observations to the north of Kwajalein cannot be compared to our 1976 data because of higher sunspot-number conditions.)

For study of the long-term, large-scale nighttime TEC behavior, then, we postulate the following low sunspot background model: an F layer whose centroid is field aligned, ranging in altitude from 700 km over the dip equator to about 350 km at 10° dip latitude, and an effective thickness at the magnetic equator roughly double that at ±10° dip latitude. In what follows, we consider the long-term deviations from this baseline model because of sunspot number, season, and other causes. Before the data are presented, however, a brief description of the general electrodynamic behavior of the equatorial ionosphere as it is currently understood is worthwhile.

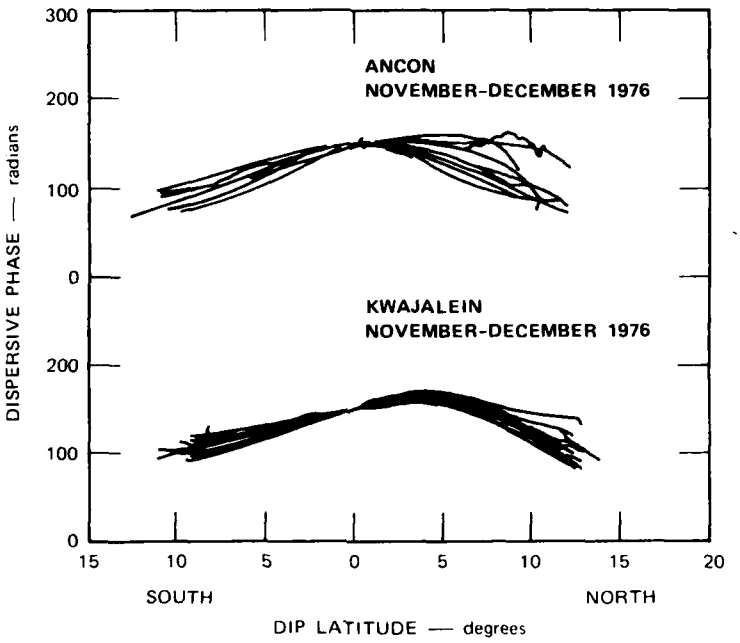

FIGURE 21 GEOMETRICALLY CORRECTED TEC OBSERVATIONS AT (a) ANCON, AND (b) KWAJALEIN FOR NOVEMBER THROUGH DECEMBER 1976 LOW SUNSPOT CONDITIONS

C. Dynamics of the Equatorial F-Region

The behavior of the equatorial F region is dominated by electric fields. Foremost of these is the E-region polarization field created by tidally controlled winds blowing across the geomagnetic field. Fields generated away from the magnetic equator map directly into the F-region along the highly conducting flux tubes. This E-region dynamo drives the F-region ionization continuously upward by E x B forces during the day. From these high altitudes, pressure and gravity force the ionization back down flux tubes to higher and lower latitudes. This rise and subsequent downward diffusion produces a latitudinal variation in density that peaks to the north and south relative to a trough over the equator: the "Appleton anomaly."

Many years of ionosonde measurements have defined the overall dependence of the anomaly on sunspot number, season, and time of day. During

the day, at the equinox and at sunspot minimum, the crests of the anomaly occur at ~17° dip latitude with a critical frequency roughly double that at the equator [Rastogi, 1959]. A similar configuration has been reported by Lyon and Thomas [1963] for the same time and season, but sunspot maximum. The sunspot number has a strong effect on the duration of the anomaly into the evening hours, which are of interest here. Rastogi [1959] shows that for sunspot minimum that the anomaly disappears by 2100 LT. On the other hand, Lyon and Thomas [1963] show that the anomaly becomes more distinct in the premidnight hours during sunspot maximum. At the solstices, north-south asymmetries in f_oF2 typically occur [Lyon and Thomas, 1963] with a reversal of that asymmetry from day to night.

Modeling of these seasonal and diurnal variation of the anomaly as driven by the E-region dynamo have been quite successful. For example, Anderson [1973] solves the time-varying plasma continuity equation including the effects of magnetic field, neutral wind, and E-region dynamo fields. Using that model, he duplicates the experimentally observed spatial and diurnal patterns of the anomaly.

However, certain key features of the evening F-layer behavior cannot be explained by the E-region dynamo alone. The rapid rise of the F-region at sunset, indicating a strongly enhanced eastward electric field, is a case in point. Rishbeth [1971] has explained this behavior, which is referred to as the prereversal enhancement, using an F-region dynamo driven by thermospheric winds. During the day, these fields are shorted by a highly conducting E-region, but near sunset, while high residual F-region ionization remains and strong neutral winds are present, F-region generated fields become significant. Heelis et al. [1974] have modeled this process with good agreement with observation at Jicamarca. Fejer et al. [1979] have compiled a large volume of vertical-drift data from Jicamarca taken over several years. Their evening and nighttime data, which are of interest to this study, are dominated by the enhancement in vertical drift, which depends highly on both sunspot number and season. Furthermore, the time of reversal from upward to downward drifts in the evening shows similar dependences.

In addition to the electric fields produced by F-region zonal winds, the meridional component of the wind has a direct effect on the latitudinal distribution of ionization [Rishbeth, 1977]. The winds flow from high to low pressure regions which have been observed to be highly asymmetrical across the equator [Hedin et al., 1974]. In general the flows are from the summer to the winter hemisphere, although the diurnal and short-term (few days) perturbations to this pattern can be significant.

The effect of the transequatorial wind transfers plasma from the upwind side of the equator to the downwind side, therefore producing significant asymmetries in the equatorial anomaly. Anderson and Matsushita [1974] have estimated the order of magnitude of this variation with season. At times, diurnal variations in neutral pressure tend to produce diverging (day) or converging (night) rather than transequatorial winds. The anomaly under such conditions has been modeled by Rush [1972].

D. Wideband Δ TEC Results

1. Overall Behavior and Sunspot Dependence

In Figure 22, three years of TEC data from Ancon are shown, the 1976 data at the top and 1979 data at the bottom. Each frame corresponds to two months of observations, from which the propagation geometry and the low-sunspot latitudinal distribution of Figure 20c have been removed. Furthermore, because we have no absolute density calibration for each pass, all have been assigned an appropriate constant value of TEC at the magnetic equator, where over the long term, the nighttime overhead TEC should least depend on electrodynamic processes.

Our measurements extend to about ±11° dip latitude, which is well into the region in which the equatorial anomaly crests of f_oF2 normally occur. Because TEC is an integrated measure of the F-layer, it is, in some ways, a more complete indicator of ionization deposition in the anomaly crests than f_oF2 measurements. However, if the thickness of the F-layer under anomaly conditions changes rapidly with latitude [as seen by Vila, 1966, for daylight hours], the TEC distribution with latitude may differ from that implied from f_oF2 studies.

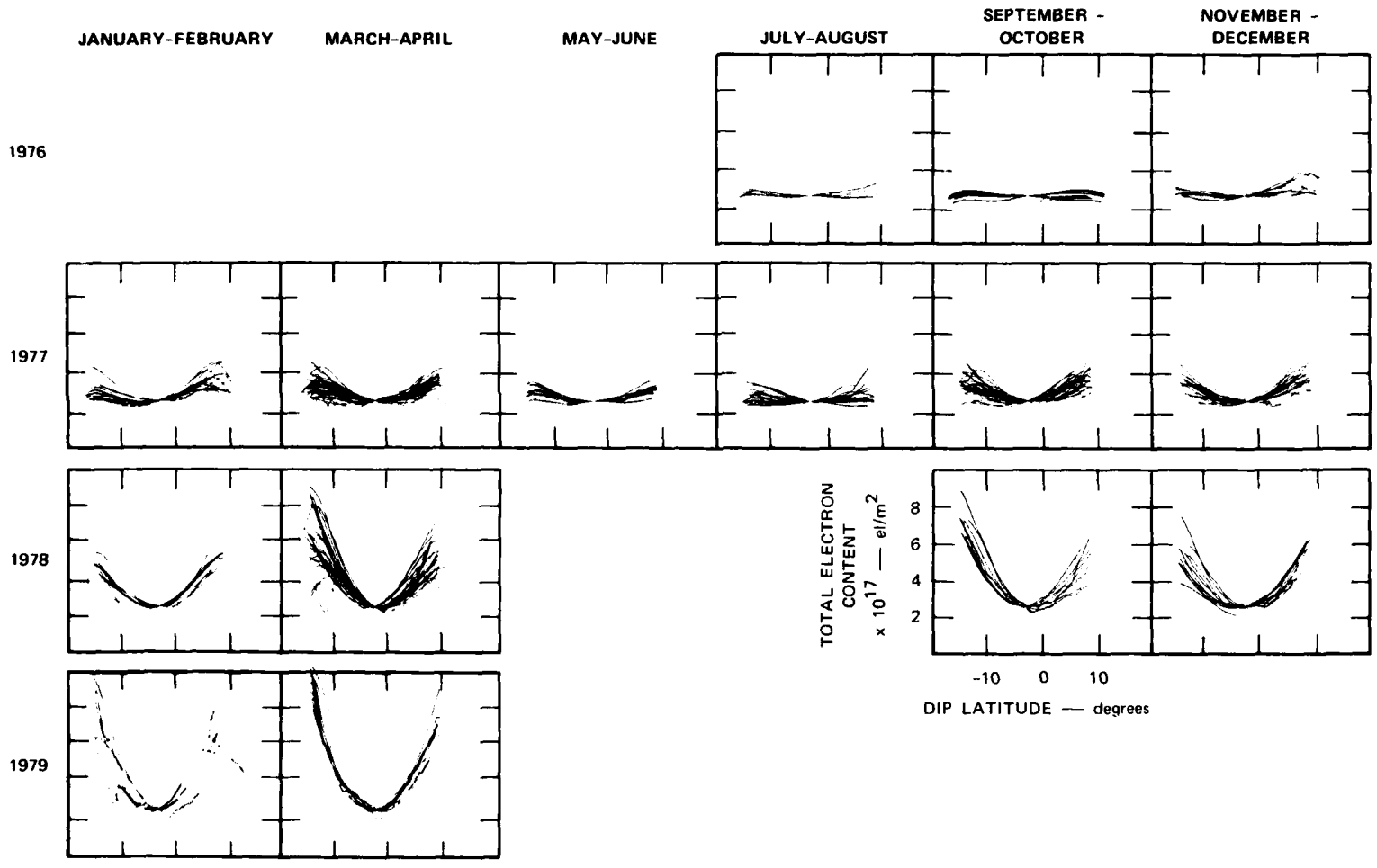

FIGURE 22 LATITUDINAL DISTRIBUTION OF TEC AT ANCON, 1976 THROUGH 1979

As Figure 22 shows, the midnight ionosphere at Ancon changed very little during the low sunspot conditions of July through October 1976. Corresponding to the upswing of the solar cycle from late 1976 through the end of our observations, we see a dramatic increase in TEC magnitudes in the anomaly crest region.

The general shapes of the ionization distributions in Figure 22 show that during the spring equinox, the Ancon observations extend through the southern crest of the anomaly. This is most conspicuous in the 1977 and 1978 data, and, although a similar crest is not clear in the 1979 data, we can make a conservative estimate of the increase of TEC in the anomaly crests with increasing sunspot number. The distributions imply that under equinox conditions the anomaly TEC from 1977 and 1978 changes ~60% and at least another 60% from 1978 to 1979, i.e., more than a doubling in TEC over the first half of the solar cycle upswing.

As the sunspot number increases, so does the magnitude of the TEC in the anomaly crest region, and the overall TEC variability. Much of the variability is caused by systematic solar, seasonal, and diurnal changes in bulk ionization transport. During the scintillation season our data also includes the signatures of specific ionospheric features, i.e., Rayleigh-Taylor bubbles, the occurrence of which also increases with solar activity. The high inclination of the Wideband orbit brings the satellite nearly along the magnetic meridian and if a bubble aligned with a particular flux tube is intercepted, it may remain in the propagation path for several minutes of the entire ~ 15-min north-south scan. The distinct signatures of such bubbles can be seen in some of the early 1978 and 1979 data in Figure 22.

The Ancon data can be directly compared to the vertical drift data collected at the Jicamarca radar [Fejer et al., 1979]. By comparing Figure 22 with those data, we can see that the dramatic change in anomaly TEC with sunspot number is closely associated with the F-region dynamo, or more specifically with the enhanced evening rise of the ionosphere. Fejer et al. [1979] have shown that the magnitude of that rise, which may exceed 30 m/s, depends highly on solar cycle. At sunspot minimum, the

prereversal enhancement is observed only at the equinoxes, and even then is weak. This is consistent with our 1976 data, although we see no evidence of any anomaly even in the Fall 1976 equinox, which probably implies that excess ionization transported by the weak prereversal enhancement had decayed by local midnight.

Fejer et al. [1979] also find that during higher solar activity conditions the prereversal enhancement is strongest in March and September; in 1977 we see an anomaly peak for the same months. The enhancement is weakest from May to August, but does have a longer duration, and continues until $\sim$ 2100 LT, some two hours later than in the winter. We observe much less anomaly from May to August 1977 than in the equinoxes, which implies that primarily, the magnitude of the enhancement, and not its duration, is important to the formation of the nighttime anomaly. This idea is not too surprising because the lower ionosphere densities, from which the anomaly is formed, are still high at E-region sunset, then rapidly decrease.

Turning to the Kwajalein data in Figure 23, we see a somewhat different latitudinal distribution of TEC. Because the observing station at Kwajalein is at $\sim 5°$ dip latitude, we expected to see more of the northern portion of the anomaly. Figure 23 shows that this is, indeed, the case and in fact, the full crest of the TEC anomaly is seen consistently at 12° north dip latitude.

A direct comparison can be made between the Kwajalein and Ancon data for the periods of simultaneous observations. For the low sunspot number conditions of November to December 1976, the TEC distributions at the two stations are very similar, reassuring us that the model layer removal discussed in Section V-B is appropriate. The January-to-February 1977 data are more variable at Ancon than at Kwajalein, but the median TEC distributions for this and the remaining five periods of simultaneous observations match closely. During this period of moderate solar activity then, the large-scale electrodynamics processes producing the anomaly must be the same in the American and Pacific sectors, despite their large longitudinal separation.

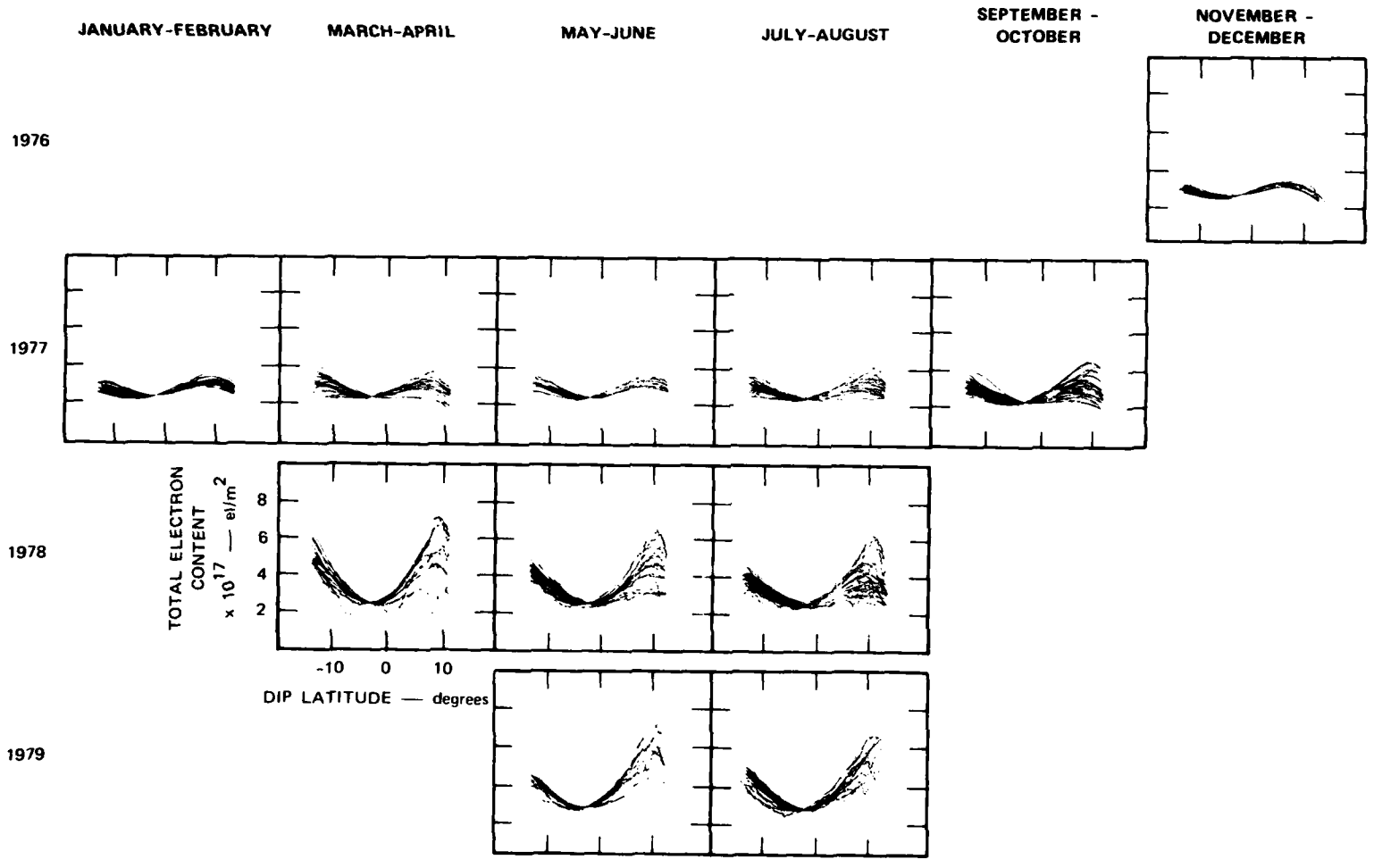

FIGURE 23 LATITUDINAL DISTRIBUTION OF TEC AT KWAJALEIN, 1976 THROUGH 1979

Unlike the Ancon data, which spans September through April and is concentrated near the equinoxes, the Kwajalein observations were made primarily during May through August. These are the months during which the prereversal enhancement in vertical drift is minimum. As we did at Ancon, we see direct evidence of that seasonal change in the Kwajalein data. Between May and August of both 1977 and 1978, we observe a constant TEC value at the summertime northern anomaly crest (and actually a decrease in 1978), when compared to the equinox value. This seasonal variation is further verification of F-region dynamo control. The relatively constant magnitude of TEC in the northern anomaly crest between the summers of 1978 and 1979, despite a doubling of the sunspot number, is less easy to explain. This compares with the equinox TEC increase of > 60 percent between the same years as observed at Ancon. Unfortunately, we do not have enough equinox data from Kwajalein to guarantee that this is not a longitudinal effect, although no evidence exists in the 1977 and 1978 equinox data that shows such a difference. More likely, the strengthening of the F-region dynamo with solar activity saturates at moderate sunspot numbers between May and August. No such saturation can be implied from the Ancon data for the November-through-February solstice period.

We next consider the seasonal changes of the TEC distributions in more detail.

2. Seasonal Dependence

In Figures 22 and 23, the envelopes of the TEC distributions indicate a large degree of variability within each two-month period. Some of the variability is caused by the intersection with discrete, medium-scale structures (i.e., bubbles) as noted above. Much of it, however, is caused by systematic trends with periods ranging from a few days to a few weeks. In this section, we consider the data in terms of those trends, and speculate on their cause.

Starting again with the Ancon data, Figure 24 shows contours of constant TEC versus latitude and day number for the first half of 1977, 1978, and 1979. Each contour level has been assigned a TEC value based

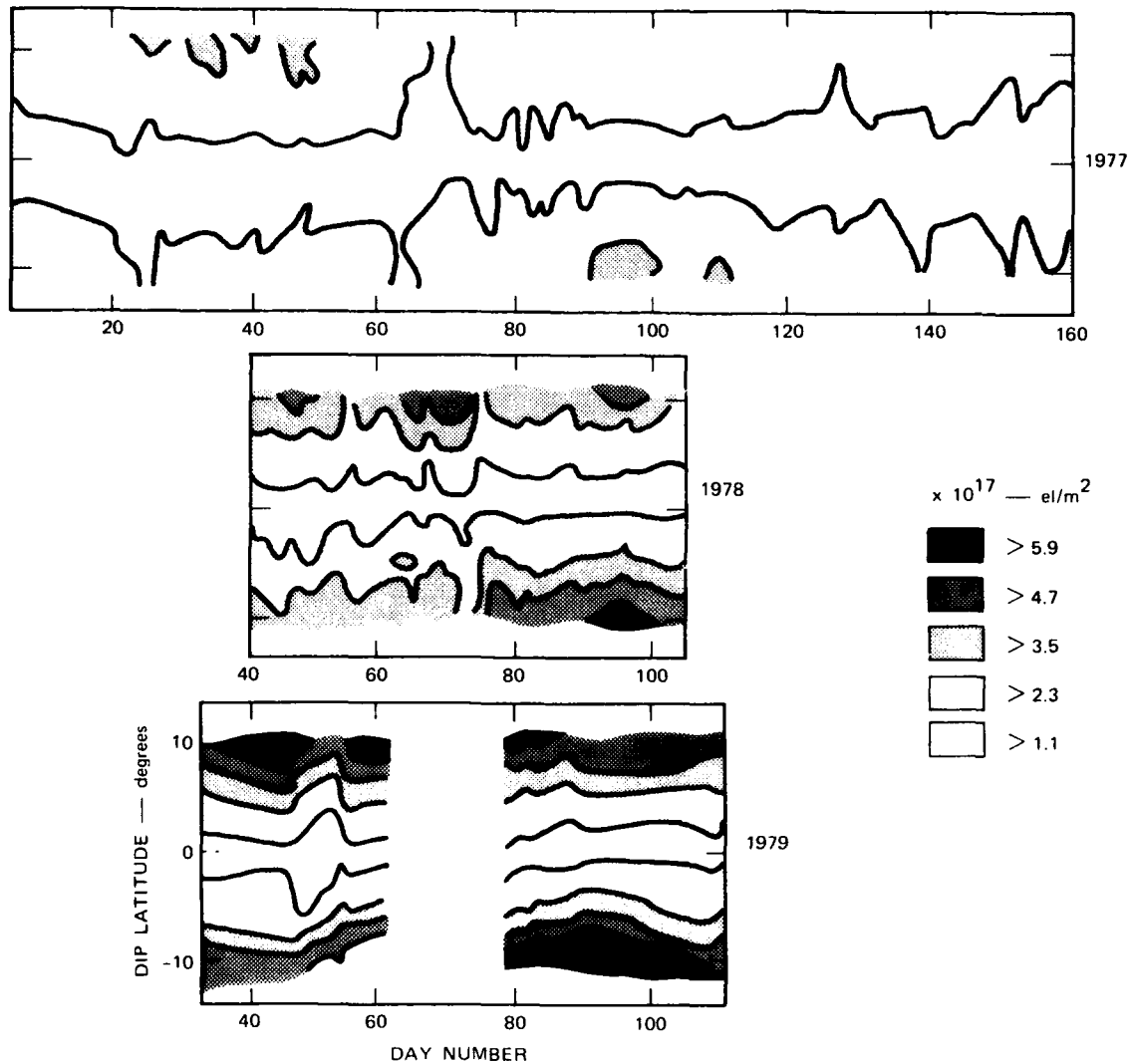

FIGURE 24 TEC VARIATION WITH LATITUDE AND SEASON AT ANCON, JANUARY THROUGH JUNE, 1977 THROUGH 1979

on a typical overhead value of 2.2×10^{17} el/m^2 (150 rad dispersive phase at 1239 MHz). Some weeks include more passes than others, which, of course, contributes to the structure in the contours. We are concerned here with the overall behavior; in the next section, when we compare the TEC and scintillation occurrence, more detail will be considered.

In Figure 24, the increase in TEC with increasing sunspot activity is clear, as in Figure 22. For the 1977 data, the weakening of the anomaly in May and June is also conspicuous despite the continuous increase in sunspot number during this period. However, Figure 24 additionally shows a distinct and systematic northward shift in the anomaly between mid-March and mid-April for all three years. In 1977, the anomaly was to the north and was strongest near Day 40; in 1978, the occurrence peak is more diffuse, showing subpeaks at about Days 50 and 70; in 1979, the northern anomaly peaks at about Day 50. For all three years, the distribution pattern shifts, and the northern anomaly disappears and is replaced by the southern peak on about Day 94.

In Figure 25, the second half of 1976, 1977, and 1978 are shown. For the latter two years, the indication is that the northward shift at the spring equinox is reversed in the fall. Unlike the spring data, however, the time of the fall southward shift appears to vary. In 1976, no real anomaly appears to the south, but appears weakly to the north centered on Day 330. In 1977, the anomaly, which appears to the south on about Day 280, shifts to the north by Day 310. In 1979, a strong southern anomaly, also centered on Day 280, is replaced by a weaker anomaly to the north some 20 to 30 days later.

Unfortunately, except for the low sunspot conditions of 1976 and 1977, little can be learned from this data set about the spatial/seasonal behavior between late December and February. All that can be implied is that the anomaly weakens, as the Jicamarca vertical drift data predict.

To compare the seasonal behavior of the Ancon and Kwajalein data, the simultaneous observation times during 1977 are plotted in Figures 26 and 27, for January through June and July through December,

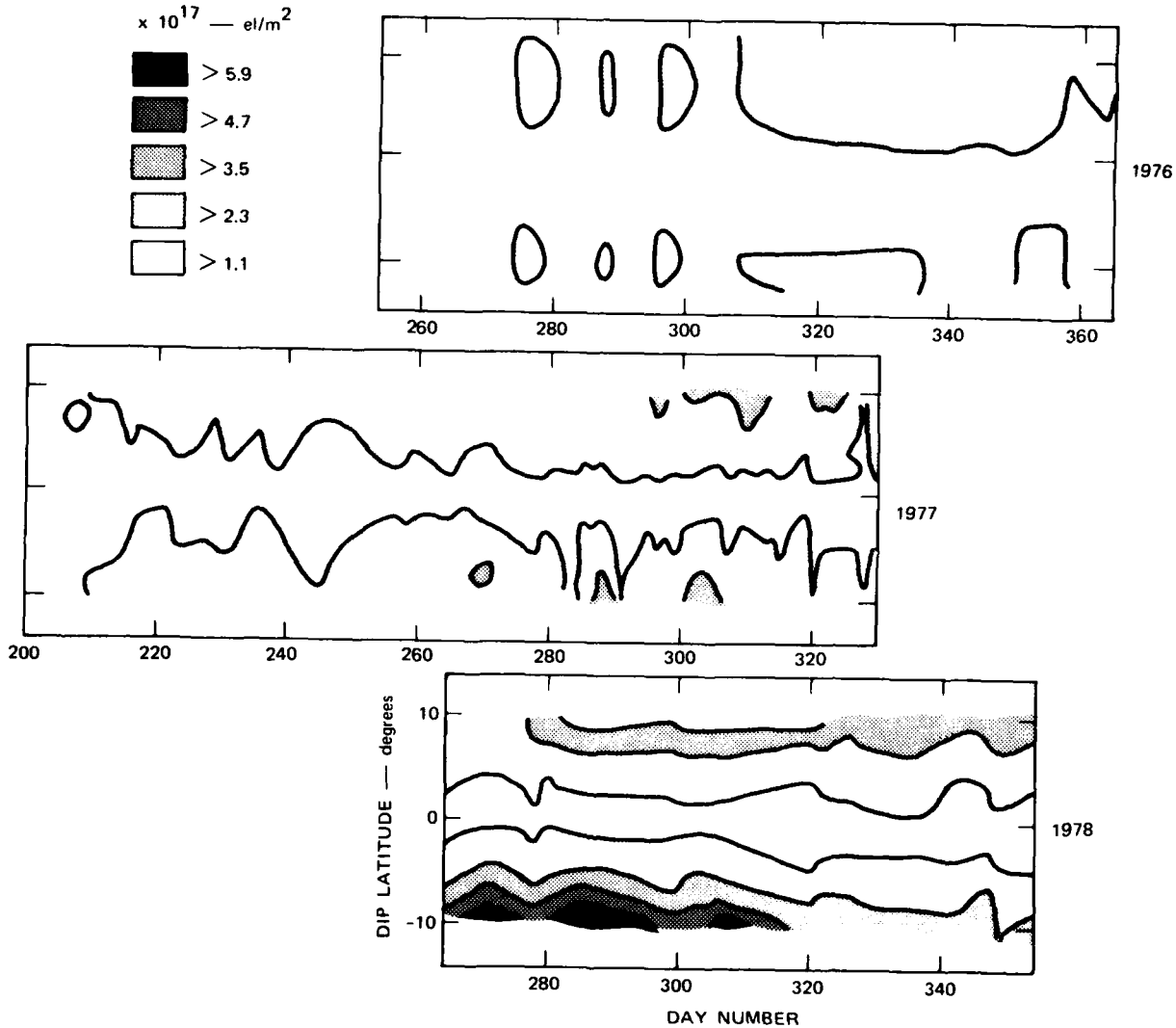

FIGURE 25 TEC VARIATION WITH LATITUDE AND SEASON AT ANCON, JULY THROUGH DECEMBER, 1976 THROUGH 1978

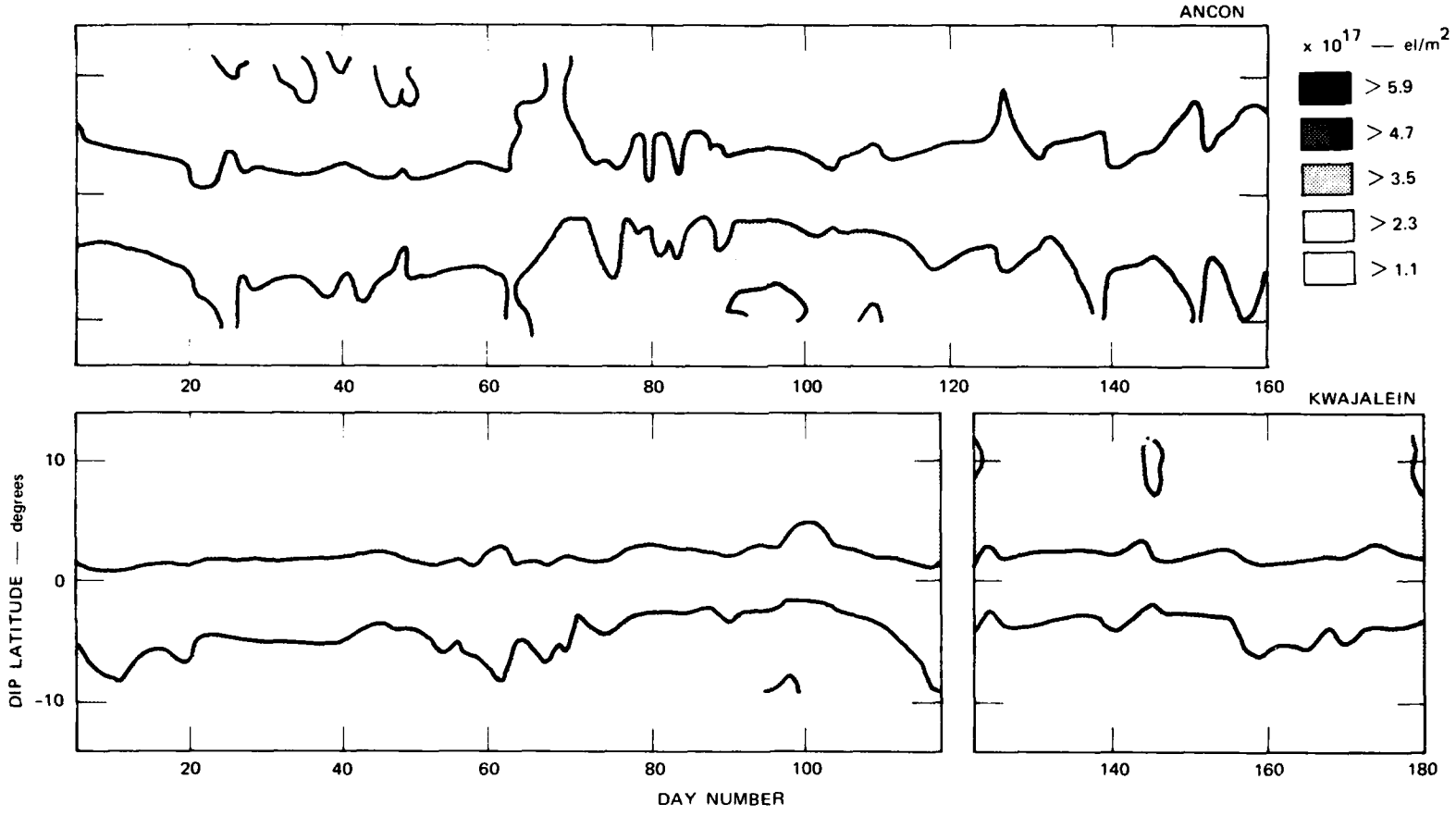

FIGURE 26 COMPARISON OF TEC VARIATION WITH LATITUDE AND SEASON AT ANCON AND KWAJALEIN, JANUARY THROUGH JUNE 1977

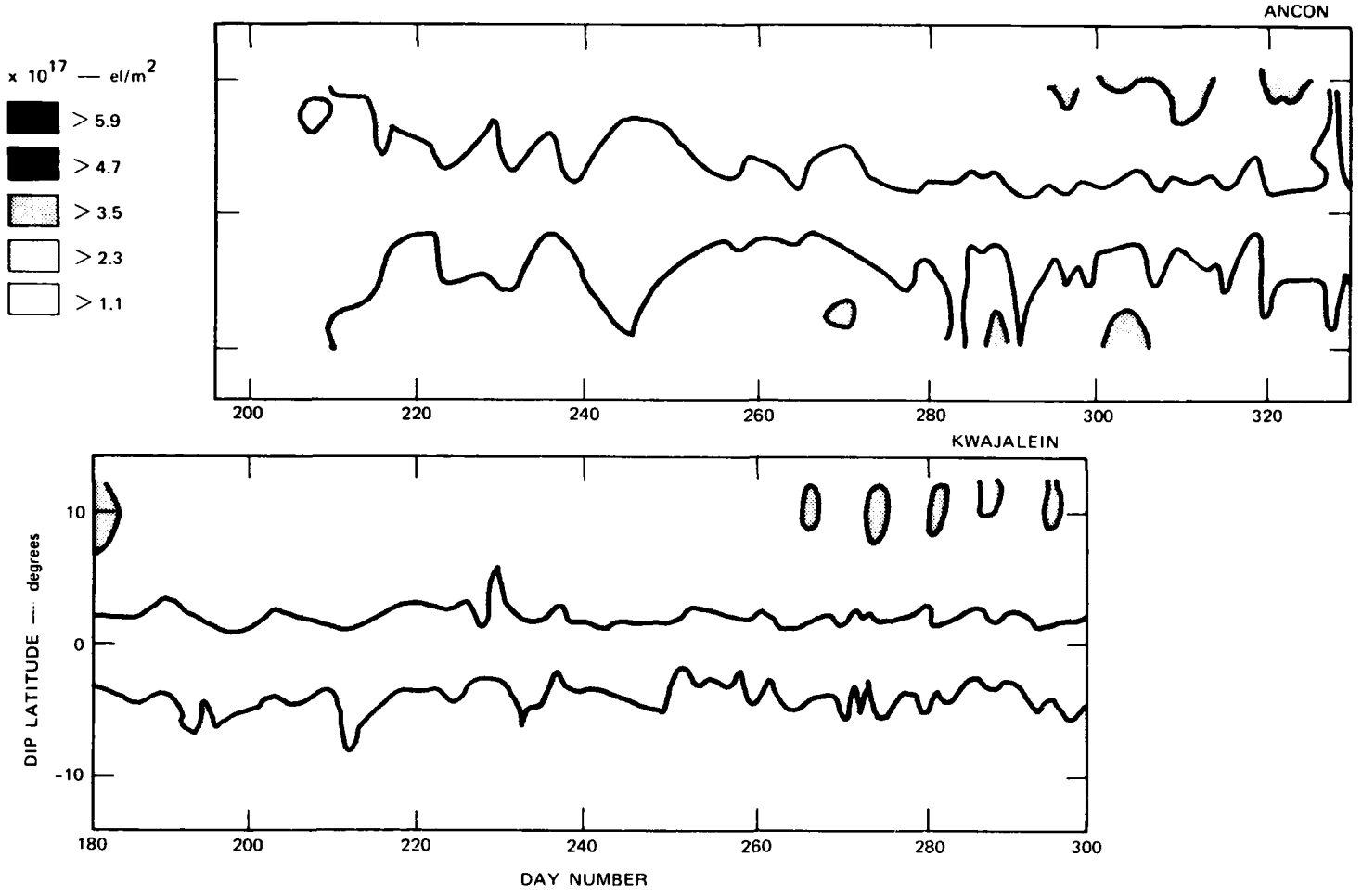

FIGURE 27 COMPARISON OF TEC VARIATION WITH LATITUDE AND SEASON AT ANCON AND KWAJALEIN, JULY THROUGH DECEMBER 1977

respectively. As can be seen, the anomaly shifts at the equinoxes are not as clear in the Kwajalein data, although the trends are the same as at Ancon; in the spring, the TEC distribution generally shifts northward by about 2°, very much like that shown by the distribution at Ancon. The southern anomaly appears at both stations on or about Day 100. In the fall, the southward shift is subtle, but as might be expected, the northern anomaly appears sooner at Kwajalein than at Ancon.

Similar behavior of the equinox anomaly can be seen in the spring 1978 data, which are compared in Figure 28. At Ancon, the southern anomaly shifts southward after a peak near Day 96; a similar shift southward can be seen in the Kwajalein data. During the shift, the northern crest, of which there is some evidence at Ancon, also progresses southward.

The biggest difference between the simultaneous Kwajalein and Ancon data sets is the behavior during the May-through-August period. In Figures 22 and 23 the TEC distributions generally agreed for this period. From Figures 26 and 27, we see now that a match occurs only because the Ancon measurements are concentrated before Day 150 and after Day 220, periods when the contours roughly match. Although the total disappearance of the anomaly between Days 200 and 210 at Ancon cannot be confirmed, the evidence is sufficient, in particular the anomaly enhancements at Kwajalein near Days 120, 145, and 182, that the anomaly behavior at the two stations is different. This suggests that a longitudinal difference exists in the processes creating the anomaly under summer solstice conditions at Kwajalein. Unfortunately, no other coincident observations between Kwajalein and Ancon at this season verify or refute this difference. Figure 26 shows no evidence that a similar difference exists during the winter solstice at Kwajalein in early 1977.

From the accumulated Kwajalein data the northern hemisphere summer patterns in TEC can be established and may shed some light on the Kwajalein-Ancon differences noted above. The contours are shown in Figure 29 for 1977, 1978, and 1979. The TEC magnitudes generally increased with sunspot numbers from 1977 to 1978, and additionally, but

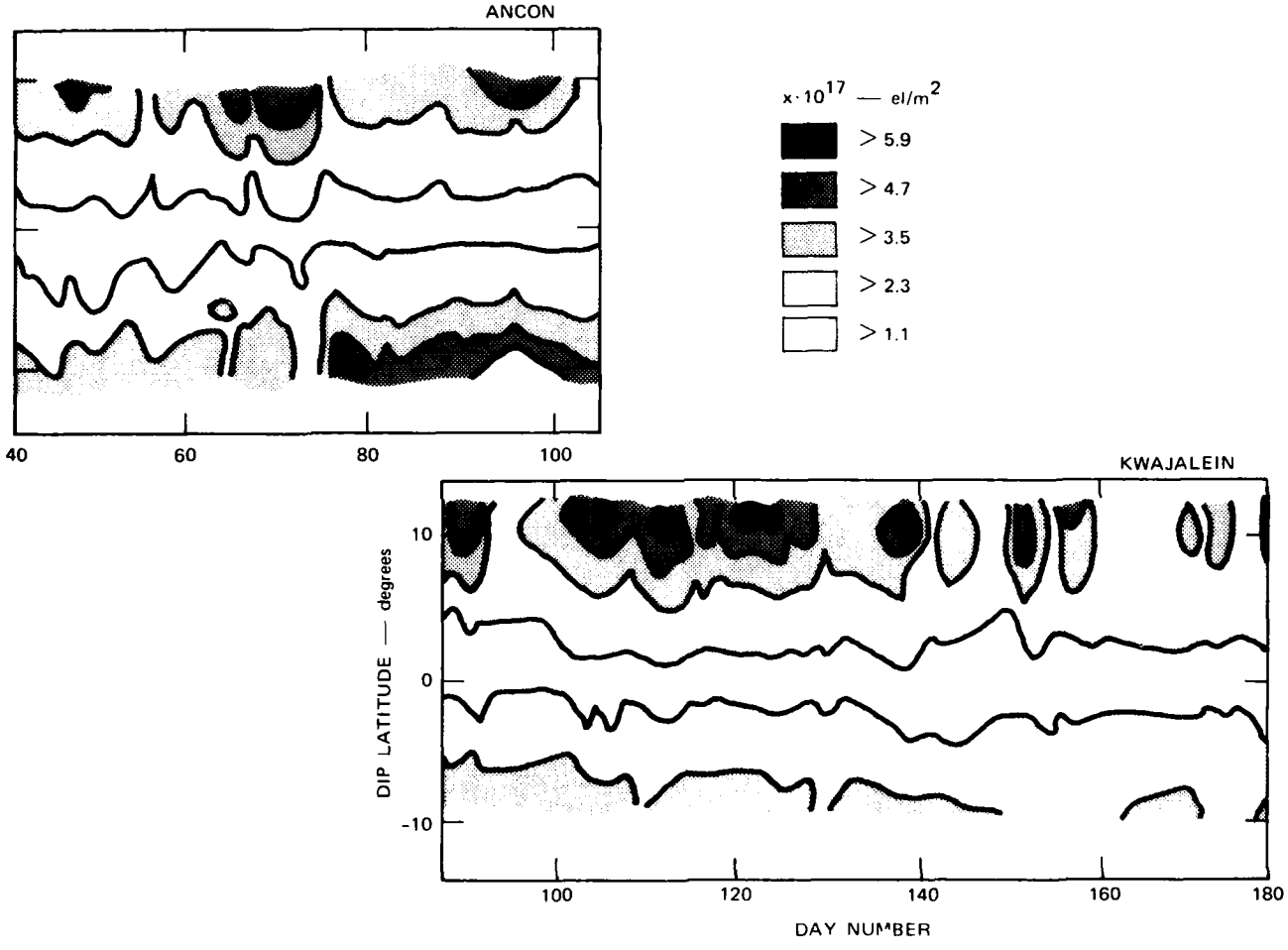

FIGURE 28 COMPARISON OF TEC VARIATION WITH LATITUDE AND SEASON AT ANCON AND KWAJALEIN, JANUARY THROUGH JUNE 1978

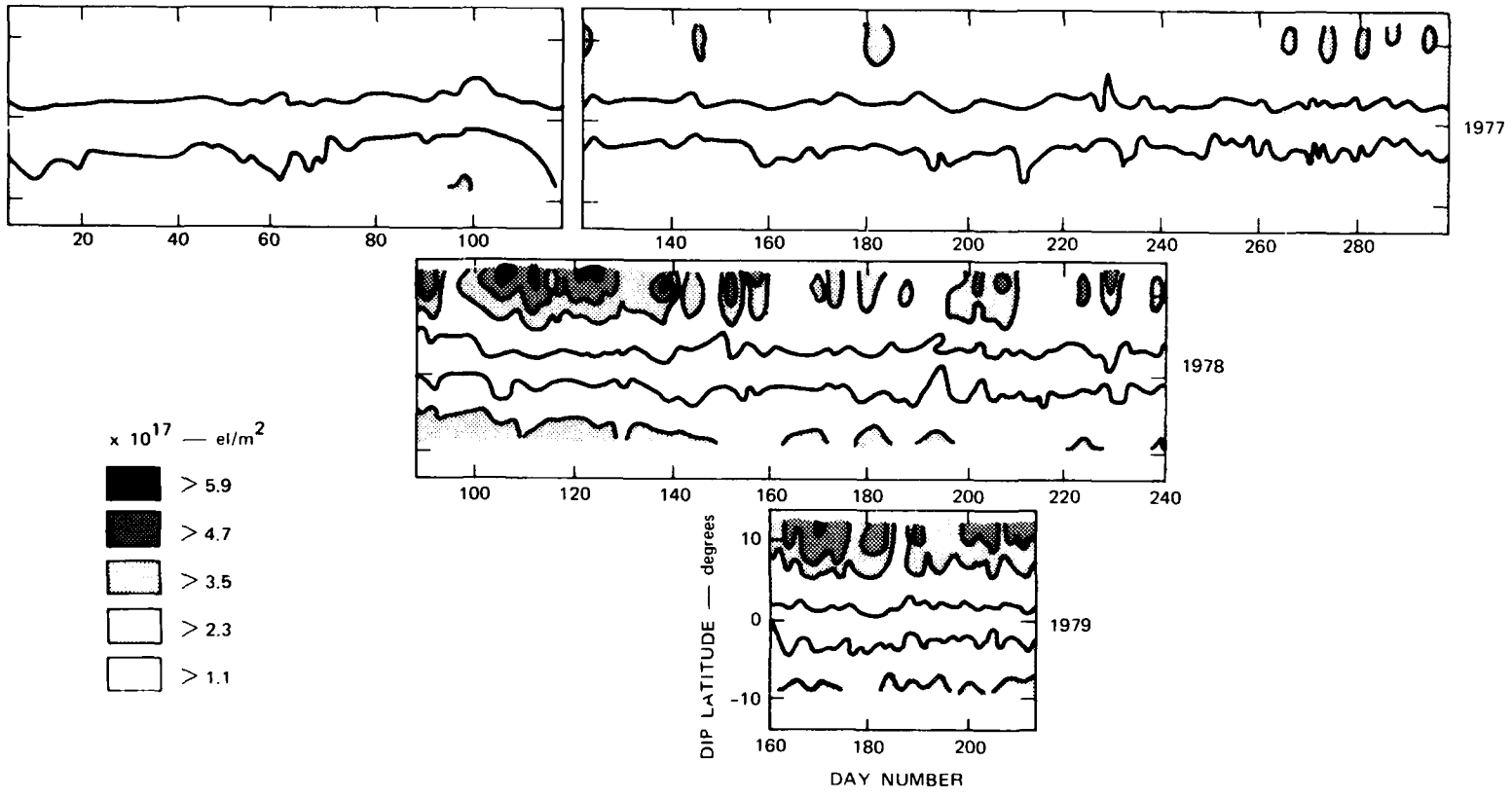

FIGURE 29 TEC VARIATION WITH LATITUDE AND SEASON AT KWAJALEIN, MAY THROUGH SEPTEMBER, 1977 THROUGH 1979

with a lesser degree, increased from 1978 to 1979, consistent with Figure 23. No patterns are obvious in the anomaly behavior during June and July, with major rearrangements occurring over a period of several days. Correlation of particular features from year to year, such as that at Day 180 are most likely coincidental.

The year-to-year variability of the summer data and the differences between Ancon and Kwajalein during this season both point to local control of the anomaly pattern.

E. The Association Between TEC and Scintillation

Although much has been learned about the equatorial ionosphere over the past few years, one question which remains is the seasonal/longitudinal control of scintillation. Livingston [1980] has shown that the scintillation seasons in the American and Pacific sectors are roughly eight months long and six months out of phase. Figure 30 illustrates this for the 1976-to-1977 intensity scintillation data. The season centers on January in the American (and African) sectors and July in the Pacific. Geographic control, alone can be discarded as a cause because of the simultaneous scintillation seasons in the American and African sectors. A combination of geographic-geomagnetic control is most likely the controlling factor, perhaps through the E-region dependent process modelled by Zalesak et al. [1981].

The basic tie between scintillation and TEC is that the scintillation depends on the density perturbation, δn, in the hundreds-of-meters to a few kilometers scale regime; the higher the background density, the larger δn can become. With this in mind, we have compared the scintillation levels with the TEC observed simultaneously by Wideband.

The severity in scintillation generally increases at both stations between 1976 and 1977. This increase can be attributed directly to the solar-cycle-produced increase in background electron density, but is more likely caused by a combination of effects, e.g., higher density plus enhanced instability growth rate from F-layer dynamics. Any direct tie in our data between enhanced TEC and scintillation will be useful in clarifying the specific cause.

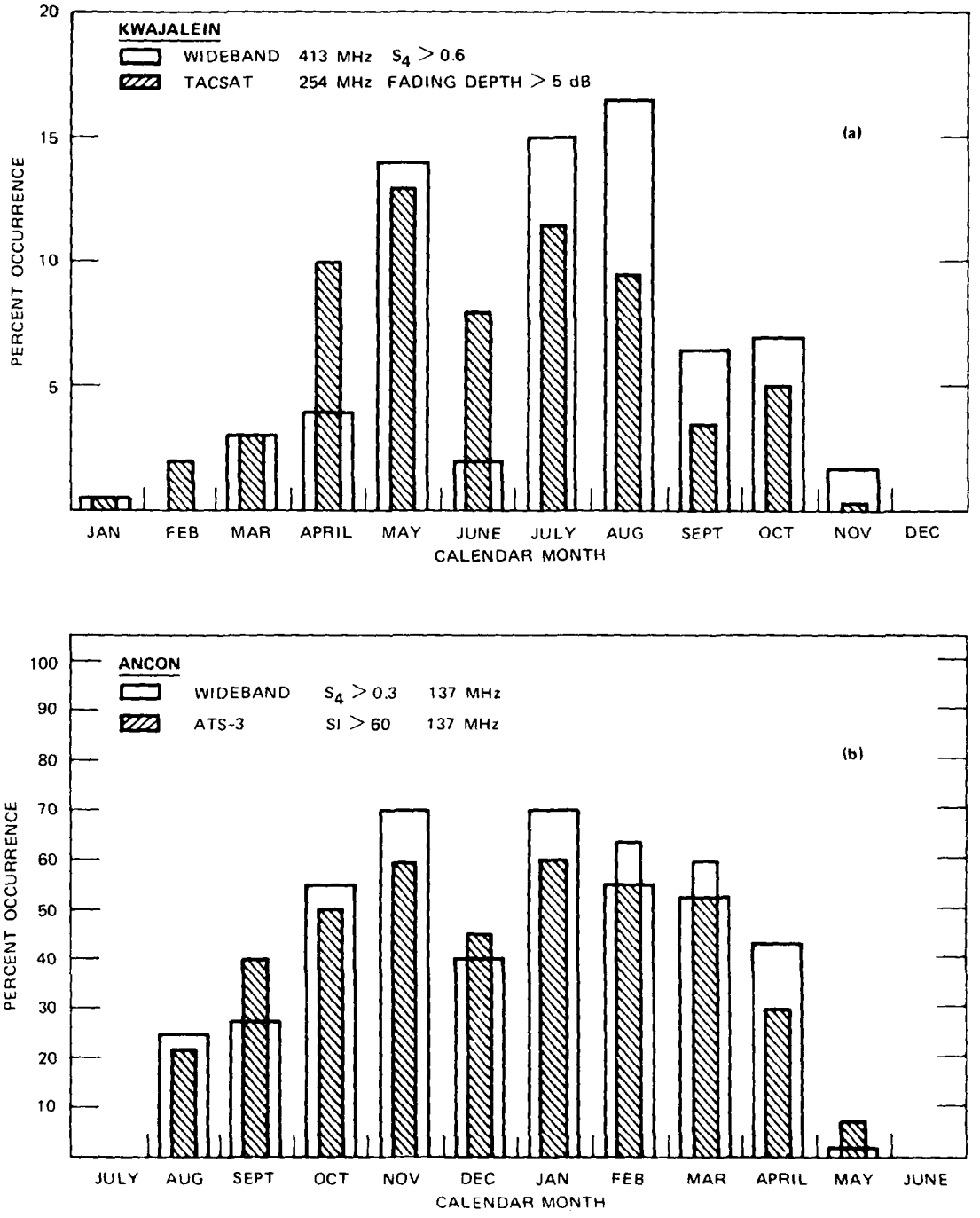

FIGURE 30 WIDEBAND DATA FROM 1977 SHOWING SEASONAL INTENSITY SCINTILLATION OCCURRENCE AT (a) KWAJALEIN AND (b) ANCON

Detailed TEC-scintillation comparisons have been made for campaign times at both stations, during which the observations were more or less continuous. To characterize the scintillation, we have chosen the standard deviation of the phase scintillation at 413 MHz, which, in this case, defines the integrated phase spectral energy on scales shorter than $\sim$ 30 km. Like the TEC, the standard deviation of phase depends on the effective thickness of the ionospheric layer and, thus, must be corrected for geometry. We have done this using the same layer height as used in the TEC corrections.

The spring equinox Ancon data from 1977 are shown in Figure 31a; in Figure 31b, the corresponding phase-scintillation data are displayed, where the size of the circle indicates the magnitude of each 20-s index. Values less than 0.2 rad of rms phase are indicated by the smallest circles that can be seen. A one-to-one comparison between the TEC magnitudes and the scintillation cannot always be expected. For those passes that intercept a depleted flux tube, an edge of which may be structured, the opposite can be true. Thus, we should look for trends of several days in the occurrence of spatial scintillation to match the same trends in TEC.

In Figure 31, there is clearly no evidence of a consistent correspondence between high TEC and the spatial/seasonal scintillation occurrence. The anomaly crests early to the north, and later to the south are not associated with the bulk of the scintillation, which occurs approximately between Days 75 and 95. The scintillation occurs primarily to the south. It may be significant that this three weeks of peak scintillation is at the end of the northward shift period noted in Section V-B.

Interestingly, the same pattern occurs in the 1978 spring data, shown in Figure 32. Here again, association between TEC and scintillation is not clear. In fact, during the span from Day 80 to Day 100, when the anomaly is strongly southward, the scintillation is conspicuously absent. Instead, as in Figure 31, the enhanced scintillation is again primarily southward, and occurs during the northward transition of the anomaly.

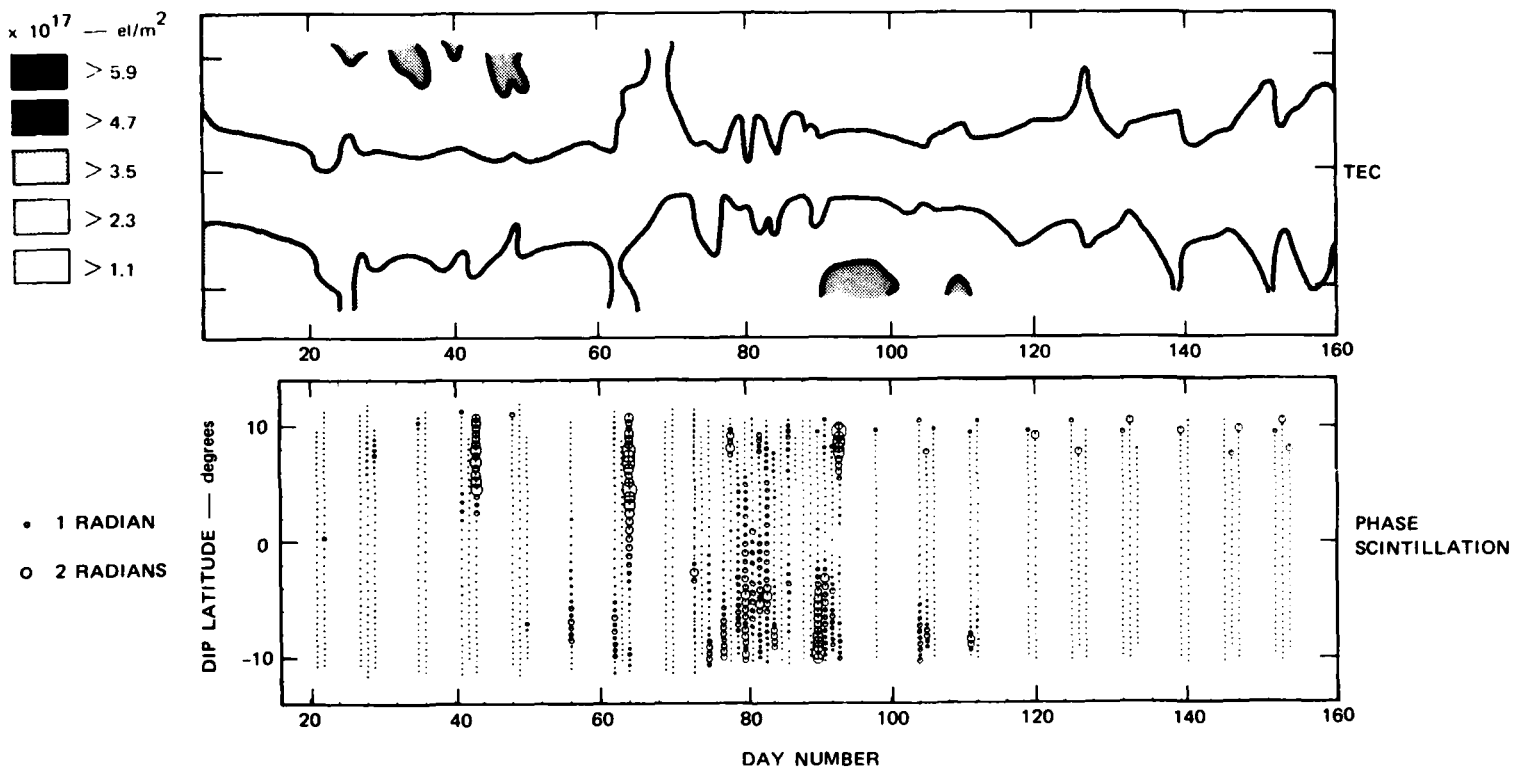

FIGURE 31 COMPARISON OF (a) TEC AND (b) UHF PHASE SCINTILLATION WITH LATITUDE AND TIME, ANCON, SPRING 1977

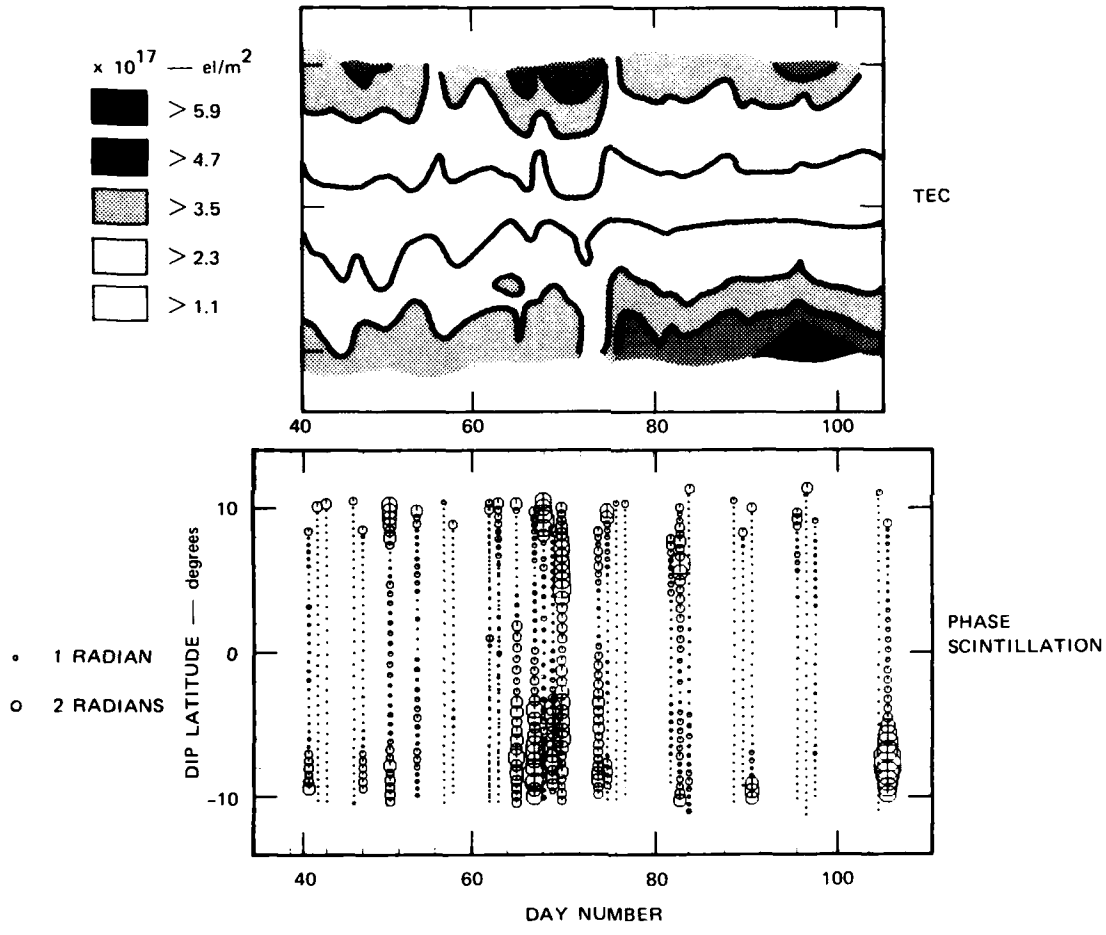

FIGURE 32 COMPARISON OF (a) TEC AND (b) UHF PHASE SCINTILLATION WITH LATITUDE AND TIME, ANCON, SPRING 1978

We have also considered the fall period in 1977, when, as in the spring, the Wideband observations were concentrated. These data are shown in Figure 33. As noted in Section V-B, the fall southward shift in the anomaly occurs between Days 280 and 320. And, as Figure 33 shows, the scintillation occurrence peaks during this period, rather than being associated with times and regions of enhanced TEC. These consistent associations between scintillation and the anomaly shift strongly suggests the influence of the neutral wind.

The Kwajalein TEC-scintillation data for 1978 are shown in Figure 34. First note the general seasonal trend in average scintillation. The severity of the peak scintillation in April is comparable to that in July. The average scintillation in April is lower, however, because of the number of interspersed quiet passes. The overall latitudinal distribution of scintillation is different from Ancon in that the disturbed regions lie to the north, i.e., in the vicinity of the anomaly.

In general, the Kwajalein data show a closer association between enhanced TEC and scintillation than do the Ancon data. This is particularly true during the period after Day 202 and beyond. The exceptions are notable, however, during the appearance of the strongest anomaly between Day 100 and Day 140, and the moderate anomaly crests between Day 170 and Day 190.

Figure 35 shows a more disturbed, but shorter span for the 1979 Kwajalein data. The patterns for the 1978 and 1979 scintillation are not consistent; the period of strongest average scintillation is earlier in 1979, between Day 175 and Day 185. The correlation between scintillation and TEC in 1979 is about the same as in 1978. Both Kwajalein data sets indicate that enhanced TEC regions are necessary for, but do not guarantee, the existence of scintillation producing irregularities.

Significant difference exists, then, between Ancon and Kwajalein in terms of the association between TEC and scintillation. It is not too surprising, in light of the six-month shift in scintillation season between the American and Pacific sectors, that different mechanisms may control the generation of scintillation irregularities.

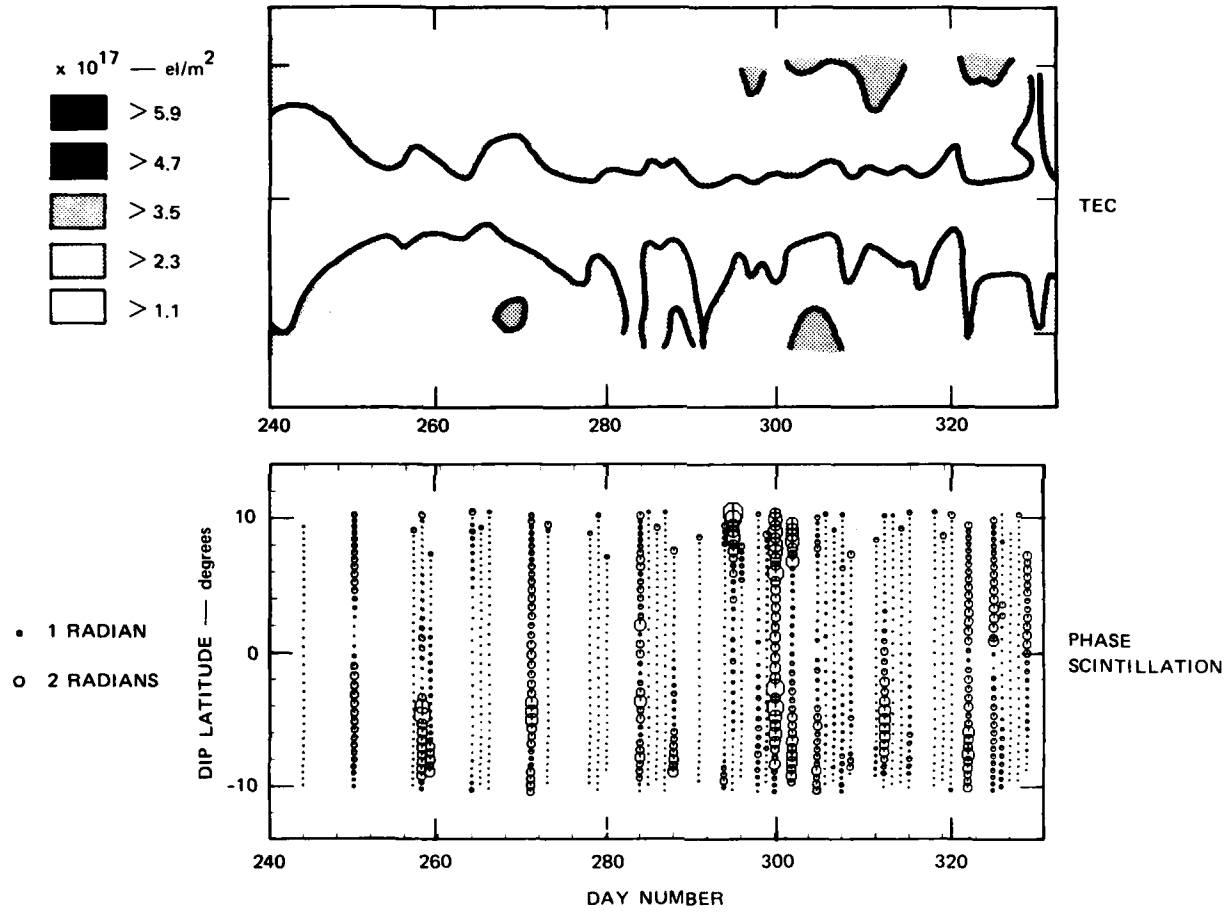

FIGURE 33 COMPARISON OF (a) TEC AND (b) UHF PHASE SCINTILLATION WITH LATITUDE AND TIME, ANCON, AUTUMN 1977

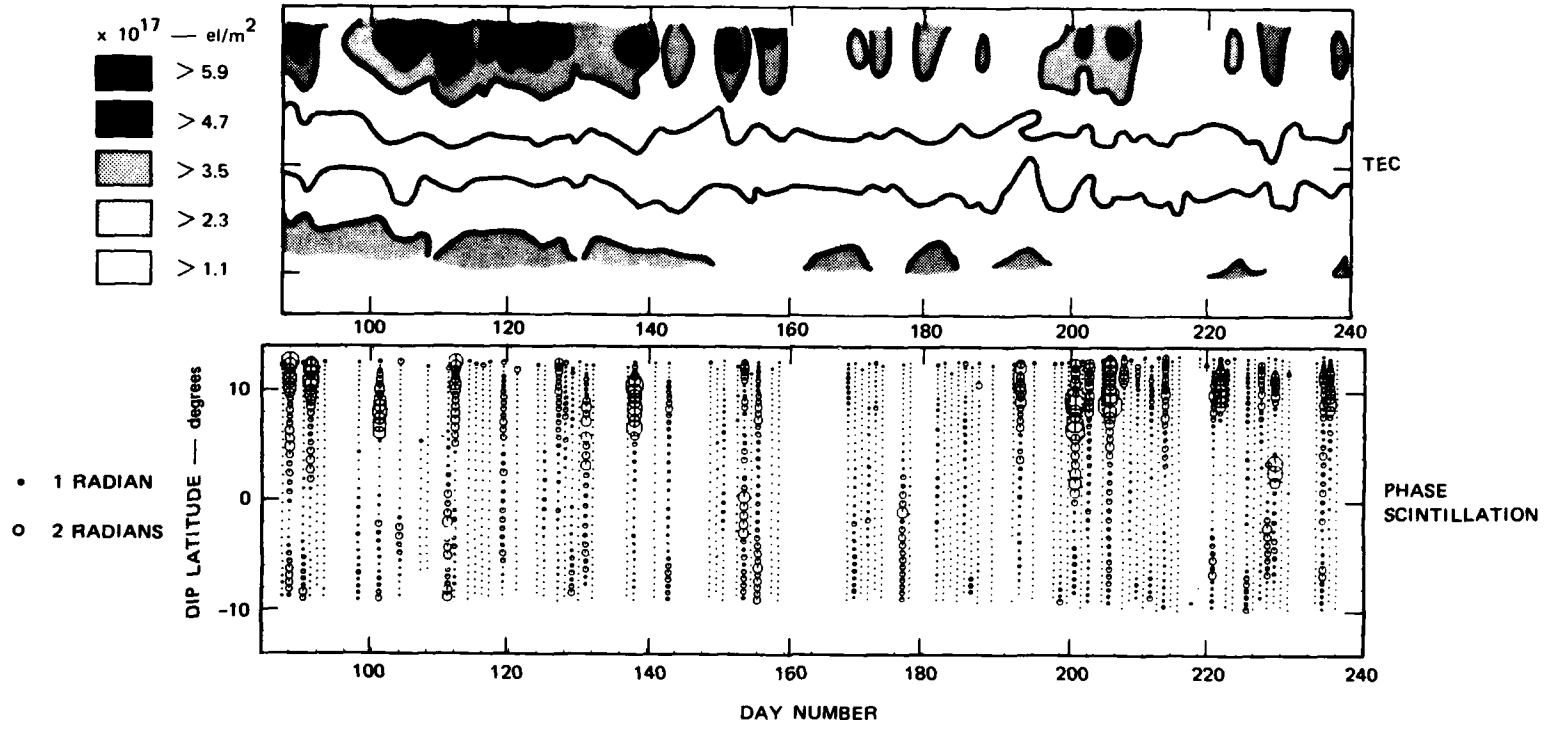

FIGURE 34 COMPARISON OF (a) TEC AND (b) UHF PHASE SCINTILLATION WITH LATITUDE AND TIME, KWAJALEIN, SUMMER 1978

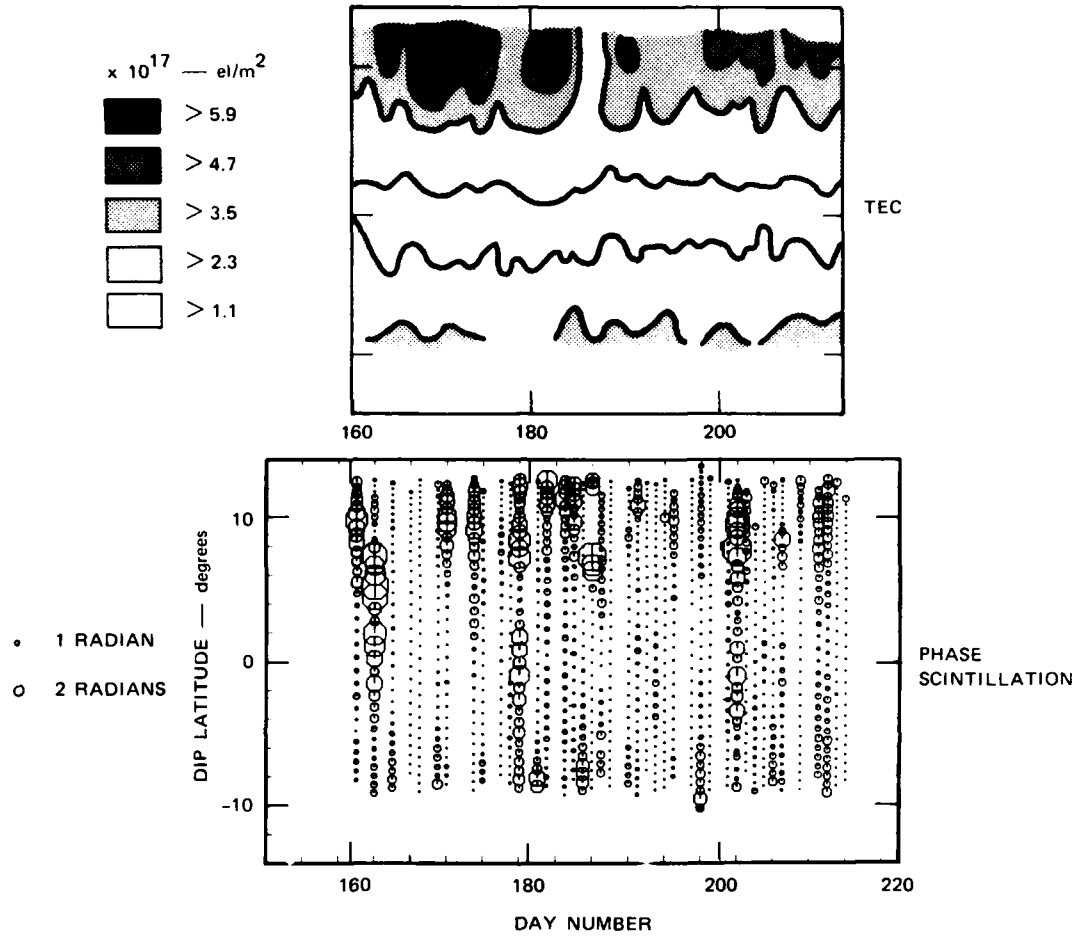

FIGURE 35 COMPARISON OF (a) TEC AND (b) UHF PHASE SCINTILLATION WITH LATITUDE AND TIME, KWAJALEIN, SUMMER 1979

F. Conclusions

Several conclusions can be drawn from our equatorial TEC study.

(1) The latitudinal distribution of TEC under no-anomaly conditions is best described by a layer whose height follows the local magnetic field. The effective vertical TEC of the layer at ±10° dip latitude is roughly half that at the dip equator, implying a decreasing layer thickness or peak density, or both.

(2) The occurrence of the nighttime equatorial anomaly is closely tied to the prereversal enhancement in vertical drift created by F-region dynamo fields. The anomaly is

absent during low solar activity, but increases rapidly with increasing sunspot number, as does the prereversal enhancement. Furthermore, the anomaly is strongest at the equinoxes, and weakest during the northern hemisphere, again in accord with the drift enhancement. This basic electrodynamic control is observed in both the American and Pacific sectors.

(3) The northern crest of the anomaly, as observed in TEC, remains within a few degrees of 12° dip latitude, as seen from Kwajalein. The southern crest remains generally beyond our observing range of -11° at Ancon. At both stations, a distinct northward shift in the anomaly is observed following the spring equinox. A similar, but less distinct, southward shift accompanies the fall equinox at Ancon. Such shifts in the anomaly symmetry are a result of transequatorial transport of ionization by F-region meridional winds. From our observations, which are limited in latitude, it cannot be established whether this shift is part of a longer term pattern, or is a distinct equinoctal event.

(4) While the seasonal behavior of TEC at Ancon and Kwajalein is similar at the equinoxes, it differs significantly during the northern hemisphere summer. The anomaly disappears at Ancon, but remains distinct, although limited in magnitude, at Kwajalein. Also, during this season, the solar-activity control of TEC, observed strongly at the equinoxes, saturates early in the solar-cycle upswing.

(5) The association between the occurrence of scintillation and TEC anomaly is not conspicuous. At Ancon, the peak scintillation is apparently associated more with the equinox anomaly shift, than with the anomaly magnitude. At Kwajalein, where the scintillation season is shifted six months from that at Ancon, the correlation between TEC magnitude and scintillation is better. Enhanced TEC is generally necessary for, but does not guarantee, enhanced scintillation.

Overall, then, similarities in the TEC behavior at Ancon and Kwajalein verify the basic electric field dependence of bulk motion in the equatorial F region. On the other hand, differences, such as the solstice behavior of the anomaly, and the scintillation behavior at the two stations, which indicates local (i.e., longitudinal) control sometimes dominate. The most likely candidate for this control is neutral atmospheric motion.

REFERENCES

Anderson, D. N., "A Theoretical Study of the Ionospheric F Region Equatorial Anomaly--I. Theory," Plant. Space Sci., Vol. 21, No. 3, pp. 409-419 (1973).

Anderson, D. N., and S. Matsushita, "Seasonal Differences in the Low-Latitude F2-Region Ionization Density Caused by E × B Drift and Neutral Wind," J. of Atmos. and Terr. Phys., Vol. 36, No. 11, pp. 2001-2011 (1974).

Booker, H. G., J. A. Ratcliffe, and D. H. Shinn, "Diffraction from an Irregular Screen with Applications to Ionospheric Problems," Phil. Trans. Roy. Soc. A., Vol. 242, pp. 242-579 (1950).

Bramley, E. N., "The Diffraction of Waves by an Irregular Refracting Medium," Proc. Roy. Soc. A., Vol. 225, p. 515 (1954).

Burns, A. A., and E. J. Fremouw, "A Red-Time Correction Technique for Transionospheric Ranging Error," IEEE Trans. on Ant. and Prop., AP-18, No. 6, pp. 785-790 (1970).

Cousins, M. D., Unpublished Report (1979).

Dandekar, B. S., "Study of the Equatorward Edge of the Auroral Oval from Satellite Observations," AFGL-TR-79-0010, Environmental Research Papers, No. 650 (1979).

Fejer, B. G., D. T. Farley, R. F. Woodman, and C. Calderon, "Dependence of Equatorial F Region Vertical Drifts," J. Geophys. Res., Vol. 84, No. A10, pp. 5792-5796 (1979).

Fejer, J. A., "The Diffraction of Waves in Passing Through an Irregular Refracting Medium," Proc. Roy. Soc. A, Vol. 220, pp. 455 (1953).

Fremouw, E. J., M. D. Cousins, and G. K. Durfey, "Wideband Satellite Observations," Bimonthly Report No. 5, Contract DNA001-75-C-0111, SRI Project 3793, Stanford Research Institute, Menlo Park, CA (1977).

Fremouw, E. J., R. L. Leadabrand, R. C. Livingston, M. D. Cousins, C. L. Rino, B. C. Fair, and R. A. Long, "Early Results from the DNA Wideband Satellite Experiment--Complex-Signal Scintillation," Radio Sci., Vol. 13, No. 1, pp. 167-187 (1978).

Hedin, A. E., H. G. Mayr, C. A. Reber, and N. W. Spencer, "Empirical Model of Global Therospheric Temperature and Composition Based on Data from the Ogo 6 Quadrapole Mass Spectrometer," J. Geophys. Res., Vol. 79, No. 1, pp. 215-225 (1974).

Heelis, R. A., P. C. Kendall, R. J. Moffett, and D. W. Windle, "Electrical Coupling of the E- and F-Regions and its Drifts and Winds," Planet Space Sci., Vol. 22, No. 6, pp. 743-756 (1974).

Kelley, M. C., R. Pfaff, K. D. Baker, J. C. Ulwick, R. C. Livingston, C. L. Rino, and R. T. Tsunoda, "Simultaneous Rocket Probe and Radar Measurements of Equatorial Spread F--Transitional and Short Wavelength Results," J. Geophys. Res., in press (1981).

Keskinen, M. J., B. E. McDonald, and S. L. Ossakow, "Preliminary Numerical Study of the Outer Scale Size of Ionospheric Plasma Cloud Striations," NRL Memorandum Report 4124, 3 December 1979.

Keskinen, M. J., E. P. Szuszczewicz, S. L. Ossakow, and J. C. Holmes, "Nonlinear Theory and Experimental Observations of the Local Collisional Rayleigh-Taylor Instability in a Descending Equatorial Spread F Ionosphere," NRL Memorandum Report No. 4455, 8, January 1981 (also in press), J. Geophys. Res. (1981).

Livingston, R. C., "Comparison of Multifrequency Equatorial Scintillation: American and Pacific Sectors," Radio Science, Vol. 15, No. 4, pp. 801-814 (1980).

Livingston, R. C., C. L. Rino, J. P. McClure, and W. B. Hanson, "Spectral Characteristics of Medium-Scale Equatorial F-Region Irregularities," J. Geophys. Res., Vol. 86, No. 44, pp. 2421-2428 (1981).

Lyon, A. J., and L. Thomas, "The F2 Region Equatorial Anomaly in the African, American, and East Asian Sectors during the Sunspot Maximum," J. Atmos. Terr. Phys., Vol. 25, No. 7, pp. 373-386 (1963).

McDaniel, D. R., "Proceedings of the Summer Equatorial Experiment Data Review Meeting, 18 March 1980," Technical Report, DNA Contract, Contract DNA001-78-C-0379, SRI Project 7745, SRI International, Menlo Park, CA (1980).

McDonald, B. E., S. L. Ossakow, S. T. Zalesak, and N. J. Zabusky, "Scale Sizes and Lifetimes of F-Region Plasma Cloud Striations as Determined by the Condition of Marginal Stability," NRL Memorandum Report 4383, Naval Research Laboratory, Washington, D.C. (1980).

Ossakow, S. L., "Spread-F Theories--A Review," NRL Memorandum Report 4455 (1981).

Rastogi, R. G., "The Diurnal Development of the Anomalous Equatorial Belt in the F2 Region of the Ionosphere," J. Geophys. Res., Vol. 64, No. 7, pp. 727-732 (1959).

Rino, C. L., "A Power Law Phase Screen Model for Ionospheric Scintillation, 1. Weak Scatter," Radio Science, Vol. 14, No. 6, pp. 1335-1145 (1979a).

Rino, C. L., "A Power Law Phase Screen Model for Ionospheric Scintillation, 2. Strong Scatter," Radio Science, Vol. 14, No. 6, pp. 1147-1155 (1979b).

Rino, C. L., "Propagation Effect in Disturbed Environments," DNA Final Report, Contract DNA001-80-C-0009, SRI Project 1129, SRI International, Menlo Park, CA (1980).

Rino, C. L., and J. Owen, "On the Temporal Coherence Loss of Strongly Scintillating Signals," Radio Science, Vol. 16, No. 1, pp. 31-33 (1981).

Rino, C. L., and J. Owen, "The Time Structure of Transionospheric Radio Wave Scintillation," Radio Science, Vol. 15, No. 3, pp. 479-489 (1980a).

Rino, C. L., and J. Owen, "The Structure of Localized Nighttime Auroral Zone Scintillation Enhancements," J. Geophys. Res., Vol. 85, No. 6, pp. 2941-2948 (1980b).

Rino, C. L., and C. H. Liu, "Intensity Scintillation Parameters for Characterizing Transionospheric Radio Signals," Radio Science (submitted for publication, 1981).

Rino, C. L., R. C. Livingston, B. C. Fair, and M. D. Cousins, "Continued Performance of the Wideband Satellite Experiment," DNA Final Report, Contract DNA001-77-C-0220, SRI Project 6434, SRI International, Menlo Park, CA (1980).

Rino, C. L., R. T. Tsunoda, J. Petriceks, R. C. Livingston, M. C. Kelley, and K. D. Baker, "Simultaneous Rocket-Borne Beacon and In-Situ Measurements of Equatorial Spread F--Intermediate Wavelength Results," J. Geophys. Res., Vol. 8, No. A4, pp. 2411-2420 (1981)

Rishbeth, H., "Dynamics of the Equatorial F-Region," J. Atmos. and Terr. Phys., Vol. 39, No. 9/10, pp. 1159-1168 (1977).

Rishbeth, H., "Polarization Fields Produced by Winds in the Equatorial F-Region," Planet. Space Sci., Vol. 19, No. 3, pp. 357-369 (1971).

Rush, C. M., "Some Effects of Neutral Wind Changes on the Low-Latitude F-Region," J. of Atmos. and Terr. Phys., Vol. 34, No. 8, pp. 1403-1409 (1972).

Singh, M., E. P. Szuszczewicz, and J. C. Holmes, "The STP/S3-4 Satellite Experiment: Equatorial F-Region Irregularities," Proceedings of the 1981 Symposium on the Effect of the Ionosphere on Radiowave Systems, Naval Research Laboratory, Washington, D.C. (1981).

Tsunoda, R. T., "Altair Radar Study of Equatorial Spread F," DNA Final Report, Contract DNA001-79-C-0153, SRI Project 8164, SRI Internationa, Menlo Park, CA (1981).

Tsunoda, R. T. "Magnetic-Field-Aligned Characteristics of Plasma Bubbles in the Nighttime Equatorial Ionosphere," J. of Atmos. and Terr. Phys., Vol. 42, No. 8, pp. 743-752 (1980).

Vickrey, J. F., "Radar Observations of Structured Plasma in the High-Latitude F Region," DNA Final Report, Contract DNA001-80-C-0015, SRI Project 1276, SRI International, Menlo Park, CA (1981).

Vila, P., "Etude Experimentale de L'Anomalie Ionospherique Equatoriale en Afrique en Periode de Minimum Solaire," Annales de Geophysique, Vol. 22, No. 3, pp. 396-404 (1966).

Wittwer, L., Private Communication (1981).

Zalesak, S. T., S. L. Ossakow, and P. K. Chaturvedi, "Predicting the Equatorial Spread-F/Scintillation Environment by Theoretical and Numerical Simulation Techniques," Proceedings of the 1981 Symposium on the Effect of the Ionosphere on Radiowave Systems, Naval Research Laboratory, Washington, D.C. (1981).

DISTRIBUTION LIST

DEPARTMENT OF DEFENSE

Assistant Secretary of Defense
Comm, Cmd, Cont & Intell
ATTN: Dir of Intel Sys, J. Babcock

Command & Control Tech Ctr
ATTN: C-650, G. Jones
ATTN: C-312, R. Mason
3 cy ATTN: C-650, W. Heidig

Defense Communications Agcy
ATTN: Code 480
ATTN: Code 480, F. Dieter
ATTN: Code 810, J. Barna
ATTN: Code 205
ATTN: Code 101B

Defense Communications Engr Ctr
ATTN: Code R410, N. Jones
ATTN: Code R123

Defense Intel Agcy
ATTN: DT-1B
ATTN: DB-4C, E. O'Farrell
ATTN: DB, A. Wise
ATTN: DIR
ATTN: DC-7B

Defense Nuclear Agcy
ATTN: NAFD
ATTN: STNA
ATTN: RAEE
ATTN: NATD
3 cy ATTN: RAAE
4 cy ATTN: TITL

Defense Technical Info Ctr
12 cy ATTN: DD

Field Command
Defense Nuclear Agcy
ATTN: FCP

Field Command
Defense Nuclear Agcy
Livermore Br
ATTN: FCPRL

Interservice Nuclear Wpns Sch
ATTN: TTV

Joint Chiefs of Staff
ATTN: C3S, Eval Ofc
ATTN: C3S

Joint Strat Tgt Planning Staff
ATTN: JLA
ATTN: JLTW-2

National Security Agcy
ATTN: R-52, J. Skillman
ATTN: B-3, F. Leonard
ATTN: W-32, O. Bartlett

DEPARTMENT OF DEFENSE (Continued)

Under Secretary of Defense for Rsch & Engrg
ATTN: Strategic & Space Sys (OS)

WWMCCS System Engrg Org
ATTN: R. Crawford

DEPARTMENT OF THE ARMY

Assistant Chief of Staff for Automation & Comm
Department of the Army
ATTN: DAAC-ZT, P. Kenny

Atmospheric Sciences Lab
US Army Electronics R&D Cmd
ATTN: DELAS-EO, F. Niles

BMD Advanced Technology Ctr
Department of the Army
ATTN: ATC-T, M. Capps
ATTN: ATC-O, W. Davies

BMD Systems Cmd
Department of the Army
2 cy ATTN: BMDSC-HW

Deputy Chief of Staff for Ops & Plans
Department of the Army
ATTN: DAMO-RQC

Harry Diamond Labs
Department of the Army
ATTN: DELHD-I-TL, M. Weiner
ATTN: Chief, Div 20000
ATTN: DELHD-N-RB, R. Williams

US Army Chemical Sch
ATTN: ATZN-CM-CS

US Army Comm-Elec Engrg Instal Agcy
ATTN: CCC-EMEO-PED, G. Lane
ATTN: CCC-CED-CCO, W. Neuendorf

US Army Communications Cmd
ATTN: CC-OPS-W
ATTN: CC-OPS-WR, H. Wilson

US Army Communications R&D Cmd
ATTN: DRDCO-COM-RY, W. Kesselman

US Army Foreign Science & Tech Ctr
ATTN: DRXST-SD

US Army Materiel Dev & Readiness Cmd
ATTN: DRCLDC, J. Bender

US Army Missile Intel Agcy
ATTN: YSE, J. Gamble

US Army Nuclear & Chemical Agcy
ATTN: Lib

DEPARTMENT OF THE ARMY (Continued)

US Army Satellite Comm Agcy
ATTN: Doc Con

US Army TRADOC Sys Analysis Actvy
ATTN: ATAA-PL
ATTN: ATAA-TDC
ATTN: ATAA-TCC, F. Payan, Jr

DEPARTMENT OF THE NAVY

COMSPTEVFOR
Department of the Navy
ATTN: Code 605, R. Berg

Joint Cruise Missiles Proj Ofc
Department of the Navy
ATTN: JCMG-707

Naval Air Development Ctr
ATTN: Code 6091, M. Setz

Naval Air Systems Cmd
ATTN: PMA 271

Naval Electronic Systems Cmd
ATTN: PME 117-211, B. Kruger
ATTN: PME 106-4, S. Kearney
ATTN: PME 106-13, T. Griffin
ATTN: PME 117-2013, G. Burnhart
ATTN: Code 501A
ATTN: PME 117-20
ATTN: Code 3101, T. Hughes

Naval Intelligence Support Ctr
ATTN: NISC-50

Naval Ocean Systems Ctr
ATTN: Code 532, R. Pappert
ATTN: Code 532, J. Bickel
ATTN: Code 5322, M. Paulson
3 cy ATTN: Code 5323, J. Ferguson

Naval Research Lab
ATTN: Code 4780, S. Ossakow
ATTN: Code 7950, J. Goodman
ATTN: Code 7550, J. Davis
ATTN: Code 4187
ATTN: Code 4700, T. Coffey
ATTN: Code 7500, B. Wald

Naval Space Surveillance Sys
ATTN: J. Burton

Naval Surface Wpns Ctr
ATTN: Code F31

Naval Telecom Cmd
ATTN: Code 341

Office of Naval Rsch
ATTN: Code 420
ATTN: Code 465
ATTN: Code 421

Office of the Chief of Naval Ops
ATTN: OP 981N
ATTN: OP 941D
ATTN: OP 65

DEPARTMENT OF THE NAVY (Continued)

Strategic Systems Proj Ofc
Department of the Navy
ATTN: NSP-2141
ATTN: NSP-43
ATTN: NSP-2722, F. Wimberly

DEPARTMENT OF THE AIR FORCE

Aerospace Defense Cmd
Department of the Air Force
ATTN: DC, T. Long

Air Force Geophysics Lab
ATTN: OPR, H. Gardiner
ATTN: OPR-1
ATTN: LKB, K. Champion
ATTN: OPR, A. Stair
ATTN: S. Basu
ATTN: PHP
ATTN: PHI, J. Buchau
ATTN: R. Thompson

Air Force Weapons Lab
Air Force Systems Command
ATTN: SUL
ATTN: NTYC
ATTN: NTN

Air Force Wright Aeronautical Lab
ATTN: W. Hunt
ATTN: A. Johnson

Air Logistics Command
Department of the Air Force
ATTN: OO-ALC/MM

Air University Lib
Department of the Air Force
ATTN: AUL-LSE

Air Weather Service, MAC
Department of the Air Force
ATTN: DNXP, R. Babcock

Assistant Chief of Staff
Studies & Analyses
Department of the Air Force
ATTN: AF/SASC, C. Rightmeyer
ATTN: AF/SASC, W. Keaus

Ballistic Missile Ofc
Air Force Systems Command
ATTN: ENSN, J. Allen

Deputy Chief of Staff
Ops Plans and Readiness
Department of the Air Force
ATTN: AFXOKS
ATTN: AFXOXFD
ATTN: AFXOKT
ATTN: AFXOKCD

Deputy Chief of Staff
Rsch, Dev, & Acq
Department of the Air Force
ATTN: AFRDS
ATTN: AFRDSP
ATTN: AFRDSS

DEPARTMENT OF THE AIR FORCE (Continued)

Electronic Systems Div
Air Force Systems Command
ATTN: DCKC, J. Clark

Electronic Systems Div
Air Force Systems Command
ATTN: OCT-4, J. Deas

Electronic Systems Div
Air Force Systems Command
ATTN: YSM, J. Kobelski
ATTN: YSEA

Foreign Technology Div
Air Force Systems Command
ATTN: TQTD, B. Ballard
ATTN: NIIS, Lib

Headquarters Space Div
Air Force Systems Command
ATTN: SKA, D. Bolin
ATTN: SKY, C. Kennedy

Headquarters Space Div
Air Force Systems Command
ATTN: YZJ, W. Mercer

Headquarters Space Div
Air Force Systems Command
ATTN: E. Butt

Rome Air Development Ctr
Air Force Systems Command
ATTN: OCS, V. Coyne
ATTN: TSLD

Rome Air Development Ctr
Air Force Systems Command
ATTN: EEP

Strategic Air Cmd
Department of the Air Force
ATTN: DCXT
ATTN: DCXR, T. Jorgensen
ATTN: NRT
ATTN: XPFS
ATTN: DCX

OTHER GOVERNMENT AGENCIES

Central Intelligence Agcy
ATTN: OSWR/NED

Department of Commerce
National Bureau of Standards
ATTN: Sec Ofc for R. Moore

Department of Commerce
National Oceanic & Atmospheric Admin
ATTN: R. Grubb

Institute for Telecom Sciences
National Telecom & Info Admin
ATTN: A. Jean
ATTN: L. Berry
ATTN: W. Utlaut

DEPARTMENT OF ENERGY CONTRACTORS

EG&G, Inc
ATTN: J. Colvin
ATTN: D. Wright

Lawrence Livermore Natl Lab
ATTN: L-389, R. Ott
ATTN: L-31, R. Hager
ATTN: Tech Info Dept Lib

Los Alamos Natl Lab
ATTN: D. Simons
ATTN: E. Jones
ATTN: D. Westervelt
ATTN: P. Keaton
ATTN: MS 670, J. Hopkins
ATTN: R. Taschek
ATTN: MX 664, J. Zinn

Sandia National Labs
Livermore Lab
ATTN: B. Murphey
ATTN: T. Cook

Sandia Natl Lab
ATTN: Org 4241, T. Wright
ATTN: D. Thornbrough
ATTN: Org 1250, W. Brown
ATTN: 3141
ATTN: D. Dahlgren
ATTN: Space Proj Div

DEPARTMENT OF DEFENSE CONTRACTORS

Aerospace Corp
ATTN: R. Slaughter
ATTN: J. Straus
ATTN: V. Josephson
ATTN: I. Garfunkel
ATTN: D. Olsen
ATTN: T. Salmi
ATTN: N. Stockwell
ATTN: S. Bower

University of Alaska
ATTN: Tech Lib
ATTN: N. Brown
ATTN: T. Davis

Analytical Systems Engrg Corp
ATTN: Radio Sciences

Analytical Systems Engrg Corp
ATTN: Scty

Barry Research Corp
ATTN: J. McLaughlin

BDM Corp
ATTN: L. Jacobs
ATTN: T. Neighbors

Berkeley Research Assoc, Inc
ATTN: J. Workman

Betac
ATTN: J. Hirsch

DEPARTMENT OF DEFENSE CONTRACTORS (Continued)

Boeing Co
ATTN: M/S 42-33, J. Kennedy
ATTN: G. Hall
ATTN: S. Tashird

Booz-Allen & Hamilton, Inc
ATTN: B. Wilkinson

University of California at San Diego
ATTN: H. Booker

Charles Stark Draper Lab, Inc
ATTN: J. Gilmore
ATTN: D. Cox

Communications Satellite Corp
ATTN: D. Fang

Computer Sciences Corp
ATTN: F. Eisenbarth

Comsat Labs
ATTN: R. Taur
ATTN: G. Hyde

Cornell University
ATTN: M. Kelly
ATTN: D. Farley, Jr

E-Systems, Inc
ATTN: R. Berezdivin

Electrospace Systems, Inc
ATTN: H. Logston

ESL, Inc
ATTN: J. Marshall

General Electric Co
ATTN: M. Bortner
ATTN: A. Harcar

General Electric Co
ATTN: C. Zierdt
ATTN: A. Steinmayer

General Electric Co
ATTN: F. Reibert

General Electric Co
ATTN: G. Millman

General Research Corp
ATTN: J. Ise, Jr
ATTN: J. Garbarino

Harris Corp
ATTN: E. Knick

Horizons Technology, Inc
ATTN: R. Kruger

HSS, Inc
ATTN: D. Hansen

IBM Corp
ATTN: F. Ricci

DEPARTMENT OF DEFENSE CONTRACTORS (Continued)

University of Illinois
ATTN: K. Yeh

Institute for Defense Analyses
ATTN: E. Bauer
ATTN: H. Wolfhard
ATTN: J. Aein
ATTN: J. Bengston

International Tel & Tel Corp
ATTN: Tech Lib
ATTN: G. Wetmore

JAYCOR
ATTN: J. Sperling

JAYCOR
ATTN: J. Doncarlos

Johns Hopkins University
ATTN: T. Potemra
ATTN: J. Phillips
ATTN: T. Evans
ATTN: J. Newland
ATTN: P. Komiske

Kaman Tempo
ATTN: DASIAC
ATTN: T. Stephens
ATTN: W. McNamara
ATTN: W. Knapp

Linkabit Corp
ATTN: I. Jacobs

Litton Systems, Inc
ATTN: R. Grasty

Lockheed Missiles & Space Co, Inc
ATTN: W. Imhof
ATTN: M. Walt
ATTN: R. Johnson

Lockheed Missiles & Space Co, Inc
ATTN: Dept 60-12
ATTN: D. Churchill
ATTN: C. Old

M.I.T. Lincoln Lab
ATTN: D. Towle

Martin Marietta Corp
ATTN: R. Heffner

McDonnell Douglas Corp
ATTN: N. Harris
ATTN: J. Moule
ATTN: W. Olson
ATTN: G. Mroz
ATTN: R. Halprin

Meteor Communications Consultants
ATTN: R. Leader

DEPARTMENT OF DEFENSE CONTRACTORS (Continued)

Mission Research Corp
ATTN: R. Kilb
ATTN: Tech Lib
ATTN: R. Hendrick
ATTN: F. Fajen
ATTN: R. Bogusch
ATTN: S. Gutsche
ATTN: D. Sappenfield

Mitre Corp
ATTN: G. Harding
ATTN: C. Callahan
ATTN: A. Kymmel
ATTN: B. Adams

Mitre Corp
ATTN: M. Horrocks
ATTN: W. Foster
ATTN: J. Wheeler
ATTN: W. Hall

Pacific-Sierra Rsch Corp
ATTN: F. Thomas
ATTN: E. Field, Jr
ATTN: H. Brode

Pennsylvania State University
ATTN: Ionospheric Rsch Lab

Photometrics, Inc
ATTN: I. Kofsky

Physical Dynamics, Inc
ATTN: E. Fremouw

Physical Research, Inc
ATTN: R. Deliberis

R & D Associates
ATTN: R. Lelevier
ATTN: R. Turco
ATTN: C. Greifinger
ATTN: B. Gabbard
ATTN: M. Gantsweg
ATTN: W. Karzas
ATTN: H. Ory
ATTN: W. Wright
ATTN: F. Gilmore
ATTN: P. Haas

R & D Associates
ATTN: B. Yoon

Rand Corp
ATTN: E. Bedrozian
ATTN: C. Crain

Riverside Research Inst
ATTN: V. Trapani

DEPARTMENT OF DEFENSE CONTRACTORS (Continued)

Rockwell International Corp
ATTN: R. Buckner

Rockwell International Corp
ATTN: S. Quilici

Santa Fe Corp
ATTN: D. Paolucci

Science Applications, Inc
ATTN: E. Straker
ATTN: L. Linson
ATTN: C. Smith
ATTN: D. Hamlin

Science Applications, Inc
ATTN: SZ

Science Applications, Inc
ATTN: J. Cockayne

SRI International
ATTN: R. Leadabrand
ATTN: D. Neilson
ATTN: J. Petrickes
ATTN: G. Price
ATTN: R. Tsunoda
ATTN: A. Burns
ATTN: M. Baron
ATTN: G. Smith
ATTN: W. Chesnut
ATTN: W. Jaye
4 cy ATTN: R. Livingston
4 cy ATTN: C. Rino
4 cy ATTN: J. Owen

Sylvania Systems Group
ATTN: I. Kohlberg
ATTN: R. Steinhoff

Technology International Corp
ATTN: W. Boquist

Tri-Com, Inc
ATTN: D. Murray

TRW Devense & Space Sys Gp
ATTN: R. Plebuch
ATTN: D. Dee

Utah State University
ATTN: K. Baker
ATTN: L. Jensen
ATTN: J. Dupnik

Visidyne, Inc
ATTN: C. Humphrey
ATTN: J. Carpenter


FILMED